Few-Layer Transition Metal Chloride Graphene Intercalation Compounds

David Pavitt

Physics Department

Royal Holloway University of London

A thesis submitted for the degree of

Doctor of Philosophy (PhD)

September 2013

Declaration

I David Pavitt hereby declare that this thesis and the work within it are my own carried out under the supervision of Dr James Nicholls and where I have collaborated with others, this is clearly stated.

Signed

David Pavitt
September 2013

Abstract

Few-layer transition metal chloride *graphene* intercalation compounds have been fabricated by the mechanical exfoliation of graphite intercalation compounds (GICs) containing $CoCl_2$, $NiCl_2$, $CuCl_2$, $MnCl_2$ and $FeCl_3$. The number of graphene layers and the distribution of the intercalate in the few-layer graphene intercalation compounds (FLGICs) have been characterised using the optical contrast of the FLGICs against the SiO_2 substrate and the G-peak of the Raman spectrum. FLGICs containing a single intercalate layer surrounded by two graphene layers have been fabricated and characterised, which are an ideal system to study 2D magnetic phase transitions. Atomic force microscopy (AFM), electrostatic force microscopy (EFM), Kelvin probe force microscopy (KPFM) and spatial maps of the Raman spectrum have revealed the intercalate layers in FLGICs form domains several microns across due to deintercalation from mechanical exfoliation. Once exfoliated, the domain structure of FLGICs remains stable for many months. Electronic transport and Raman spectroscopy measurements reveal the graphene layers in FLGICs to be highly p-doped with charge densities of up to $n = 8 \times 10^{13}$ cm^{-2}, making them suitable to be used as transparent conductors in future electronic devices.

Acknowledgements

I am very grateful to everyone who helped me throughout my time at Royal Holloway, and in particular my supervisor Dr James Nicholls who guided me throughout the PhD. I am very grateful for the help of Axel Eckmann and Dr Cinzia Casiraghi whom without, Raman spectroscopy measurements would not be possible. I would like to acknowledge Vishal Panchal and Dr Olga Kazakova for their assistance with vital AFM and EFM measurements. Many thanks go to Dr Spas Spasov for his assistance with running the dilution refrigertor and Mr Francis Greenough for maintaining us with a supply of liquid helium. I would like to thank Dr Rais Shaikhaidarov and Dr Vladimir Antinov for showing me how to use the equipment needed for device fabrication and thanks goes to fellow students Dr Ray Davis, Dr Richard Marsh, Connor Shelly and Jim Wells for their general assistance when working in the labs. I would like to thank Dr Dan Porter for his expertise in X-ray diffraction and I would like to thank my friends around the deparment; Rob Cantrill, Aya Shibahara, Manoj Pandiyan, Simon Schmidlin, Stephen Pelling, Chris Harrison, George Nichols, Terence Giles and others for their support and entertainment during lunchbreaks and Friday trips to the pub.

Finally I owe a massive thanks to my family who are supportive of me whatever I choose to do and to you, I dedicate this thesis.

Contents

Table of Contents **v**

List of Figures **viii**

List of Tables **xiii**

1 Introduction **1**

2 Background **3**

2.1 Graphene . . . 3

2.1.1 Introduction . . . 3

2.1.2 Crystallographic Structure . . . 5

2.1.3 Electronic Structure . . . 6

2.1.4 Fabrication of Graphene . . . 10

2.1.4.1 Mechanical Exfoliation . . . 10

2.1.4.2 Other Fabrication Routes . . . 12

2.2 Graphite Intercalation Compounds . . . 14

2.2.1 Overview . . . 14

2.2.2 Magnetic Graphite Intercalation Compounds . . . 18

2.3 Raman Spectroscopy . . . 19

2.3.1 Introduction . . . 19

2.3.2 Raman spectroscopy of Graphene . . . 21

2.3.2.1 The Main Features of the Spectrum . . . 22

2.3.2.2 The Effects of Doping . . . 26

2.3.2.3 Number of Layers and Orientation . . . 27

2.3.2.4 Strain Effects . . . 32

2.3.3 Raman Spectroscopy of GICs 32
2.4 Review of $FeCl_3$ FLGIC Studies 33
2.5 Scanning Probe Microscopies 37
2.5.1 Imaging of Graphene 38

3 Fabrication and Experimental Setup 42
3.1 Fabrication of GICs 42
3.2 Characterisation of GICs 43
3.2.1 Weight Uptake 43
3.2.2 X-ray Diffraction 44
3.2.3 Raman Microprobe of the GIC surface 45
3.3 Exfoliation of GICs 47
3.3.1 Exfoliation Technique 47
3.3.2 Microdroplet Formation 52
3.4 Optical Contrast of Intercalated Flakes 52
3.4.1 Estimated Contrast Change due to the Intercalate Layers 52
3.4.2 Estimating the Number of Layers Experimentally 55
3.5 Fabrication of Devices 57
3.6 Low Temperature Measurement Setup 59
3.6.1 Current Annealing 62

4 Raman spectroscopy of FLGICs 66
4.1 Raman Spectra of $CoCl_2$, $NiCl_2$, $CuCl_2$ and $MnCl_2$ FLGICs 66
4.1.1 Raman Spectra of FLGICs with i2L Structure 69
4.1.2 Raman Spectra of FLGICs with ii3L Structure 69
4.1.3 Raman Spectra of FLGICs with i3L Structure 71
4.2 Raman Spectra of $FeCl_3$ FLGICs 72
4.3 Raman Spectra of FLGICs Containing 4+ Graphene Layers 75
4.4 Raman Maps 75
4.4.1 Intercalated Domains 78
4.4.2 Other Observations from Raman Maps 78
4.5 Stability of FLGICs 82
4.6 Measurements at Different Excitation Energies 83

5 Intercalated Domains Studied by Scanning Probe Microscopies 86
5.1 AFM Images 86
5.2 EFM Images 90
5.3 Quantitative EFM Measurements 95
5.4 KPFM Images 97

6 Electronic Transport in FLGICs 100
6.1 Sweeping the Back Gate 100
6.1.1 FLGIC Samples 100
6.1.2 Pristine Graphene Samples 102
6.2 Measurements in a Perpendicular Magnetic Field 105
6.3 Current Annealing of FLGICs 105

7 Conclusions and Future Work 111
7.1 Future Work 112

References 115

List of Figures

2.1 Image showing how graphene (2D) can be stacked to form graphite (3D), rolled into a carbon nanotube (1D) or wrapped up to form a buckyball (0D - Fullerene). 4

2.2 The graphene lattice and reciprocal space 5

2.3 Dispersion relation of electrons in graphene with the inset showing the linear bands around the K point 7

2.4 Electronic masurement of gated graphene 8

2.5 (a) Dispersion relation of electrons in bilayer graphene around the K point and (b) dispersion relation with a gate voltage V_g applied that introduces a band gap 8

2.6 Density of states for typical 2D systems and graphene. The linear band structure of graphene gives it a different DOS compared to a typical 2D semiconductor with parabolic bands 9

2.7 Thin film model of graphene on a silicon substrate with a SiO_2 oxide layer 11

2.8 Optical contrast of monolayer graphene on a Si substrate with a SiO_2 layer and incident light of wavelength λ 13

2.9 Staging in graphite intercalation compounds 16

2.10 Representation of the Daumas-Hérold domain model for a stage-3 GIC showing intercalate forming in-plane domains but retaining the staging structure. 17

2.11 Representation intercalate islands for a GIC that has de-intercalated, with trapped islands of intercalate remaining 17

2.12 (a) The $CdCl_2$ structure that is adopted by the $CoCl_2$, $MnCl_2$ and $NiCl_2$ compounds. (b) Representation of a stage-1 $CoCl_2$-GIC with repeat distance I_c. 18
2.13 (a)Stokes Raman scattering process where a photon with energy $\hbar\omega_L$ scatters with a phonon (Ω) and leaves the system with energy $\hbar\omega_S$. (b) Energy diagram of Rayleigh, non-resonant Raman and resonant Raman processes 20
2.14 Phonon dispersion relation of graphene 22
2.15 Representation of the phonon modes in graphene and graphite 23
2.16 The Raman spectrum of graphene and graphite with the G and 2D peaks labelled. 24
2.17 The electron-phonon processes for the G, D and 2D peaks of the Raman spectrum 25
2.18 The Raman spectrum of a graphene edge measured at 2.41 eV. The edge causes disorder in the graphene lattice. The G and 2D peaks are observed plus additional peaks labelled D and D' due to the disorder. . 26
2.19 Raman measurement of monolayer graphene with a voltage applied to the back gate to control the electron concentration 28
2.20 Evolution of the 2D peak for an increasing number of graphene layers. 29
2.21 The 2D Raman process in bilayer graphene 30
2.22 Raman spectrum of rotated bilayer graphene showing the D, G and 2D peaks when the graphene layers are misoriented by the specified angle . 31
2.23 Raman spectrum of $FeCl_3$-GICs with stage index n measured at 488 nm. The evolution of the G band with stage number is seen. 34
2.24 The position of the high frequency $\omega(\hat{E}_{2g2})$ (G_2) and low frequency component $\omega(E^{\circ}_{2g})$ (G_1) of the G band are plotted for various a) accepter and b) donor GICs against their reciprocal stage index 35
2.25 Raman Spectrum of Pristine and $FeCl_3$ Intercalated Graphene Layers . 36
2.26 (a) The temperature dependence of the square resistance in $FeCl_3$ FLGICs containing 2-5 graphene layers and (b) in pristine graphene samples for comparison 37
2.27 Sweeping V_{tip} in EFM measurements to obtain values of surface potential for different numbers of graphene layers 39

2.28 AFM and EFM images of exfoliated few-layer graphene SiO_2 40
2.29 (a) AFM image of graphene film grown epitaxially on SiC(0001) and (b) corresponding KPFM image 40
2.30 EFM image of a HOPG surface where a variation in phase can be observed, revealing regions of conducting and insulating-like behaviour . . 41

3.1 Synthesis system for a $FeCl_3$-GIC 43
3.2 hk0 X-ray of a $CoCL_2$-GIC 46
3.3 Raman spectra of a stage-1 $FeCl_3$ GIC measured at 488 nm 47
3.4 Raman spectra of a mixed stage $FeCl_3$ GIC measured at 488 nm 48
3.5 Optical image of a graphene flake exfoliated from Kish graphite with a measured contrast of 5% against the substrate background. The flake was confirmed to be monolayer graphene by Raman spectroscopy. 49
3.6 Optical images of flakes exfoliated from kish graphite which are triangular and exhibit overlapping regions and folding of the graphene layers. The scale bar is 10 μm 51
3.7 Optical images of FLGICs exfoliated from (left) a stage-2 $CoCl_2$-GIC and (right) a stage-1 $MnCl_2$-GIC, both based on kish. The structure appears deformed compared to flakes exfoliated from pristine kish graphite. The scale bar is 10 μm. 51
3.8 Optical images of trails of FLGICs produced by pushing a GIC along the substrate. The scale bar is 10 μm. 51
3.9 Optical images showing microdroplet formation during fabrication of FLGICs 53
3.10 Calculated optical contrast of FLGICs 56
3.11 Illustration of a back gated graphene device 58
3.12 Illustration showing the steps in device fabrication 58
3.13 Optical image of fabricated devices showing metal pads in contact with the exfoliated flakes 60
3.14 Sample mounted onto a chip carrier 61
3.15 Optical image of a flake showing a tear that formed due to excessive heating when bonding. 61

3.16 Phase diagram of liquid ^{3}He–^{4}He mixture at saturated vapour pressure, showing the phase separation line below which the mixture separates into a ^{4}He-rich and a ^{3}He-rich phase. 63
3.17 Two-terminal measurement circuit showing an AC signal applied to the sample and measured using a lock in amplifier. 64

4.1 The possible stacking arrangements of layers in FLGICs produced by the exfoliation of GICs 68
4.2 Rama spectra of FLGICs 70
4.3 Raman Spectra of Sample 6-$FeCl_3$-BB 73
4.4 Raman spectra of FLGICs containing 4+ graphene layers 74
4.5 Optical Image and Raman maps of G peak for sample 5-$CuCl_2$-EC . . . 76
4.6 Raman maps of G peak for sample 3-$CoCl_2$-B3 containing a $CoCl_2$-intercalated flake tens of layers thick. 77
4.7 Raman maps of the 2D and D peak for sample 5-$CuCl_2$-EC 79
4.8 Optical Image and Raman maps of G peak for sample 5-$MnCl_2$-CD . . . 80
4.9 Raman maps of the 2D and D peak for sample 5-$MnCl_2$-CD 81
4.10 Raman maps of G peak and $FeCl_3$ mode intensity of sample 6-$FeCl_3$-BB taken over 24 hours 84
4.11 Raman map of sample 5-$MnCl_2$-CD showing no changes in the G peak position over 8 months 85
4.12 Comparison of the 2D peak of sample 5-$MnCl_2$-CD measured at two laser energies 85

5.1 AFM height image of sample 5-$MnCl_2$-CD 87
5.2 AFM height image of sample 5-$CuCl_2$-EC 88
5.3 AFM profile of a intercalated domain in sample 5-$MnCl_2$-CD 89
5.4 EFM phase image of sample 5-$MnCl_2$-CD 91
5.5 EFM Phase Image of sample 5-$CuCl_2$-EC 92
5.6 EFM profiles of sample 5-$MnCl_2$-CD with different values of V_{tip} 93
5.7 Histogram of EFM phase for sample 5-$MnCl_2$-CD. 94
5.8 V_{tip} is varied in EFM Mode at various positions over sample 5-$MnCl_2$-CD to measure surface potential 96
5.9 KPFM image of sample 5-$MnCl_2$-CD 97

5.10 Histogram of KPFM voltages for sample 5-$MnCl_2$-CD 99

6.1 Resistance measured across FLGICs with the back gate voltage being varied 103
6.2 Resistance measured across a non-intercalated 2L flake with the back gate voltage being varied 104
6.3 Measurements of FLGICs in a magnetic field at 30 mK 106
6.4 Resistance of FLGICs plotted against inverse magnetic field 107
6.5 Sample-23 measured before and after current annealing 109
6.6 Measured current during annealing of FLGIC sample-23 110

7.1 A comparison of techniques used to image sample 5-$MnCl_2$-CD 113

List of Tables

2.1 Structure Parameters for the Transition Metal Chlorides 17
2.2 Raman G peak positions for GICs and FLGICs 33

3.1 Expected Weight Uptake of GICs 44

4.1 A list of the GICs exfoliated to produce samples for Raman spectroscopy measurement. The stage indices are identified from the weight uptake during intercalation. 67

6.1 List of samples showing the measured resistances and position of the Dirac point 101

Chapter 1

Introduction

The discovery of graphene by exfoliating graphite has lead to an explosion of related research and was awarded the Nobel prize in 2010. Following the interest in graphene research, this thesis explores the exfoliation of graphite intercalation compounds (GICs), adding a novel twist to the techniques originally used to exfoliate graphite, resulting in new few-layer graphene intercalation compounds (FLGICs) consisting of 2-4 graphene layers separated by transition metal chloride layers.

Graphene is a candidate for use as a transparent conductor in future devices such as touch screens, flexible displays and solar cells[1, 2]. Tin-doped indium oxide (ITO) is currently the material of choice for transparent conductive electrodes but the search is on for alternatives as the price of indium is increasing[2] and future devices may demand bendable electrodes. Graphene is transparent, flexible and has the potential to be low cost due to the abundance of carbon but it has a higher sheet resistance than ITO ($R_s = 10\,\Omega/\square$). FLGICs may be a superior alternative than graphene to replace ITO since the intercalate layers in GICs increase the conductivity of the graphene layers through charge transfer (doping). Carbon nanotube (CNT) films and networks of metallic nanowires have also emerged as alternatives to ITO. Currently the resistance at CNT - CNT junctions is a limiting factor[1] and to compare to the sheet resistance (R_s) of ITO they need to be $> 100\,\text{nm}$ thick, severely reducing the transparency. Networks of metallic nanowires have electronic and optical properties that rival ITO[3] however much research is needed to produce a large scale fabrication methods.

Molecular beam epitaxy can be used to fabricate ultrathin magnetic films[4] where one or two magnetic monolayers are grown on top of another non-magnetic metal, and

are studied as 2D magnetic systems[5, 6]. FLGICs may provide an additional set of systems to investigate 2D magnetic behaviour. Historically transition metal chloride GICs have been studied[7] to investigate two-dimensional magnetic phase transitions, since the magnetic ions exhibit a strong coupling between spins within a plane and have a weak coupling between the planes, due to the separation of intercalate layers by the graphite host. FLGICs are of interest in this area as the possibility of isolating a single intercalate layer, i.e. fabricating a sample consisting of two graphene layers separated by a single intercalate layer, can be studied as a model 2D system with no interplanar interactions which have previously obscured clear observation of 2D magnetic phase transitions. The graphene layers will act as a benign mechanically strong host and protect the intercalate layer from surface contamination which have previously affected the properties of ultrathin magnetic films[4].

This thesis contains seven chapters including the introduction. Chapter 2 outlines the background properties of graphene, graphite and GICs which are core to this thesis and the principles behind Raman spectroscopy and scanning probe microscopy that are used to study samples in this thesis.

Chapter 3 lays out the fabrication methods used to produce GICs, their exfoliation, the thin film model used to describe the visibility of the resulting FLGICs and the processing of FLGICs into devices for two-terminal measurements at low temperatures.

Chapter 4 presents the results from Raman spectroscopy which identifies intercalate layers amongst the exfoliated GIC flakes. The differences in the Raman spectra of FLGICs of different number of graphene layers (2-4) are discussed. Raman maps show how the intercalate layers are arranged spatially.

In chapter 5 the in-plane structure of the FLGICs is studied using atomic force microscopy (AFM), electrostatic force microscopy (EFM) and Kelvin probe force microscopy (KPFM) and the surface potential of a FLGIC is measured.

Chapter 6 presents results from two-terminal electrical transport measurements at low temperatures of FLGICs that have been fabricated into devices containing ohmic contacts and a back gate.

Chapter 7 summaries the findings of the thesis and discusses possible future work to be carried out.

Chapter 2

Background

2.1 Graphene

2.1.1 Introduction

Graphene is a single layer of carbon atoms arranged in a honeycomb lattice as shown in Fig. 2.1. It is the building block for other carbon-based materials where the rolling up graphene produces carbon nanotubes and buckyballs while stacking graphene produces graphite. The in-plane strength of the carbon bonds is much stronger than the c-axis bonds of graphite causing it to shear easily. It is this ability for graphite to cleave easily that lead to the first isolation of a single graphene by simply using adhesive tape in a technique known as mechanical exfoliation[8]. Before the discovery of free-standing graphene it was only studied theoretically[9] and thought thermodynamically unstable and not possible to exist[10, 11]. Following the discovery of graphene in 2003 came a huge wave of scientific research[12]. Graphene was found to exhibit many amazing properties and is hyped to become the new silicon[13]. Its exceptional qualities include atomic thinness, transparency, thermal conductivity, electrical conductivity, charge density, carrier mobility, strength, and flexibility, which show great promise for a wide range of applications[13].

The mobility of a graphene sheet is up to 10^5 cm^2/Vs[15] at room temperatures, several orders of magnitude higher than silicon. This makes it a promising candidate for various nanoelectronic applications and devices operating at high frequencies. Graphene is a zero gap semiconductor, also known as a semi-metal[13]. A typical field

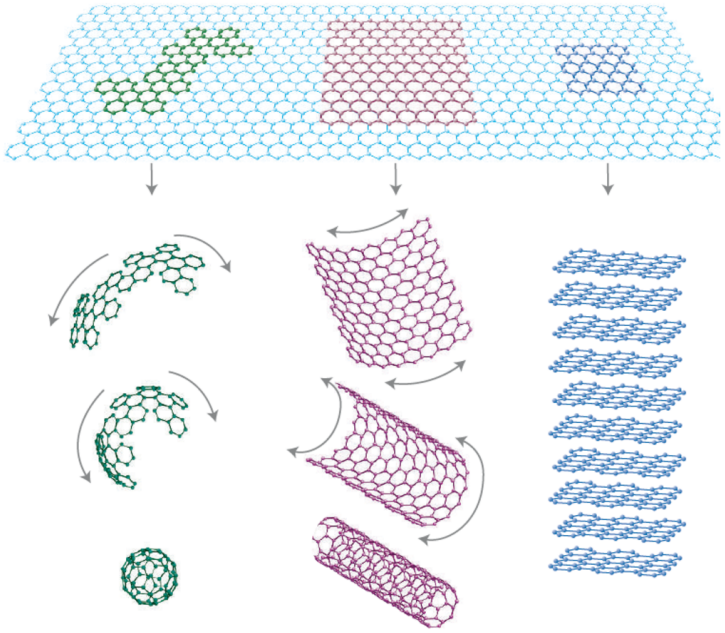

Figure 2.1: Image[14] showing how graphene (2D) can be stacked to form graphite (3D), rolled into a carbon nanotube (1D) or wrapped up to form a buckyball (0D - Fullerene).

effect transistor (FET) requires an off state and so efforts have been made to introduce a band gap into graphene for the production of graphene FETs[16].

Graphene is found to withstand high temperatures, up to ∼600°C during current annealing and has been shown to have a high thermal conductivity of around 5×10^3 W/mK[17, 18]. It has unprecedented strength, measurements on suspended graphene have yielded a breaking strength 42 N/m[19], the strongest material on record (although only valid on the microscopic level). As well as being mechanically strong graphene is highly elastic with a Young's modulus of 1 TPa[19].

Graphene has a range of interesting electronic properties[20, 21] that have been studied. The linear electron dispersion results in a rest mass of zero where the electrons behave as massless Dirac fermions[22], the reason for such high mobility seen in graphene. The Fermi velocity of electrons in graphene is $\sim 10^6$ m/s and ballistic transport with mean free paths of up to a micrometer have been observed[23] at room temperature.

An additional quantum number called pseudospin is present in graphene and arises from the chiral nature of the massless Dirac fermions' Hamiltonian[21]. States at the K

and K' points (opposite corners of the Brillouin zone) have opposite pseudospin. The two-dimensional confinement of carriers in graphene means that phenomena such as the quantum Hall effect (QHE) and Berry's phase can be observed[24]. Due to the unique nature of charge carriers in graphene, such as the property of pseudospin, other quantum effects like the anomalous QHE (with a Landau level at 0), half-integer and QHEs can be observed[25, 26]. The chiral nature of electrons in graphene[27, 28] means it exhibits the interesting Klein effect[21] whereby electrons have a 100% tunnelling rate through potential barrier of any size. The 2010 Nobel prize was awarded to the Graphene co-discoverers[8].

2.1.2 Crystallographic Structure

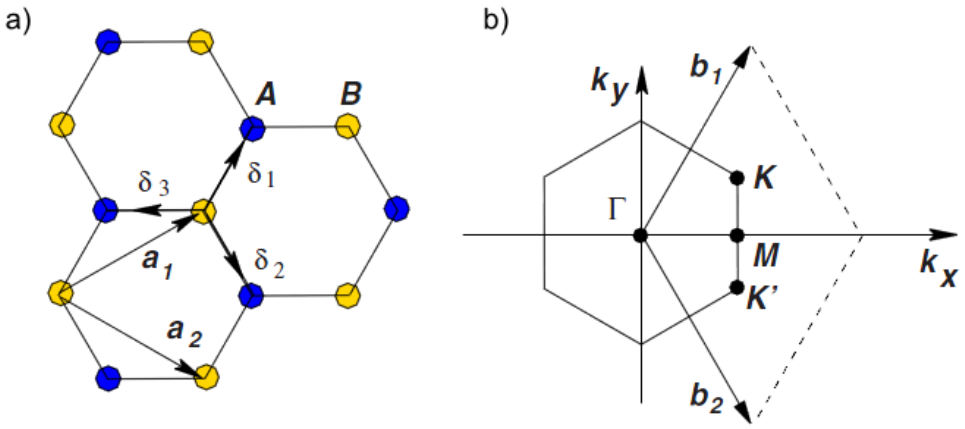

Figure 2.2: (a) The graphene lattice and (b) reciprocal space. a) The hexagonal lattice of graphene is comprised of two triangular lattices A and B with unit lattice vectors $\mathbf{a}_1$ and $\mathbf{a}_2$ and three nearest neighbours $(\delta_1, \delta_2, \delta_3)$. b) The reciprocal space with Brillouin zone centre, edge and corners labelled Γ, M, K and K' respectively. The reciprocal lattice parameters are $\mathbf{b}_1$ and $\mathbf{b}_2$[21].

The honeycomb structure of graphene can be constructed by combining two triangular sublattices[21]. Figure 2.2 (a) shows the two lattices labelled A (blue) and B (yellow) which make up the honeycomb structure. The length of a carbon-carbon bond in graphene is a =1.42 Å. The lattice vectors for each sublattice, describing the position of one atom to the next are:

$$\mathbf{a}_1 = \frac{a}{2}(3, \sqrt{3}), \qquad \mathbf{a}_2 = \frac{a}{2}(3, -\sqrt{3}), \tag{2.1}$$

and are shown in Fig. 2.2 (a). The unit cell of graphene, the smallest unit possible to describe the crystal structure, consists of one atom from each of the interlinked triangular lattices. Figure 2.2 (b) shows the construction in reciprocal space along with the Brillouin zone. The reciprocal-lattice vectors are

$$\mathbf{b}_1 = \frac{2\pi}{3a}(1, \sqrt{3}), \qquad \mathbf{b}_2 = \frac{2\pi}{3a}(1, -\sqrt{3}), \tag{2.2}$$

and are shown in the figure. Special points in the Brillouin zone are labelled $\mathbf{\Gamma}$, $\mathbf{M}$, $\mathbf{K}$ and $\mathbf{K}'$ corresponding to the centre, edge and corners of the Brillouin zone respectively. The $\mathbf{K}$ and $\mathbf{K}'$ points are of significant importance as they are the locations of the Dirac points where all the interesting Physics takes place, similar to the importance of the Γ point in 2D semiconductor physics[20].

2.1.3 Electronic Structure

The electronic band dispersion of single layer graphene was calculated even before the material was experimentally discovered, due to research into band theory of graphite[9]. The tight-binding approximation approach is used with the second-nearest neighbour hopping terms included in the Hamiltonian[21]. This approach yields an energy dispesion $E(k)$ given by[9]:

$$E_{\pm}(\mathbf{k}) = \pm t\sqrt{3 + f(\mathbf{k})} - t' f(\mathbf{k}), \tag{2.3}$$

where

$$f(\mathbf{k}) = 2\cos\sqrt{3}k_y a + 4\cos\frac{\sqrt{3}}{2}k_y a \cos\frac{3}{2}k_x a,$$

where t and t' are the nearest (A - B sublattice) and next nearest-neighbour (A - A or B - B sublattice) hopping energies respectively, with $t(\approx 2.5$ eV$) \gg t'(\approx 0.1$ eV$)$[20]. Figure 2.3 plots the result of equation 2.3. It can be seen how the band structure becomes linear where the cones touch around the K point and the valence and conduction bands intersect with the Fermi level lying at the intersection. At the Dirac points the dispersion relation is given by[21] $E = \hbar k v_F$ as opposed to the usual parabolic structure[29] with $E = \hbar^2 k^2/2m^*$. Interestingly the Fermi velocity, v_F which describes the linear bands, is independent of energy and momentum[21] ($v_F = \sqrt{2E/m}$ for the

usual case) and is given in the tight-binding solution as $v_F = 3ta/2\hbar \approx 10^8$ cm/s or 1/300 the speed of light.

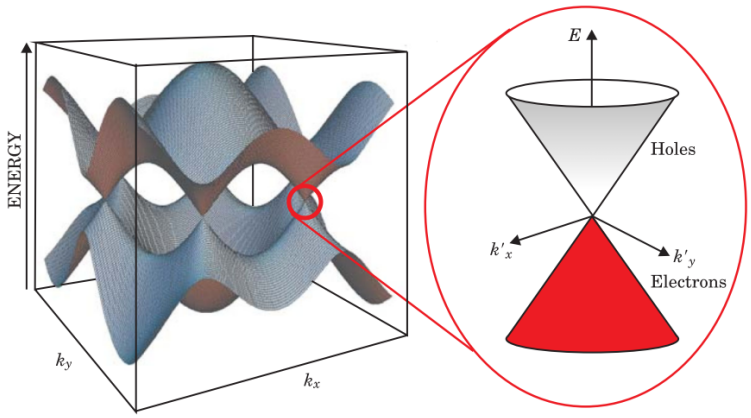

Figure 2.3: Dispersion relation of electrons in graphene with the inset showing the linear bands around the K point[30]

There is no band gap in single layer graphene making it a zero-gap semiconductor. Typical graphene samples have some level of electron or hole doping that shifts the Fermi level up or down from the crossing point, increasing the conductivity. Gates can be fabricated onto graphene devices that allow the Fermi level to be controlled by applying a gate voltage[8], V_g. Figure 2.4 (a) shows how the measured resistivity sharply peaks when the Fermi level lies at the intersection of the conduction and valence band (Dirac point) when there are no free carriers for electronic transport.

The tight binding approach has also been applied to bilayer graphene where two monolayers are weakly coupled by interlayer hopping and stacked in an AB arrangement for graphite[31]. Figure 2.5 shows the dispersion relation around the K point, which consists of two parabolic valence and conduction bands that touch at $E = 0$. Applying an external bias breaks the equivalence of the two layers[21] and a band gap opens up near the K point[32] as seen in Fig. 2.5 (b)

The Density of States, DOS (number of available states to occupy per unit volume and energy) is affected by the linear band structure. In a conventional 2D semiconductor such as GaAs the DOS is given by $D(E) = m/\pi\hbar^2$ and is independent of energy. For graphene near the K point $E = \hbar k v_F$ can be used instead of $E = \hbar^2 k^2/2m$ and the DOS becomes:

$$D(E) = \frac{2E}{\pi(\hbar v_F)^2}. \tag{2.4}$$

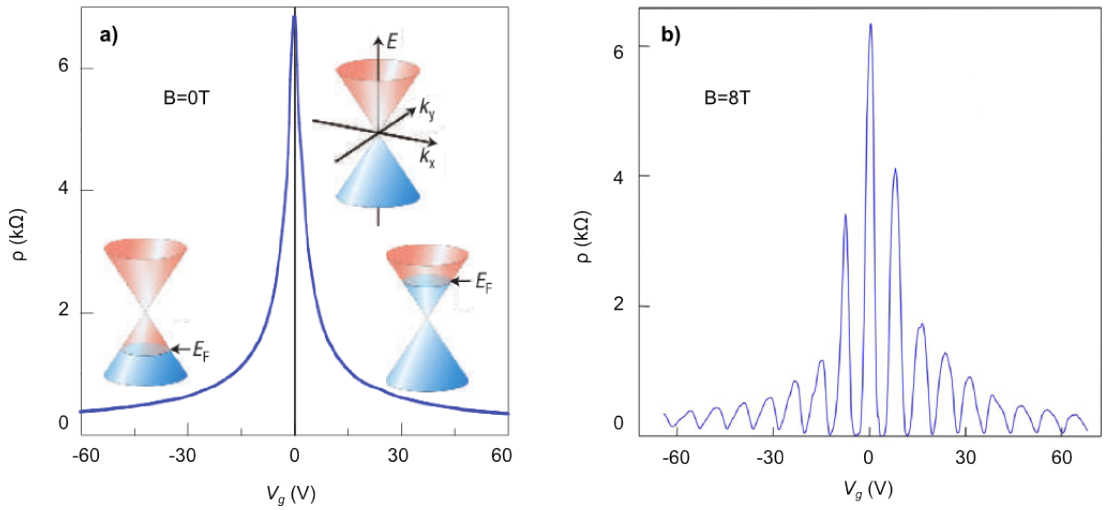

Figure 2.4: Electronic measurement of gated graphene[22] showing (a) the longitudinal resistivity of a graphene Hall bar device at 4K in zero magnetic field and (b) applied magnetic field. Applying a gate voltage, V_g induces electrons or holes in graphene and applying a magnetic field creates quantised energy levels. The diagrams in (a) show the position of the Fermi energy E_F, as the gate is varied from negative to positive. It is assumed that at $V_g = 0$ the sample is undoped, and E_F lies at the Dirac point

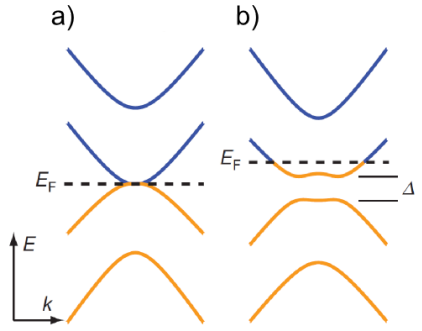

Figure 2.5: (a) Dispersion relation of electrons in bilayer graphene around the K point and (b) dispersion relation with a gate voltage V_g applied that introduces a band gap[33].

Figure 2.6 shows the DOS for graphene compared to a typical 2D system with parabolic band structure. This can be used to calculate the carrier density by integrating up to the Fermi level:

$$n = \int_0^{E_F} D(E)\ dE = \frac{E_F^2}{\pi(\hbar v_F)^2} = \frac{k_F^2}{\pi}, \tag{2.5}$$

assuming a temperature of $T = 0$, where all charge carries are in their lowest states filled up to the Fermi level.

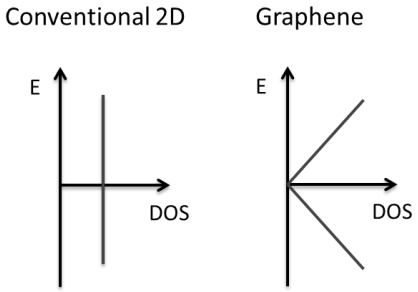

Figure 2.6: Density of states for typical 2D systems and graphene. The linear band structure of graphene gives it a different DOS compared to a typical 2D semiconductor with parabolic bands

Applying a perpendicular magnetic field B causes electrons to occupy quantised energy levels (Landau Levels). For a two-dimensional electron gas these are[29]:

$$E_N = \hbar\omega_c(N + \frac{1}{2}) \tag{2.6}$$

where $\omega_c = eB/m$ and N is an integer which labels the different Landau levels. The density of states in 2D is then split into a series of delta functions separated by $\hbar\omega_c$ and having zero DOS at $E_N = 0$. Not surprisingly the Landau levels in graphene are different due to its unique properties. As the electrons behave as Dirac Fermions, the cyclotron frequency is given by[21]:

$$\omega_c = \sqrt{\frac{2eB}{c}} v_F \tag{2.7}$$

and the energy levels are given by[21]:

$$E_N = \pm v_F \sqrt{2e\hbar BN}, \tag{2.8}$$

where $+/-$ describes electrons/holes. The result differs for the usual 2D case in several

ways. First, for $N = 0$ there is a energy level at $E = 0$. Figure 2.4 (b) shows the Shubnikov de Haas oscillations in the resistivity for a graphene device in a magnetic field at 4 K. The resistivity oscillates as the gate is swept and E_F passes through the Landau levels. It can be seen that there is a level at $E = 0$ from the peak around $V_g = 0$ where E_F is at the Dirac point. Secondly, the energy levels scales with $\sqrt{B}$ instead of linearly with B, which allows the quantum Hall effect to be observed at room temperature[21].

When measuring in a magnetic field, equation 2.8 can be used to obtain the carrier density or Fermi energy. As the magnetic field is swept, when the gate voltage V_g is constant, the resistivity will oscillate when passing through the Landau levels (the reverse case of varying V_g and keeping B constant as shown in Fig.2.4 (b)). By identifying two values of magnetic field, B_1 and B_2 that correspond to adjacent Landau levels we get from equation 2.8:

$$v_F\sqrt{2e\hbar B_1 N} = E_F \tag{2.9}$$

and

$$v_F\sqrt{2e\hbar B_2(N+1)} = E_F. \tag{2.10}$$

Using $E_F = \hbar k_F v_F$ and rearranging for N gives:

$$N = \frac{\hbar k_F^2}{2eB_1}, \tag{2.11}$$

$$N + 1 = \frac{\hbar k_F^2}{2eB_2}. \tag{2.12}$$

Subtracting the first from the second and using equation 2.5 gives:

$$1 = \frac{\hbar\pi n}{2e}(\frac{1}{B_2} - \frac{1}{B_1}) \tag{2.13}$$

$$n = \frac{4e}{h(\frac{1}{B_2} - \frac{1}{B_1})} \tag{2.14}$$

2.1.4 Fabrication of Graphene

2.1.4.1 Mechanical Exfoliation

Graphene was first isolated using the mechanical exfoliation or 'Scotch Tape' method[8] whereby layers of graphene are simply separated from graphite using adhesive tape and deposited onto a substrate, usually sillicon with an oxide layer (Si/SiO_2). Layers in

graphite easily cleave due to weak interplanar bonds. For this reason graphite has been used as a lubricant in industry and pencil lead for years. Simply pushing a graphite based pencil across a page as one does when writing should lead to the production of graphene. The key to isolating graphene however is being able to find it amongst the many graphite flakes produced during cleavage. Graphene becomes visible under an optical microscope when placed on a dielectric substrate of certain thickness, due to interference effects[34, 35, 36]. This allows instant identification of graphene amongst the many graphite flakes produced during exfoliation, simply making use of the human brain to quickly distinguish between different contrast levels. The technique is not suitable for large scale industry, but exfoliated graphene produces the highest quality graphene which is suitable for fundamental research. The adhesive tape and type of graphite used affect the size of resulting flakes. To achieve the highest quality graphene, adhesive tape that leaves little or no glue residue is desired. For the largest sized graphene flakes exfoliation from natural graphite is best, producing flakes up to 1 mm[37], as opposed to HOPG. Graphene remains attached to the substrate due to van der Waals forces with an adhesion strength of 0.45 J/m for SiO_2[38].

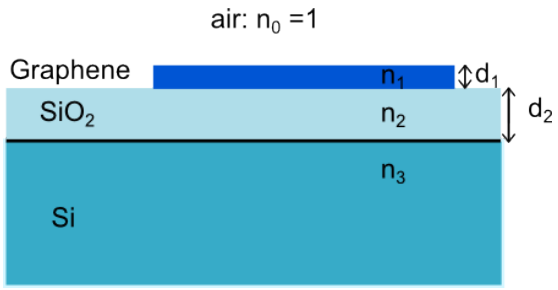

Figure 2.7: Thin film model of graphene on a silicon substrate with a SiO_2 oxide layer required to enhance the optical contrast of graphene. The reflectance of graphene depends on the refractive index n and thickness d of each layer, as light is reflected or transmitted at each interface.

Visibility after Exfoliation The mechanical exfoliation technique requires the exfoliated graphene to be placed onto a suitable substrate. Graphene was visible when it was first isolated due to a 300nm thick oxide layer on the silicon surface so that light reflected from the silicon travels a fraction of a wavelength further and interferes with light reflected from the graphene surface, analogous to rainbow patterns seen in oil floating on water. Analysis of the system revealed changing the oxide thickness or using

monochromatic light to illuminate the graphene had dramatic effect on its visibility[35]. For a double layer film system (graphene and SiO_2 on semi-infinite Si) shown in Fig. 2.7, the reflected light intensity for normally incident light is given by[39]:

$$R(n_1) = |\frac{r_1 e^{i(\theta_1+\theta_2)} + r_2 e^{-i(\theta_1-\theta_2)} + r_3 e^{-i(\theta_1+\theta_2)} + r_1 r_2 r_3 e^{i(\theta_1-\theta_2)}}{e^{i(\theta_1+\theta_2)} + r_1 r_2 e^{-1(\theta_1-\theta_2)} + r_1 r_3 e^{-i(\theta_1+\theta_2)} + r_2 r_3 e^{i(\theta_1-\theta_2)}}|^2, \tag{2.15}$$

where

$$r_1 = \frac{n_0 - n_1}{n_0 + n_1}, \qquad r_2 = \frac{n_1 - n_2}{n_1 + n_2}, \qquad r_3 = \frac{n_2 - n_3}{n_2 + n_3},$$
$$\theta_1 = 2\pi n_1 d_1/\lambda, \qquad \theta_2 = 2\pi n_2 d_2/\lambda.$$

The refractive indices for Si and SiO_2[40] are complex and vary with λ. For graphene $d_1 = 0.34$ nm and the refractive index of graphite, n_1=2.6−1.3i, can be used as it is found to fit well with experimental data[34, 35]. Contrast of the graphene compared to the rest of the wafer is a more useful and measurable quantity. It is defined as the relative intensity of light reflected from graphene compared to that reflected from the same substrate with no graphene ($n_1 = n_0 = 1$):

$$C = \frac{R(n_1 = 1) - R(n_1)}{R(n_1 = 1)}. \tag{2.16}$$

Figure 2.8 shows a plot of the contrast as a function of wavelength and SiO_2 thickness. Regions of maximum and minimum contrast are clearly visible from the colour plot. Experimentally, substrates with an oxide layer of 90 nm or 300 nm are most commonly used to maximise contrast and make identification under an optical microscope possible. Filters are also used so that only a certain wavelength of light is incident on the sample. Although SiO_2 is widely used it is not the only material that can act as an optical buffer and enhance the contrast of graphene. It is possible to use other dielectric substrates[36] and also metallic substrates with a suitable thickness of polymethylmethacrylate (PMMA) instead of an oxide layer[41].

2.1.4.2 Other Fabrication Routes

Extensive research has shown graphene can be fabricated via methods other than mechanical exfoliation, such as intercalating graphite to expand the graphene separation followed by sonicating to cause deintercalation and separate the graphene layers[42];

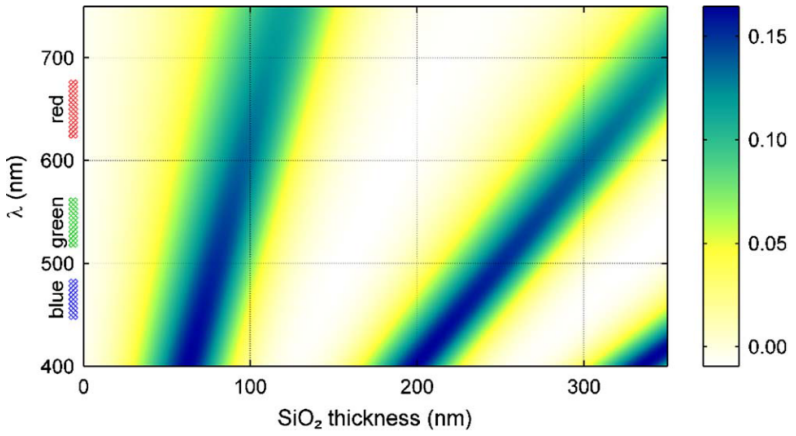

Figure 2.8: Optical contrast of monolayer graphene on a Si substrate with a SiO_2 layer and incident light of wavelength λ, given by equations 2.15 and 2.16. Maxima in the contrast can be seen, for example when λ ~600 nm (green light) and the SiO_2 layer thickness is ~300 nm.

or choosing appropriate solvents that will exfoliate graphite and leave colloidal suspension of graphene films after sonication[43]. Graphite oxide can also be reduced into graphene monolayers[44], this usually produces low quality graphene due to the difficulty of removing the oxygen bonds.

Epitaxial growth of graphene involves silicon carbide (SiC) and can produce wafer sized graphene sheets[45]. SiC is heated to high temperatures (1200-1600 °C) where the silicon sublimates leaving epitaxial graphene to form. Chemical Vapour Deposition (CVD) has also been used to produce large-scale graphene sheets suitable for future industrial production[46]. Again using high temperatures, carbon atoms are dissolved and precipitate onto a metallic surface on cooling. The number of graphene layers can be controlled by the cooling rate and hydrocarbon gas concentration. Copper foils are usually used as their low carbon solubility enables monolayer graphene to be grown[47]. Graphene films up to 30 inches in diameter have been reported deposited onto copper foils with 97% optical transmittance, 125 Ω sheet resistance and are high enough quality to produce the half integer quantum Hall effect[47].

2.2 Graphite Intercalation Compounds

2.2.1 Overview

The AB stacking (see inset of Fig. 2.9) of graphene results in the construction of Graphite. Graphite is anisotropic with weak interplanar bonding but strong in-plane bonds for the individual graphene layers. This allows for the modification of graphite, where different chemical species are inserted between the graphene layers, known as Graphite Intercalation Compounds (GICs). The first discovery of a GIC was made in 1841 and over the years many reagents have been found that successfully intercalate, producing GICs ($\gg$ 100 different chemical species[48]). Whether or not a compound can be used to form a GIC depends on geometrical factors such as intercalate size and length of bonds[48]. The inserted chemical species, referred to as intercalate, causes the distance between adjacent graphene layers to be expanded from c_0 $\approx$3.35 Åto d_s, which varies by intercalate (see table 2.1). Upon intercalation the graphene layers themselves remain intact despite having their c-axis spacing increased. The intercalate structure remains mostly the same and can be commensurate or incommensurate with the graphite host[48].

Natural graphite flakes are good quality single crystals, however they are usually too small (2 mm $\times$ 2 mm $\times$ 0.5 mm) to be used for GICs . Highly oriented pyrolytic graphite (HOPG) is most commonly used, due to it having dimensions an order of magnitude larger. HOPG is synthesised using high temperatures and pressure to create graphite that is well oriented in the c-axis but in-plane consists of many crystallites $\sim 1\mu$m in diameter. An alternative to HOPG is Kish which is a by-product of the steel industry, which consists of several large crystallites and has suitable dimensions for intercalation.

Graphite is a semi-metal with zero band gap and when intercalated is metallic in behaviour as intercalate layers transfer charge to the adjacent graphene layers shifting the Fermi level from the neutrality point[49]. GICs are categorised as either acceptors or donors depending on if the intercalate transfers holes or electrons to the graphite host respectively. This thesis concentrates on acceptor type transition metal chlorides as the intercalate, part of a group known as the magnetic GICs since the unpaired electrons in transition metals can form a 2D lattice of magnetic moments. The addition of an intercalate can cause significant changes to the electrical, thermal and magnetic properties of the host graphite. Insulating behaviour can be seen along the c-axis for

certain acceptor compounds[48] while superconducting behaviour is possible for some GICs such as the stage-1 C_8K GIC[50] even though superconductivity is not found in pure potassium.

The intercalate layer is not always present between every graphene layer, remarkably a GIC forms with set number of graphene layers separating each intercalate. This number is known as stage index, n and is one of the key features of GICs. So a GIC with intercalate separating every graphene layer is a stage-1 compound. Figure 2.9 illustrates GICs with different stage numbers. The c-axis repeat distance of a GIC is given by:

$$I_c(\text{Å}) = d_s + c_0(n-1) \tag{2.17}$$

where c_0 =3.35 Åand for stage-1 we simply get $I_c = d_s$. Interestingly GICs have been formed that are up to stage-8[51], and so have a repeat distance of over 30 Å[49]. The staging phenomena is thought to arise due to strain in the system[48] as opposed to electrostatic effects, since graphene layers adjacent to intercalate effectively screen the charge from the other layers[52, 53]. Several techniques are available to characterise GICs. Simple observation of colour change and measurement of weight uptake can give initial information on the intercalation process. Staging can be estimated from weight uptake measurements if the chemical formula is known but assumes that the GIC is intercalated homogeneously. Structural information can be gained from X-ray and neutron scattering techniques. Diffraction patterns due to the intercalate and graphite host can be observed and analysed. Performing a (00l) X-ray reflection measurement on a GIC determines the repeat distance, I_c and hence stage index n. As n increases, the interaction between adjacent intercalate layers becomes weaker as the distance between them increases. This leads to a crossover from 3D to 2D behaviour and so the intercalate layer can be studied as a model 2D system.

Weight uptake measurements of the bulk MCl_2-GICs reveal incomplete intercalate coverage[21], characterized as a *filling factor* of f = 70-85%. From structural measurements it is believed that there are domains of intercalate and possibly the excess Cl^- ions are distributed on the perimeter of the domains [54, 55] making these intercalates acceptor-type. The widths of the in-plane neutron and X-ray diffraction peaks provide a measure of the domain size, which range from 450 to 1200 Åin $CoCl_2$ GICs studied by neutron scattering[56].

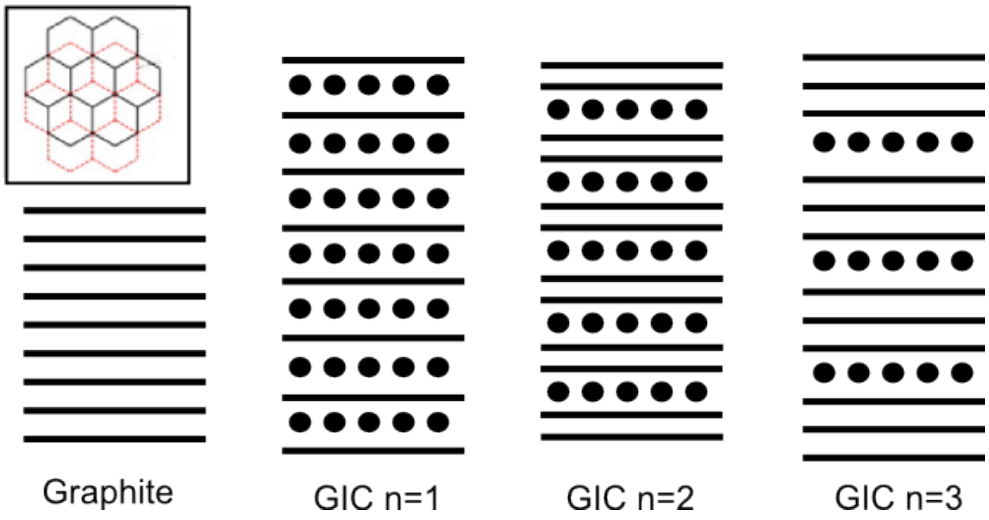

Figure 2.9: Staging in graphite intercalation compounds where graphene layers are represented by solid lines and intercalate layers by solid circles. The number of graphene layers separating an intercalate layer is given by the stage index, n. The inset shows AB staking of two graphene lattices.

Further evidence of domains comes from in situ X-ray measurements, while changing the intercalation parameters[57]. These have shown phase transitions are possible from stage n to stage n±1. The Daumas-Hérold model[57] was proposed to explain this phenomenon without the need for intercalate to switch layers, entering and leaving at the edges or somehow passing through the graphene layers. Figure 2.10 shows the domain model for a stage-3 GIC. The intercalate forms domains that align with domains from other layers in order to retain the stage-3 structure. In this model during GIC synthesis intercalate enters between every graphene layer forming domains and aligning to create the staging effect; as opposed to entering only every third layer in a perfectly homogenous stage-3 GIC as shown in Fig. 2.9. The model also allows for the observed phase transitions to different stage numbers by realigning the domains as intercalate can be added or removed to all layers. The interface between two intercalate domains has been observed by imaging the side of a $FeCl_3$ GIC with an electron microscope[58].

A theoretical consequence of the Daumas-Hérold domain model is Hendricks-Teller (HT) disorder[59] whereby stage disorder occurs along the c-axis. This results in macroscopic regions of the GIC being stage-n while other regions are stage-n±1, creating a mixed stage sample.

In general GICs are very unstable in air. Donor compounds become oxidised and

acceptors easily desorb. The acceptor GICs used in this study are among the few known to be air stable[49], although the pristine intercalates without the graphite host are hygroscopic and very reactive.

Intercalate domains $\sim$1 μm in diameter have been observed to form between crystal imperfections[60]. These occur in residue compounds (de-intercalated GICs) and are thought to be due to intercalate trapped by defects that could not react with the air and de-intercalate , leaving behind intercalate islands. Figure 2.11 shows a representation of this kind of domain.

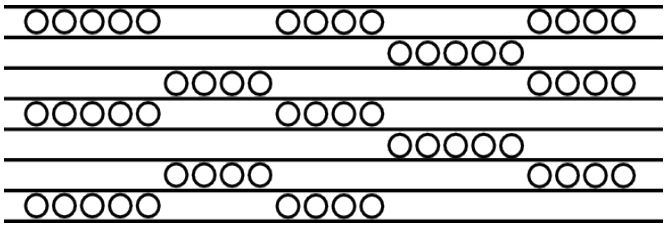

Figure 2.10: Representation of the Daumas-Hérold domain model for a stage-3 GIC showing intercalate forming in-plane domains but retaining the staging structure. The straight lines represent graphene layers and circles represent the intercalate.

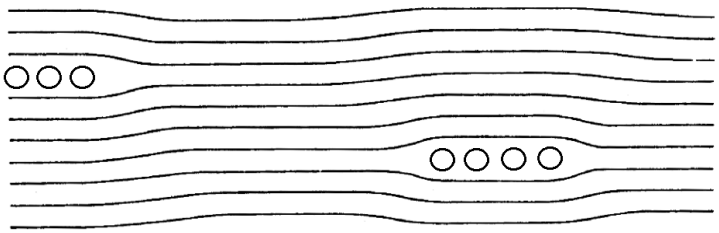

Figure 2.11: Representation intercalate islands for a GIC that has de-intercalated, with trapped islands of intercalate remaining[48]. Straight lines represent graphene layers and circles represent the intercalate.

Intercalate	d_s (Å)	Structure	a_0 (Å)
$CoCl_2$	9.38	$CdCl_2$	3.54
$MnCl_2$	9.47	$CdCl_2$	3.69
$NiCl_2$	9.42	$CdCl_2$	3.54
$CuCl_2$	9.40	monoclinic	3.30
$FeCl_3$	9.37	$FeCl_3$	6.06

Table 2.1: Structure Parameters[61] for the Transition Metal Chlorides used in this thesis.

2.2.2 Magnetic Graphite Intercalation Compounds

The intercalates used in this study are $FeCl_3$, $CoCl_2$, $CuCl_2$, $MnCl_2$ and $NiCl_2$. The process to synthesize the bulk GICs is discussed in section 3.1. Table 2.1 lists the lattice type and in-plane lattice constant for each intercalate in its pristine (non-intercalated) form. Figure 2.12 (a) shows the $CdCl_2$ structure which is also adopted by the Ni, Co and Mn anhydrous chlorides. It is a Cl-M-Cl trilayer structure (M=Co, Mn or Ni) consisting of M^{2+} ions in a triangular lattice, sandwiched between two close-packed layers of Cl^- ions. $FeCl_3$ has a similar structure but with a honeycomb lattice and larger lattice constants. $CuCl_2$ also has a trilayer structure, but is monoclinic in plane as the triangular lattice is distorted into isosceles triangles[7]. All the transition metal chlorides are incommensurate with the graphite host but are all oriented in-plane at either 0° or 30° (depending on the compound and stage index) to the graphene layers[61]. After intercalation the in-plane lattice constants of both the host and the intercalate are within 1.5% of their pristine values, and the distance between the metal and Cl layers is reduced by ∼6±3 %[61]. The AB stacking of graphite is modified such that it can be AA or AB either side of an intercalate layers, e.g. ABIAB or ABIBA (where I represents an intercalate layer)[48].

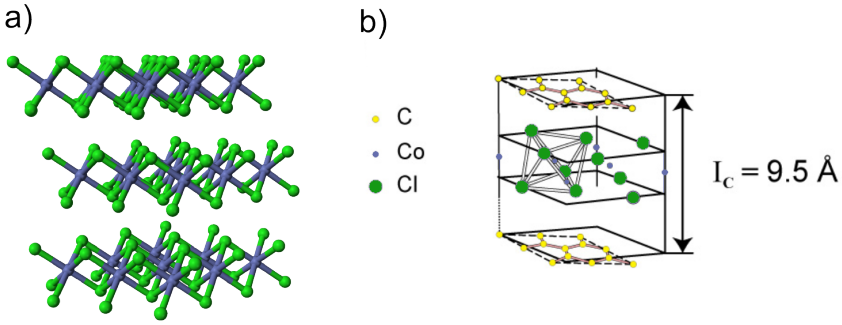

Figure 2.12: (a)The $CdCl_2$ structure that is adopted by the $CoCl_2$, $MnCl_2$ and $NiCl_2$ compounds. (b) Representation of a stage-1 $CoCl_2$-GIC with repeat distance I_c.

These magnetic GICs are layered magnetic materials with a Hamiltonian that consists of intraplanar J and interplanar J' exchange coupling terms. The magnetic Hamiltonian of the pristine samples are well known, with the exchange interactions measured by neutron scattering experiments. $CoCl_2$ GICs have received a lot of interest in the past due to their magnetic properties[7] and the magnetic Hamiltonian for pure $CoCl_2$

is[7]:

$$\mathcal{H} = -J\sum_{i<j}\mathbf{S_i}\cdot\mathbf{S_j} + J_A\sum_{i<j}S_{iz}S_{jz} + J'\sum_{i<k}\mathbf{S_i}\cdot\mathbf{S_k} - J'_A\sum_{i<k}S_{iz}S_{kz} - \mu_B\sum_i \mathbf{S_i}\cdot\mathbf{g}\cdot\mathbf{H}, \quad (2.18)$$

with $S = 1/2$, for a g factor in a magnetic field H and where J_A and J'_A are the intraplanar and interplanar anisotropy constants. The interplanar coupling terms (J', J'_A) are greatly reduced in GICs due to the graphene layers that separate the magnetic layers. After intercalation the intraplanar coupling terms (J, J_A) are expected to remain the same, as $CoCl_2$ retains its in-plane structure. This allows 2D theoretical behaviour to be studied such as the Kosterlitz Thouless transition in 2D XY ferromagnets. $CoCl_2$ GICs have been studied for this purpose but the phase transition expected at 10K has not been observed as the interplanar interactions cause 3D transitions as the in-plane spin-correlation length increases. A ultra-thin sample consisting of only one intercalate layer would exhibit purely 2D behaviour with $J' = 0$. The magnetic GICs in this study each have a unique classification: $CoCl_2$ - 2D XY ferromagnet with fictitious spin S=1/2, $NiCl_2$ - 2D Heisenberg ferromagnet with small XY anisotropy and S=1, $MnCL_2$ - 2D XY antiferromagnet on triangular lattice with S=5/2, $FeCl_3$ - 2D XY antiferromagnet on honeycomb lattice with S=5/2 and $CuCl_2$ - 2D XY antiferromagnet on isosceles triangular lattice with S=1/2[49].

2.3 Raman Spectroscopy

2.3.1 Introduction

In a crystal lattice, incoming photons can be scattered elastically or inelastically by phonons, the quantized lattice vibrations. For elastic scattering (Rayleigh scattering) the incident photon frequency ω_0 is equal to the scattered frequency. For inelastic scattering there is a change in energy between the incident and scattered photon. Raman scattering is the inelastic scattering of monochromatic light, usually from a laser in the UV-visible range. The excitation energy is chosen to be sufficiently small so as not to excite the system from the ground state to the first electronic excited quantum state (except for Resonant Raman Spectroscopy where the excitation length is chosen to match that of an electronic excited state). The light scattered by a vibrational mode is sent through an analyser and the frequency shift measured. The convention is to give

the shift in wavenumber (cm^{-1}), the reciprocal of the wavelength λ. Rayleigh scattering is the most probable event with the intensity of scattered light 10^{-3} less than the incident light and 10^{-6} for Raman scattered light [62]. The high intensity Rayleigh scattered light is filtered out to protect the sensitive detectors used for Raman spectrum measurement.

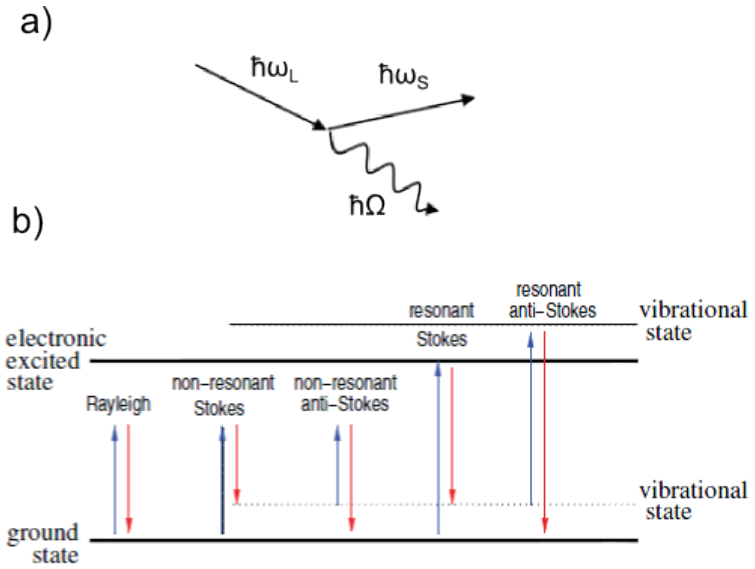

Figure 2.13: (a)Stokes Raman scattering process where a photon with energy $\hbar\omega_L$ scatters with a phonon (Ω) and leaves the system with energy $\hbar\omega_S$. (b) Energy diagram of Rayleigh, non-resonant Raman and resonant Raman processes[63].

Figure 2.13 outlines the Raman scattering process. An incident photon with energy $\hbar\omega_L$ excites an electron-hole pair so that the system is in a virtual state. The system then must emit a photon to return to the stable ground state. For elastic scattering the incident and scattered photon have the same energy but different direction of propagation. If a Raman scattering process occurs the scattered photon will lose some of its energy and exits with energy, $\hbar\omega_S$. Since the electron-hole pair returns to the same ground state the loss of energy is attributed to a phonon energy, $\hbar\Omega = \hbar\omega_L - \hbar\omega_S$, known as the Stokes process. The incident photon can also arrive at the system already in a excited state and gain energy by absorbing a phonon, referred to as anti-Stokes. Anti-Stokes photons are generally not used in Raman spectroscopy since the process is less probable than Stokes, producing less intense peaks in the Raman spectrum. Not all phonons can be probed by Raman spectroscopy. Vibrational modes are either Raman

or IR (absorption of infra-red radiation) active or both depending on their symmetry and application of IR and Raman selection rules[64].

For Raman scattering of a photon by a phonon, energy and momentum conservation gives:

$$\omega_L = \omega_S \pm \Omega$$

$$\boldsymbol{k_L} = \boldsymbol{k_S} \pm \boldsymbol{q}$$

where Ω and $\boldsymbol{q}$ are the frequency and wave vector of the phonon. Stokes is given by '+' and anti-Stokes by '−'. Experimentally the laser excitation used is 300 - 900 nm and the lattice parameter of the crystal is a ∼1-2 Å, therefore Raman spectroscopy only measures phonons around $q = 0$ (called the Γ point in graphene) for single phonon processes. Electrons as well as phonons are probed by Raman Spectroscopy, since scattering by phonons is influenced by electrons and mechanisms of scattering rely on electronic excitations as intermediary states instead of direct photon-phonon interactions.

Raman measurement is particularly useful as it is non-destructive and graphene based samples do not have to be specially prepared for measurement and can be taken at room temperature. The power of the laser is usually monitored and kept as low as possible to avoid any unwanted effects that may occur due to heating. Raman measurement is used on graphene samples to reveal structural and electronic information, and the good spatial resolution of modern Raman spectrometers allows Raman maps of graphene flakes to be created. Raman spectroscopy can also be used to identify staging in a GIC as discussed in section 2.3.3.

2.3.2 Raman spectroscopy of Graphene

Raman spectroscopy is a popular high resolution technique used for graphene research as it non-destructively provides information on the number and orientation of layers, defects, doping, strain, graphene edge type (armchair or zigzag) and other information[65]. A knowledge of Raman spectroscopy on graphene is applicable to the other graphene based materials such as nanotubes, graphite and GICs.

Due to the linear band structure around the K point in graphene (see Fig. 2.3), resonant Raman scattering occurs (see Fig. 2.13 (c)) for any excitation energy, producing intense peaks. Figure 2.14 shows the calculated[66] phonon dispersion for graphene,

essential to understand its Raman spectra. It consists of six bands arising from the two graphene sublattices: LO, iTO, oTO, LA, iTA and oTA. There are three optical (O) modes, referring to out-of-phase movement of the atoms in the lattice, one atom moving to the left, and its neighbour to the right. There are also three acoustic (A) modes, coherent movements of atoms of the lattice out of their equilibrium positions, such as in a sound wave. These can be longitudinal (L), transverse in-plane (iT) or transverse out-of-plane (oT). The iTO and LO are seen to be degenerate at the Γ point (corresponding to vibrations of sublattice A against sublattice B) and correspond to the E_{2g} representation[67]. Figure 2.15 shows the representation of the Raman active E_{2g} mode plus all other phonon modes in graphene and graphite.

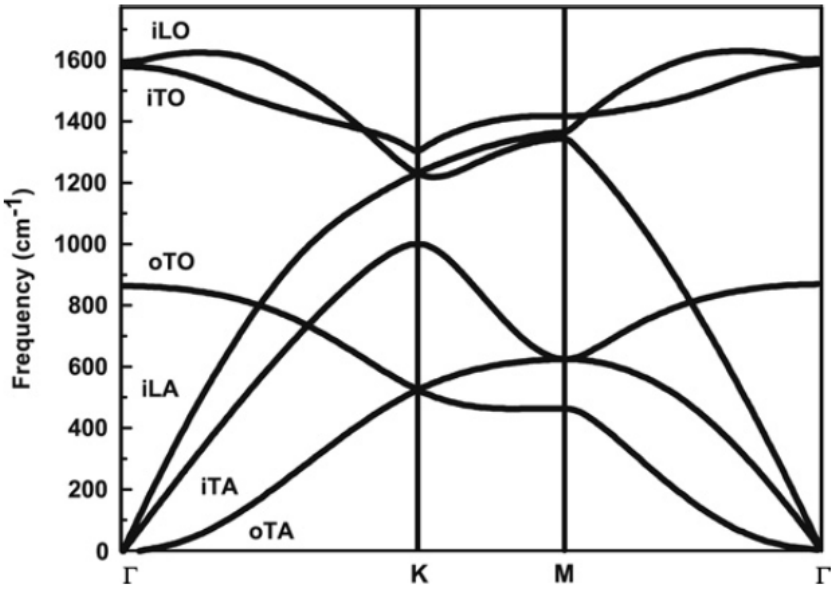

Figure 2.14: Phonon dispersion relation of graphene showing three acoustic (A) and three optic (O) phonon branches. Vibrations are in-plane (i) or out-of-plane (o) and longitudinal (L) or transverse (T) with respect to the A-B carbon-carbon directions. The degenerate LO and iTO branches at Γ produce the G peak in the Raman spectrum of graphene and graphite. [66].

2.3.2.1 The Main Features of the Spectrum

Figure 2.16 shows the main features from the Raman spectrum of graphene. The peaks seen also appear in graphite and other carbon forms such as carbon nanotubes[69]. The primary feature of the spectrum is the G band at ∼1580 cm^{-1}. This is due to

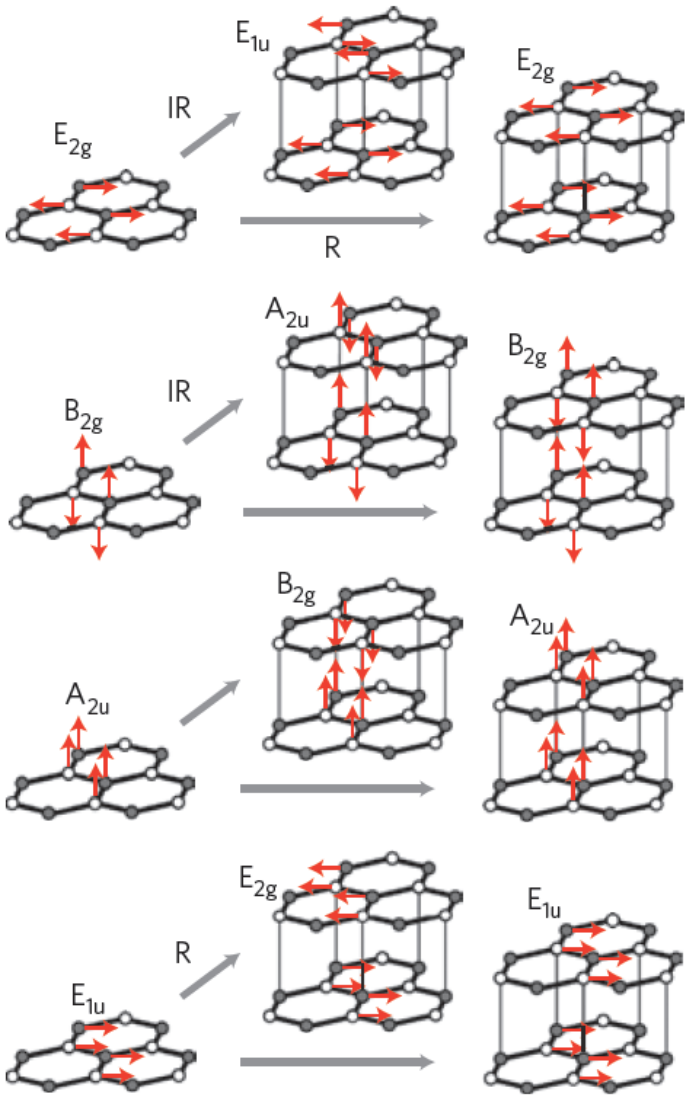

Figure 2.15: Representation of the phonon modes in graphene and graphite. The red arrows show the displacement of the carbon atoms and the atoms are shaded according to the sublattice they belong to[65]. The grey arrows indicate the equivalent mode in graphite and if the mode is Raman active (R), Infra-red active (IR) or inactive (unlabelled) according to group theory[68].

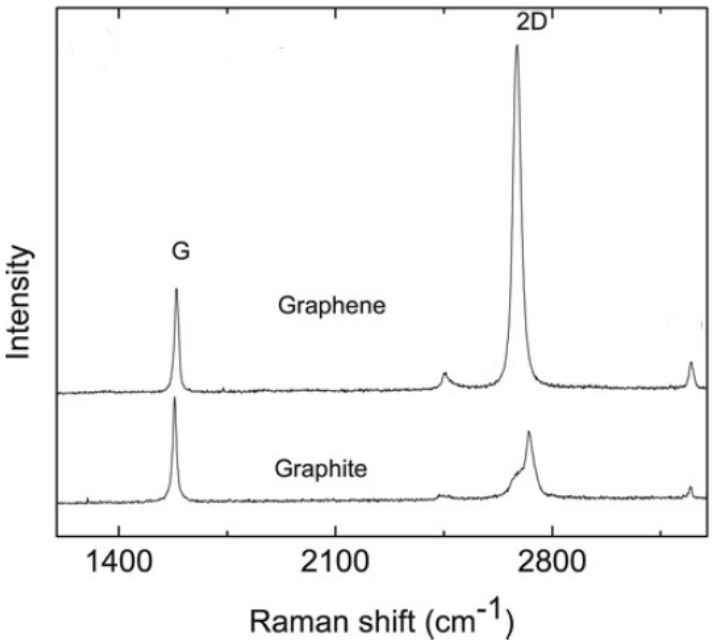

Figure 2.16: The Raman spectrum of graphene and graphite with the G and 2D peaks labelled. The spectrum was taken at 514 nm and have been scaled to show the same G peak intensity[63]. In graphene the 2D peak is more intense than the G peak and is narrower than the 2D peak of graphite.

scattering with the degenerate LO and iTO modes at Γ, seen in Fig. 2.14 (labelled E_{2g} in Fig. 2.15). The G peak is the only peak in the spectrum arising from a standard first-order Raman process, as described in section 2.3.1. The remaining peaks require several phonons with opposite $\boldsymbol{k}$ or a phonon and a defect in the disordered case. The Raman processes for all the peaks in graphene are outlined in Fig. 2.17.

Figure 2.16 shows the 2D peak at ∼2700 cm^{-1} for graphene and graphite. It arises from scattering from two iTO phonons at different but opposite Brillouin zone corners $\boldsymbol{k}$ and $\boldsymbol{k'}$ as represented in Fig. 2.17. The peak position is dispersive with excitation energy[65, 67], since exciting an electron to a higher quantum state requires an iTO phonon of lower momentum and hence energy to scatter it into the opposite Brillouin zone corner (see fig. 2.17). Historically (and somewhat confusingly) the 2D peak was labelled G' since it was the second most prominent peak observed in graphite samples[70].

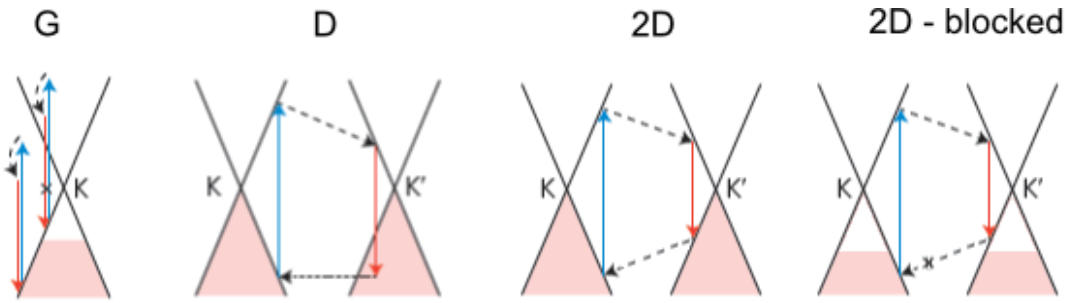

Figure 2.17: The electron-phonon processes for the G, D and 2D peaks of the Raman spectrum. Electronic transitions with blue and red arrows represent photon absorption and emission, a dashed arrow indicates scattering with a phonon and the horizontal dotted line is scattering with a defect. A cross indicates when a transition is not allowed due to a Fermi level shifted away from the Dirac point (doping). The processes responsible for the G peak takes place on the same Dirac cone whereas the processes for the D and 2D peaks take place across different K points[65].

Figure 2.18 shows the Raman spectrum at a Graphene edge. This spectrum has an additional D peak at ∼1350 cm^{-1} which is due to the breathing modes of six-atom rings and requires a defect and an iTO phonon for its activation[65, 67], as shown in Fig. 2.17. The D peak has been used to measure disorder in graphite samples and its absence is an indicator good defect-free graphene based samples.

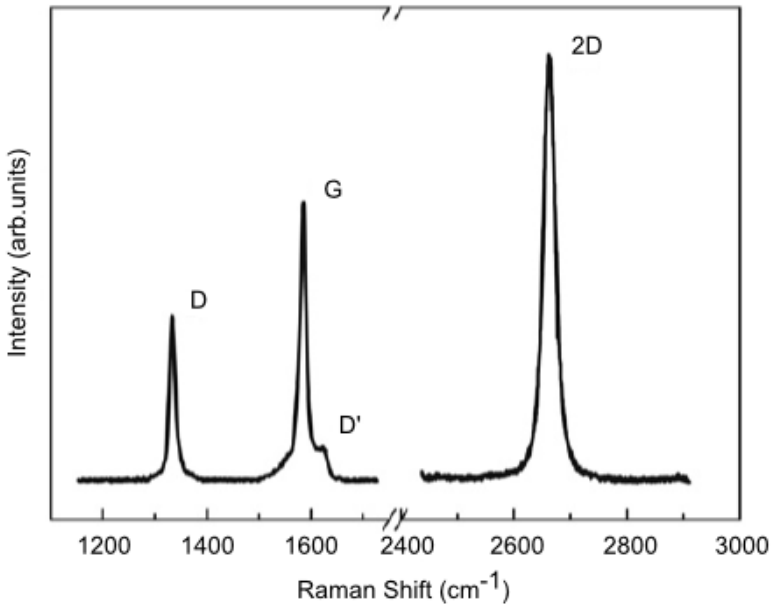

Figure 2.18: The Raman spectrum of a graphene edge measured at 2.41 eV. The edge causes disorder in the graphene lattice. The G and 2D peaks are observed[63] plus additional peaks labelled D and D' due to the disorder.

2.3.2.2 The Effects of Doping

The primary effect of electron or hole doping on the Raman spectrum of graphene is to move the G peak position due to stiffening or softening of the phonon modes[71, 72, 73]. As a result the G peak upshifts in wavenumber for p-type doping and downshifts for n-type doping[74]. However for low levels of doping, below $\sim 3\times10^{13}$ cm^{-2}, a modification of phonon dispersion near the Kohn anomaly causes the G peak to upshift for both p and n type doping[71, 72, 75], but the G peak position in n type doping returns to downshifting at higher levels of doping. The change in G peak position by doping has been observed for electronically gated bilayer[72] and single layer graphene[71, 76]. Figure 2.19 shows the change in G peak observed as doping in graphene is increased (via a back-gate). It is possible to estimate the charge carrier concentration in other samples by measuring the G peak position and comparing to plots such as Fig. 2.19. As well as a change in G peak position, the width of the G peak was found to be reduced but only at higher levels of doping when $E_F > \hbar\omega_L$.

Doping modifies the 2D peak intensity due to the interactions with electrons in a double resonant process requiring real electronic states[67]. Figure 2.17 shows that

when the Fermi level shifts beyond $|E_F| > (E_L - \hbar\omega_{2D})/2$ the 2D process cannot form the needed electron-hole pair, known as *Pauli blocking*. At these high levels of doping no 2D peak would appear in the Raman spectrum. It is possible to make use of this effect to get an estimate of shift in Fermi level to a graphene sample. The Raman spectrum can be taken for a range of excitation energies and the point found where lowering the excitation energy further results in no 2D peak being observed in the resulting spectrum.

When the excitation energy is sufficiently large compared to the Fermi level, so that Pauli blocking does not occur, the 2D peak intensity is found to decrease with doping due to a higher electron-electron scattering rate[77]. The area under the 2D peak (A(2D)) with respect to that of the G peak (A(G)) is given by[77]:

$$\sqrt{\frac{A(G)}{A(2D)}} = \frac{0.26}{\gamma_{e-ph}}[\gamma_{e-ph} + |E_F| f(e^2/\epsilon v_F)], \tag{2.19}$$

where γ_{e-ph} is the scattering rate due to the emission of phonons, ϵ the dielectric constant, and the function f is given in the appendix of [77].

2.3.2.3 Number of Layers and Orientation

The shape of the 2D peak can be used to determine the number of graphene layers (up to ∼5 layers) in a few layer graphene samples[63]. Above 5 layers the 2D lineshape becomes indistinguishable from graphite. The change in electronic band structure when moving from single layer graphene to several layers causes a change in 2D peak shape and intensity[63]. Figure 2.20 shows the evolution of the 2D peak with number of layers for several excitation energies. Figure 2.21 shows the four different Raman processes that are possible for bilayer graphene with its double band structure. This leads to a combination of four peaks, from each of the double resonant Raman processes, being used to fit to the measured 2D peak in bilayer graphene. The 2D lineshape continues to change as layers are added and the electronic band structure continues to change, eventually tending to that of graphite. The single linear bands in mono layer graphene means there is only one 2D process available which produces a single Lorentzian 2D peak. Additionally for the case of 1L graphene the process is triple resonant and leads to a 2D peak that is significantly more intense than the G peak[67], this feature makes Raman spectroscopy particularly useful for identifying mono layer graphene.

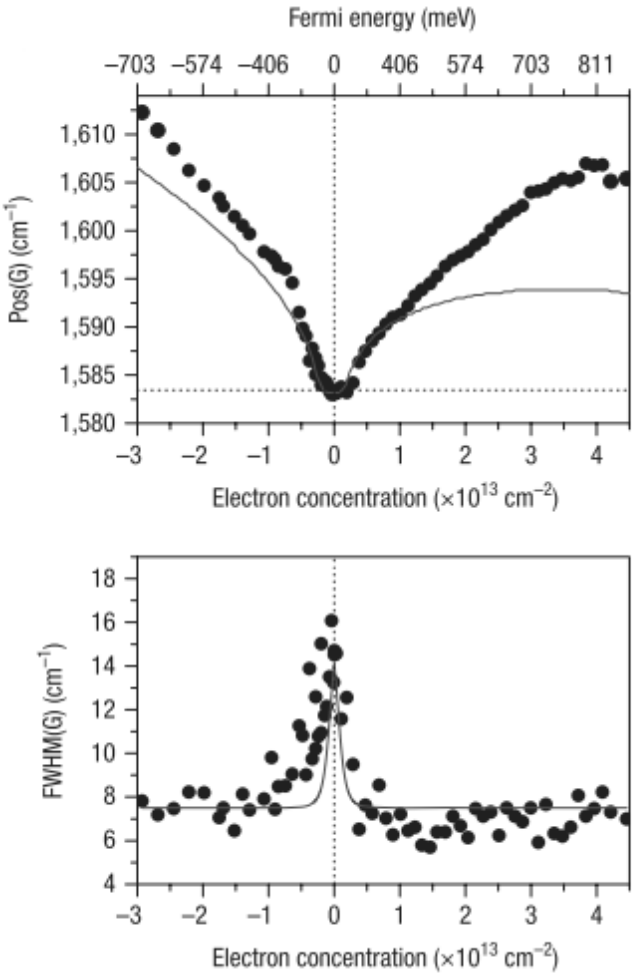

Figure 2.19: Raman measurement of monolayer graphene with a voltage applied to the back gate to control the electron concentration[71]. Measurements show the position and full width half maximum (FWHM) of the G peak to vary with electron concentration. The solid lines are predicted non-adiabatic trends[78]

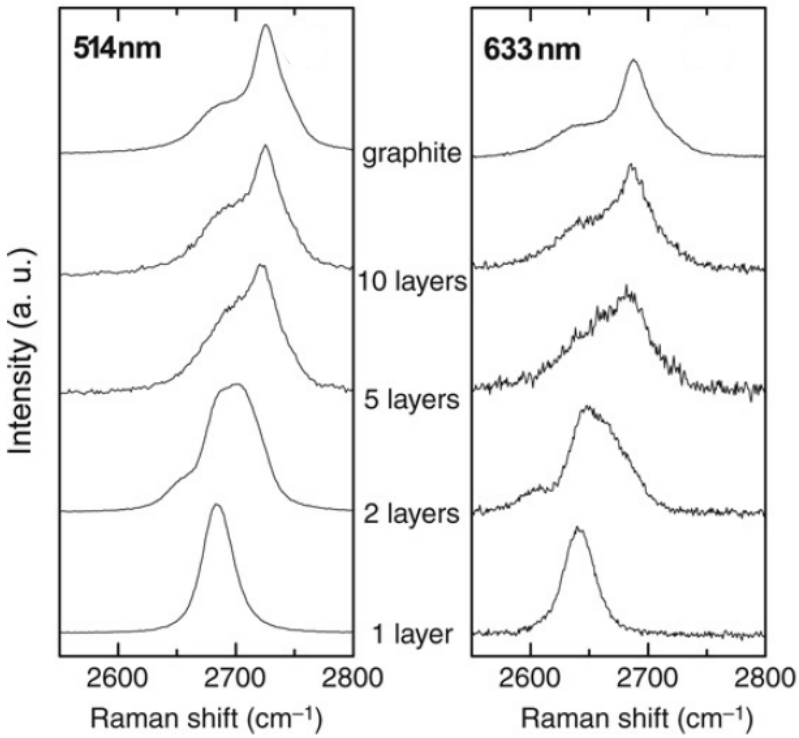

Figure 2.20: Evolution of the 2D peak for an increasing number of graphene layers. The 2D peak of the Raman spectra evolves from single peak in mono layer towards the structure seen in graphite. The measurements were performed with 514nm and 633nm laser light[63].

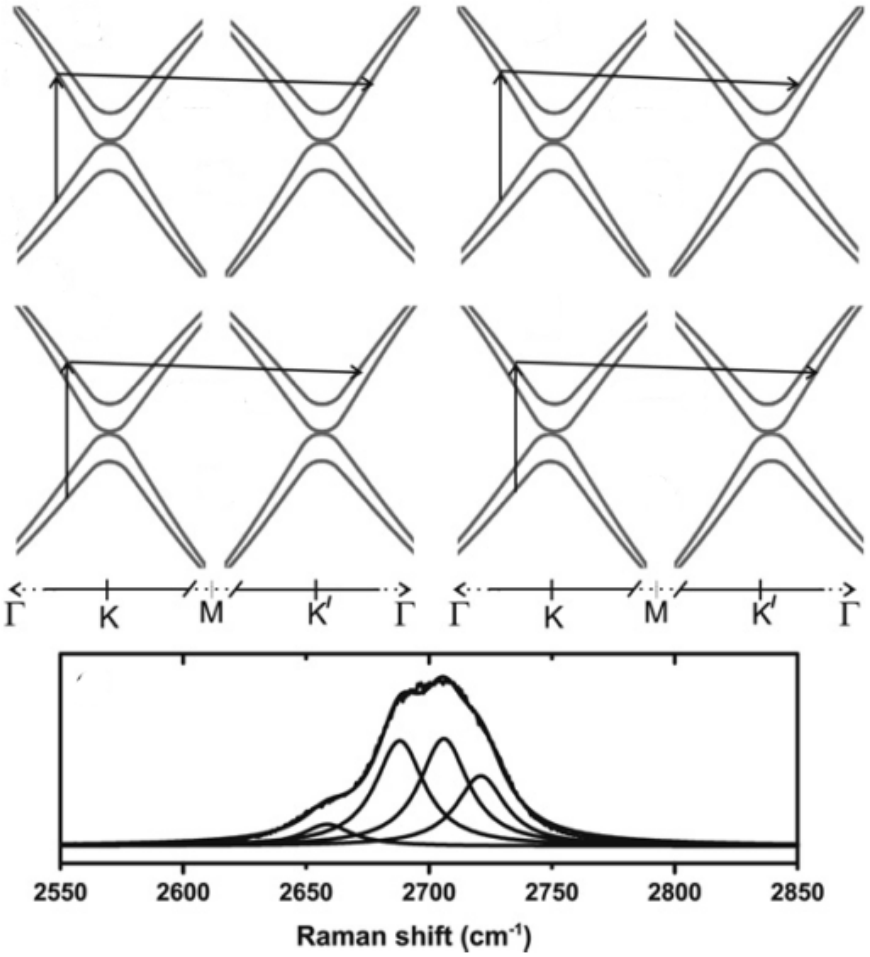

Figure 2.21: The 2D Raman process in bilayer graphene. (Top) The electron dispersion of bilayer graphene, the double band structure allows for four different possible phonon scattering processes, each with a different amount of momentum exchanged and energy lost. (Bottom) Raman spectrum showing the 2D peak of bilayer graphene measured at 2.41 eV, where the four different Lorentzian curves fit can be attributed to the four different different processes shown[79].

The 2D peak features outlined are valid when the graphene layers are Bernal AB stacked. For turbostatic graphite (unordered stacking) the difference in band structure leads to a single 2D peak but with FWHM almost double that of graphene and is upshifted by $\sim$ 20 cm^{-1}[80]. As well as turbostatic stacking, graphene stacked with a specific rotation between the layers have been studied[81]. Figure 2.22 shows the angle dependence on the Raman spectrum of misoriented bilayer graphene. The most obvious features are the 2D peak becoming more intense than the G peak (similar to the case for 1L) at 14° rotation, and the G peak becoming ~30 times more intense at 10° at 633nm. Furthermore the 2D peak position and FWHM are also sensitive to the relative angle between the layers[81].

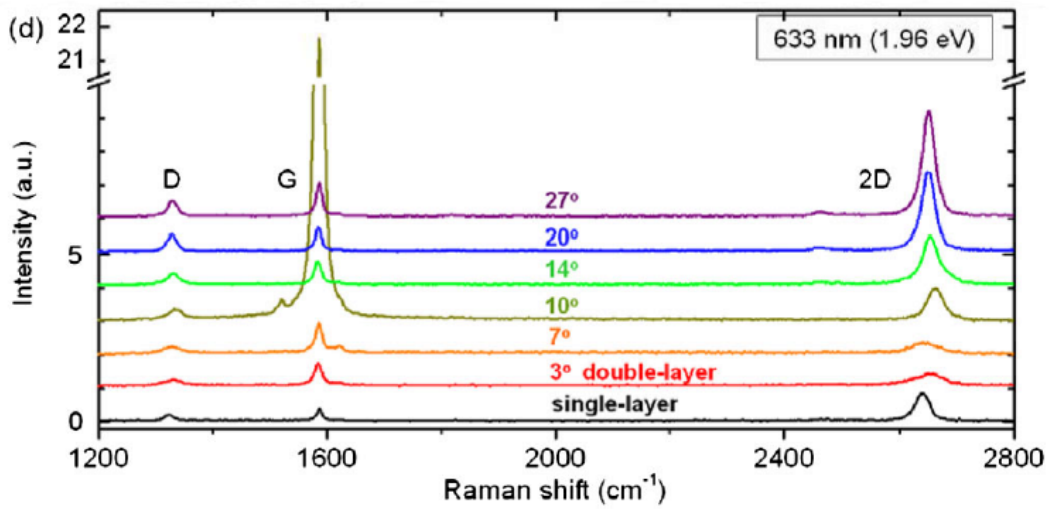

Figure 2.22: Raman spectrum of rotated bilayer graphene showing the D, G and 2D peaks when the graphene layers are misoriented by the specified angle[81]

There are other peaks besides the 2D peak that can be used to study the number of layers in graphene samples. A mode related to the shearing of the graphene sheets on top of one another leading to a so called C-peak has been observed at $\sim$ 42 cm^{-1}[82]. The intensity of this C peak scales directly with layer number and is not present in single layer. The peak is of limited practical use since the position is of such low frequency that it is usually below the notch filter that protects the measurement equipment from the intense Rayleigh scattered light.

2.3.2.4 Strain Effects

Raman measurements have shown that graphene placed under strain exhibits a change in G peak[83, 84]. Placing graphene under tensile strain usually softens vibrational modes, and the opposite occurs for compressive strain[65]. G peak position shifts of up to 14.2 cm^{-1} per 1% of strain have been observed[83]. Furthermore the G peak was split into two peaks[84, 85] due to components of the E_{2g} mode being parallel or perpendicular to the applied strain. When analysing the G peak care must be taken to distinguish between strain and doping, both of which can affect its position. Small amounts of strain can be caused by corrugations in a graphene sheet[86, 87], however it is placing graphene on a flexible substrate and applying pressure that introduces significant levels of strain required for the G peak to split into two components[83, 84].

2.3.3 Raman Spectroscopy of GICs

The Raman spectra of GICs are very similar to that of their graphite host. Figure 2.23 (a) shows the G peak of the Raman spectra for $FeCl_3$ GICs of different stage index. The stage-1 compound shows a single G peak upshifted to ~ 1626 cm^{-1}. For stage-2 a single peak around 1613 cm^{-1} is seen, and for stage-3 and above the G band has two components whose intensities change with stage number, but positions do not. The higher wavenumber component decreases with stage number and vanishes for graphite, whereas the low frequency peak coincides with the graphitic peak and is strongest in the dilute compounds. These observations led to the conclusion that the two peaks are due to interior (low wavenumber) graphene layers not adjacent to any intercalate layers and exterior (high wavenumber) graphene layers that are bound by intercalate[48]. There is no low wavenumber component of the G band for stage-1 and stage-2 compounds, as all the layers in these compounds are adjacent to one (stage-2) or two (stage-1) intercalate layers, and hence no interior graphene layers. The different G peak positions observed for Raman measurements[88] of $FeCl_3$ GICs are listed in Table 2.2.

Figure 2.24 shows the G band components plotted for both acceptor and donor compounds. Both types have two components for stage-3 and above but the trend is reversed for the donor compounds with both components becoming downshifted for lower stage GICs (more intercalate layers). This is consistent with the effect of doping on graphene described in section 2.3.2.2, where n-type doping causes a G peak upshift

and p-type doping a downshift. The difference in G peak position between stage-1 and stage-2 compounds can be explained by an increased level of doping for stage-1 compounds as the graphene layers are doped by intercalate on both sides compared to just one side in stage-2.

Peak	Description	$FeCl_3$ Position
G_0	Graphene not flanked by any intercalate. Pristine graphene	1585 cm^{-1}
G_1	Graphene flanked by intercalate on one side. Equivalent to a stage-2 GIC	1613 cm^{-1}
G_2	Graphene flanked by intercalate on both sides. Equivalent to a stage-1 GIC	1626 cm^{-1}

Table 2.2: Nomenclature used to describe the G peaks that appear in the G band of the Raman spectrum of GICs and FLGICs, identified by the number of intercalate layers flanking the graphene layer. In general G peak position increases as level of doping is increased. Samples with several graphene layers can have several peaks in the G band, e.g. the stage-3 GICs can be described by the scenario of one layer with G_0 doping and the other two G_1. Measured positions of the peaks are given for $FeCl_3$ GICs[88].

2.4 Review of $FeCl_3$ FLGIC Studies

Parallel to this thesis, bilayer graphene on SiO_2 substrates has been intercalated with $FeCl_3$ directly using the two zone transport by several groups[74, 89, 90, 91]. Typically the flakes were verified to be bilayer using the 2D lineshape in Raman spectroscopy before intercalation. Upon intercalation the G peak is observed to shift to around G_1 (1612 cm^{-1}) in [74, 89, 91] and beyond 1620 cm^{-1} towards G_2 in [90]. This extra upshift was attributed to intercalate on the surface and underneath the flake that along with a central intercalated layer would dope the graphene layers on both sides instead of just one. Rinsing the flake in acetone was seen to remove the exterior intercalate and reduce the position of the G peak in Raman spectrum to G_1. Direct $FeCl_3$ intercalation of 3L, 4L and 5L flakes was also achieved [74, 89, 91], creating extremely thin stage-1 GICs. Figure 2.25 shows the G band of Raman spectrum was found to split into G_1 and G_2 peaks in[89, 91]. Raman modes seen in pristine $FeCl_3$ between 100 and 300 cm^{-1} were also seen in the intercalated samples[74].

Changes in the 2D peak of Raman spectrum were also observed upon intercalation[74, 89, 90, 91]. Figure 2.25 shows how the 2D lineshape changed to that of a Lorentzian

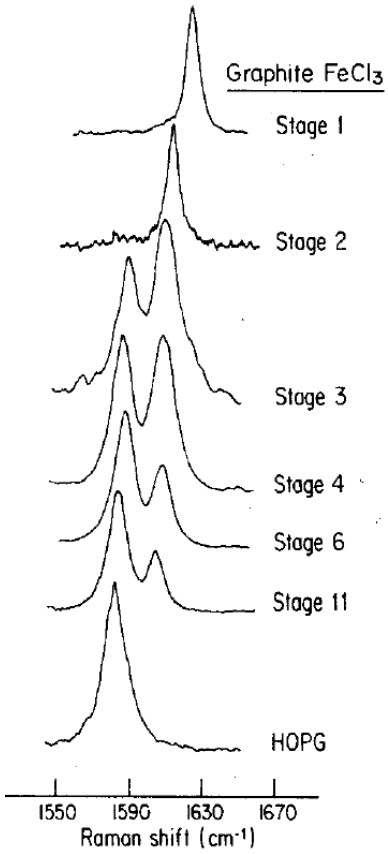

Figure 2.23: Raman spectrum of $FeCl_3$-GICs with stage index n measured at 488 nm[88]. The evolution of the G band with stage number is seen.

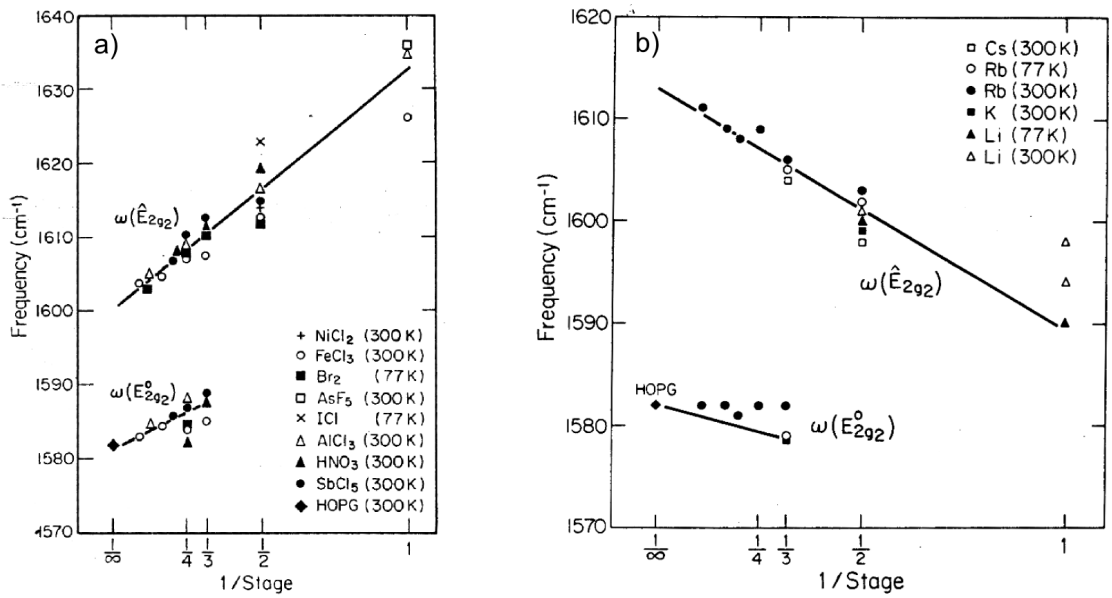

Figure 2.24: The position of the high frequency $\omega(\hat{E}_{2g})$ (G_2) and low frequency component $\omega(E^{\circ}_{2g})$ (G_1) of the G band are plotted for various a) acceptor and b) donor GICs against their reciprocal stage index[48].

peak after intercalation. The addition of the intercalate layers greatly increases the graphene separation, removing any coupling between the graphene layers resulting in their Raman spectrum and electronic structure matching that of single layer graphene.

The samples were found to remain intercalated for up to a year[91], despite the hygroscopic nature of $FeCl_3$. Evidence of partial deintercalation over several months was seen[74] as the G band gained an additional downshifted G peak towards the G_0 position. Some inhomogeneity of G peak position across the flakes was observed and studied[90] by producing Raman maps that suggest the formation of small $\sim$ 1 μm islands in the intercalate layer.

The intercalated flakes were fabricated into hall bar devices with a back gate to control carrier density[90, 91]. The resistivity across the samples was seen to increase as the temperature was lowered indicating metallic behaviour in contrast to graphene where resistivity decreases at the Dirac point. Figure 2.26 shows the results[91] where resistivity is significantly lower in intercalated samples compared to non-intercalated samples with the same number of graphene layers.

Additional measurements were performed in a magnetic field to produce magneto-

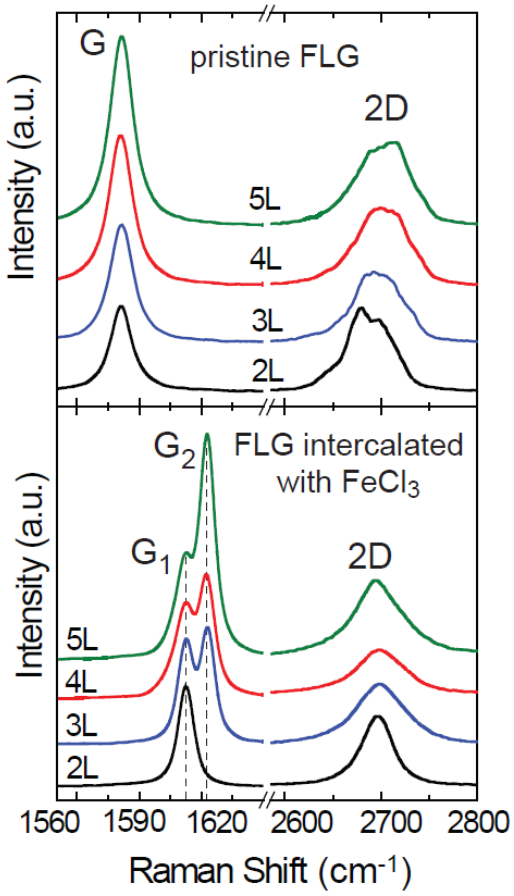

Figure 2.25: Raman Spectrum of Pristine and $FeCl_3$ Intercalated Graphene Layers. Graphene flakes with number of layers ranging from 2L to 5L were measured before and after direct intercalation with $FeCl_3$[91]. The G band upshifts and splits into G_1 and G_2 components upon intercalation. The 2D peak is seen to change shape after intercalation, resembling that of single layer graphene.

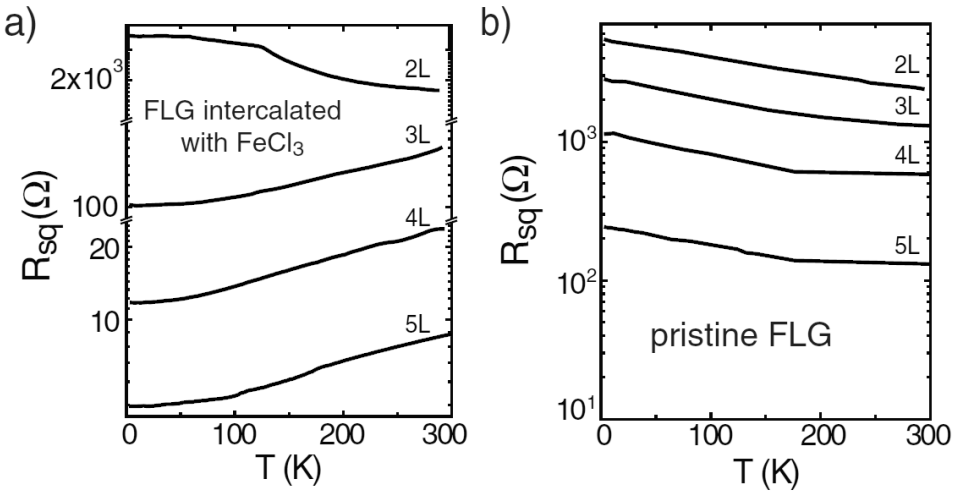

Figure 2.26: (a) The temperature dependence of the square resistance in $FeCl_3$ FLGICs[91] containing 2-5 graphene layers and (b) in pristine graphene samples for comparison.

conductivity measurements which revealed oscillations at two distinct frequencies. The temperature dependence of the oscillations gave the cyclotron masses which corresponded to the cyclotron frequency of massless Dirac fermions in graphene and of chiral massive carriers in bilayer graphene. For a 2L sample this was attributed to the inhomogeneous intercalate layer allowing regions of bilayer graphene to form[90]. For a 5L sample it was thought, based on total carrier density arguments, that the intercalate layer at the top of the stack had deintercalated creating a bilayer there[91].

2.5 Scanning Probe Microscopies

Scanning probe microscopy provides images of a surface with high spatial resolution. A surface is scanned by a probe 0.1 - 100 nm above the surface depending on the mode of operation. The probe contains a tip at the end which must be atomically sharp to achieve the best resolutions. Atomic force microscopy (AFM) is the most common mode of operation, where the tip is attached to a cantilever driven to oscillate at its resonant frequency[92]. As the tip approaches the sample surface van der Waals forces induce a change in the cantillever oscillation amplitude and frequency. Using a feedback loop, the average sample-tip height is adjusted to maintain a constant oscillation amplitude,

and hence the surface topography of a sample is measured.

To probe electrostatic forces, electrostatic force microscopy (EFM) and Kelvin probe force microscopy (KPFM) can be used. In both modes, for each scan line the topography from AFM must first be obtained and then a second (interleave) scan takes place where the tip retraces the sample topography maintaining a constant height above the surface[93]. In EFM mode a dc bias between the tip and sample is applied during the interleave scan, and the resulting phase shift of the cantilever oscillation due to long range electrostatic forces are measured[93], providing information about the charge distribution on the sample surface. In KPFM mode during the interleave scan an ac signal is applied to the tip and a dc bias applied via a feedback loop that minimises the cantilever oscillation, measuring the surface potential directly.

KPFM typically has a poor resolution when compared to EFM due to the long range nature of the Coulomb force (EFM probes force gradient)[93]. While KPFM has the advantage of providing a direct measure of surface potential, this can also be obtained with EFM by sweeping the tip voltage V_t, as explained below. By modelling the cantilever as a harmonic oscillator with spring constant k and quality factor Q, the EFM phase shift $\Delta\Phi$ is given by:[94]

$$\Delta\Phi = -\frac{Q}{2k}C''(V_{\text{tip}} - V_{\text{surface}})^2, \tag{2.20}$$

where C'' is the second derivative of the capacitance between the sample and the probe as a function of the vertical distance, V_{tip} is the dc bias applied to the tip, and V_{surface} is the electrostatic potential at the sample surface. In equation 2.20, $\Delta\Phi = 0$ when $V_{\text{tip}} = V_{\text{surface}}$, so the surface potential can be found at a given point by sweeping V_{tip} to find the value where it nulls the measured phase shift. Figure 2.27 (A) shows an example of applying this technique to find $\text{V}_{\text{surface}}$ for graphene flakes of varying thickness[95].

2.5.1 Imaging of Graphene

Scanning probe microscopy techniques have been used to image graphene based samples. AFM has been used to observe the microscopic corrugations of graphene on various substrates[96] and is generally used to identify monolayer graphene, however deviations of up to ∼1 nm from the expected graphene thickness of 0.34 nm have been

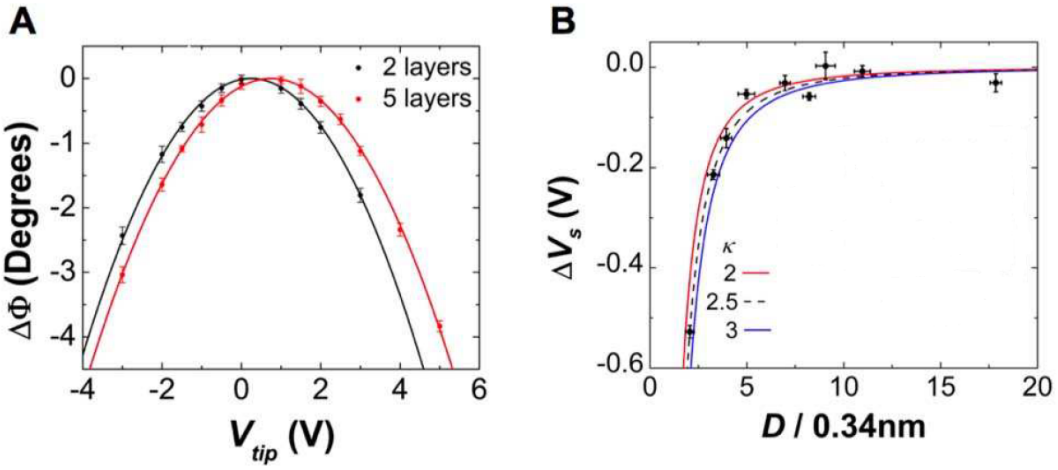

Figure 2.27: (A) V_{tip} is varied to find point where $\Delta\Phi = 0$ and hence $V_{\text{tip}} = V_{\text{surface}}$, for graphene flakes containing 2 and 5 graphene layers[95]. Solid lines are parabolic fits to the data. (B) Change in surface potential ΔV_s from that of bulk graphite ($V_s = 0.78$ V) plotted for graphene flakes (thickness D) of varying number of layers. Charges in the substrate become more effectively screened in thicker graphene flakes. Curves are fits to the nonlinear Thomas-Fermi screening model[95] with dielectric constant κ.

observed due to poor choice of measurement parameters[97] and a layer of water that can become trapped between the substrate and flake during fabrication[8].

Figures 2.28 and 2.29 show how EFM[95] and KPFM[98] have been used to image graphene flakes. Areas consisting of different numbers of graphene layers can easily be identified in the images, especially important for Epitaxial graphene where steps in the substrate make identification difficult via AFM[98, 99]. Studies have measured the surface potential and work function of graphene flakes[95, 98, 100] and shown the work function can be varied[101, 102] by moving the Fermi energy by means of applying a voltage to a back gate. EFM and KPFM studies have revealed charge inhomogeneities across graphene samples[100, 103, 104] due to water, adhesive tape residue and charged impurities trapped in the SiO_2 substrate, which scanning tunnelling microscopy (STM) measurements[103] have revealed to be 5 nm in radius and spaced 22 nm apart, and corresponding to a charge density of $n = 10^{12}$ cm^{-2}. The incomplete screening of the impurities electric field by the graphene layers[95, 100] is what makes them so distinguishable. Figure 2.27 (B) shows the surface potential measured for varying numbers of graphene layers, where it can be seen that increasing the number of layers improves the charge screening until ∼5 layers, where it approaches that of bulk graphite.

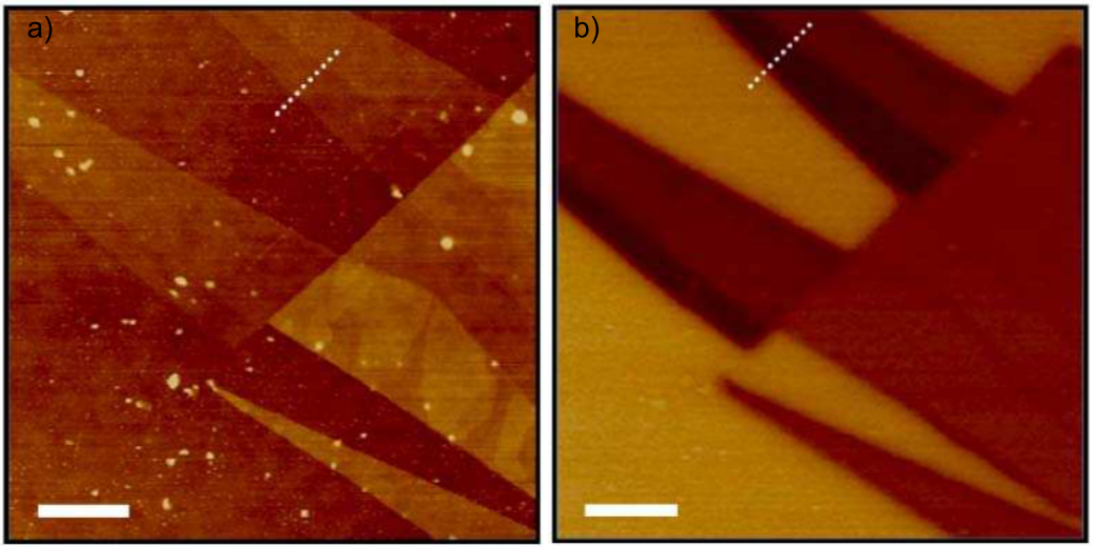

Figure 2.28: (a) AFM image[95] with colour scale of 10 nm and (b) EFM phase image with $V_{\text{tip}} = -2$ V where the colour scale represents 5.0°, for exfoliated few-layer graphene on SiO_2. The scale bar in each image is 1.5 μm. The dotted line indicates the position of a crossover from two to three graphene layers which can been seen in AFM, and also in EFM since three graphene layers screen the trapped charges in the SiO_2 layer more effectively than two graphene layers.

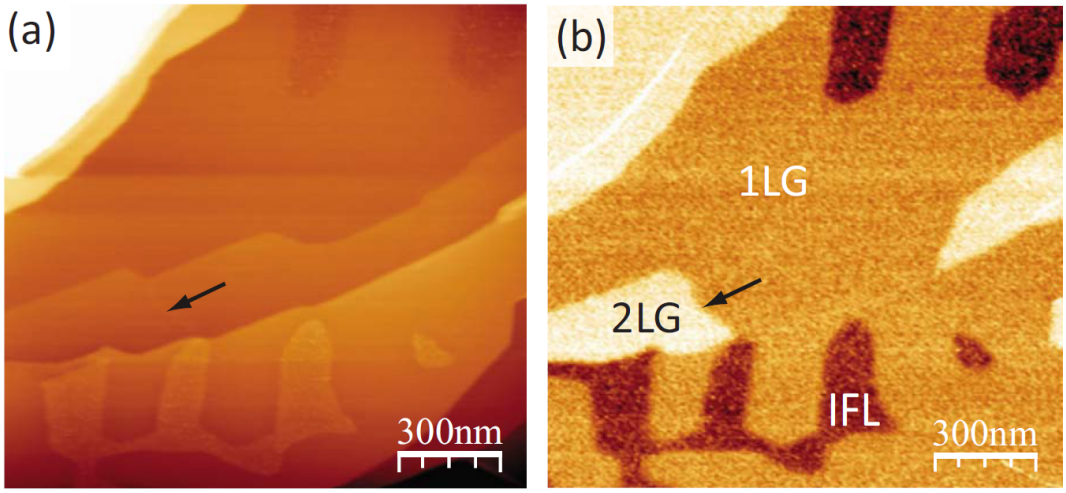

Figure 2.29: (a) AFM image of graphene film grown epitaxially on SiC(0001) and (b) corresponding KPFM image[98]. Changes in graphene film thickness are difficult to observe in the AFM image due to the step structure of the SiC substrate, but are easily visible in the KPFM image. The arrow indicates a two-layer graphene region that is barely visible in AFM but is clear in KPFM mode. The label IFL corresponds to the carbon rich interface layer unique to epitaxial graphene.

A nonlinear Thomas-Fermi model[95] has been used to study c-axis charge transfer in GICs[52, 53] and more recently the charge screening by graphene layers on a SiO_2 substrate and used to fit to experimental EFM data[95] (see Fig.2.27 (B)).

As well as imaging graphene, EFM has been used to image graphite[105]. Figure 2.30 shows the surface of HOPG measured by EFM, where variations in phase across the surface indicate regions of conducting and insulating type behaviour. Graphite is conductive with semi-metal like behaviour and so the observation of micrometer sized domains with potential differences of up to 0.25 V are unexpected. The result was found to occur only in high quality HOPG samples and not in those of lower quality (mosaicity $> 0.4°$).

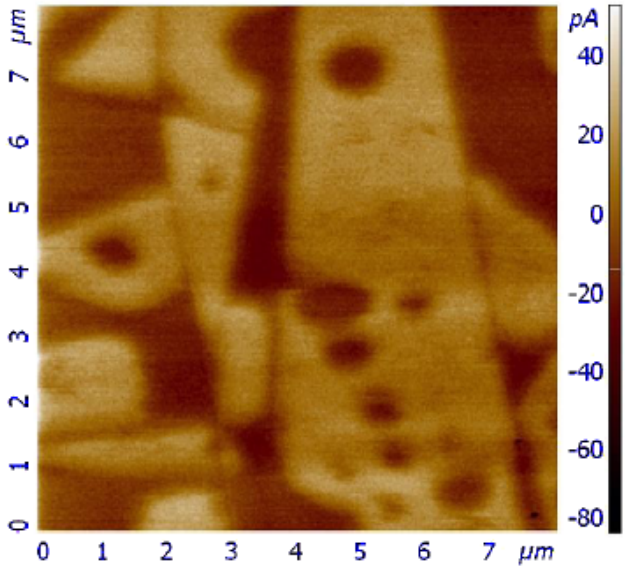

Figure 2.30: EFM image of a HOPG surface where a variation in phase can be observed, revealing regions of conducting and insulating-like behaviour[105]. Analysis reveals that the potential can vary by up to 0.25 V

Chapter 3

Fabrication and Experimental Setup

3.1 Fabrication of GICs

Synthesis of metal chloride GICs was carried out by Professor M. Suzuki at Binghampton State University of New York. Figure 3.1 shows the two-zone method that uses vapour transport to create the transition metal chloride stage-1 and stage-2 GICs. The intercalate is heated up to the chloride melting point ($\sim 500^{\circ}$C) where the metal chloride vapour can then diffuse between the graphene layers. The intercalate and graphite are separated as shown in Fig. 3.1 (b) and each heated to a different temperature, with the graphite heated to the highest temperature of the two. The temperature difference between the two determines the weight uptake of intercalate into the GIC and hence determines the stage index of the fabricated GIC (ΔT $\sim$10°C for stage-2 $CoCl_2$[49]). The ampoule containing the kish graphite and intercalate is filled with Cl_2 gas which aids the intercalation process[48]. Cl_2 pressures greater than 4 atmospheres are used to speed up the intercalation process further. Each of the different intercalates used ($CoCl_2$, $CuCl_2$, $MnCl_2$, $NiCl_2$ and $FeCl_3$) require different intercalation conditions. Additionally the size of the kish graphite used affects the total time required for intercalation, with thicker samples taking longer. The intercalate can be prepared in situ, as is the case for $FeCl_3$ in Fig. 3.1(a), which ensures it remains anhydrous and does not take on any water. It takes several days for the intercalation process to complete, after which the ampoule is cooled, all the while ensuring the metal chloride vapour

condenses on the intercalate side and not onto the newly formed GIC.

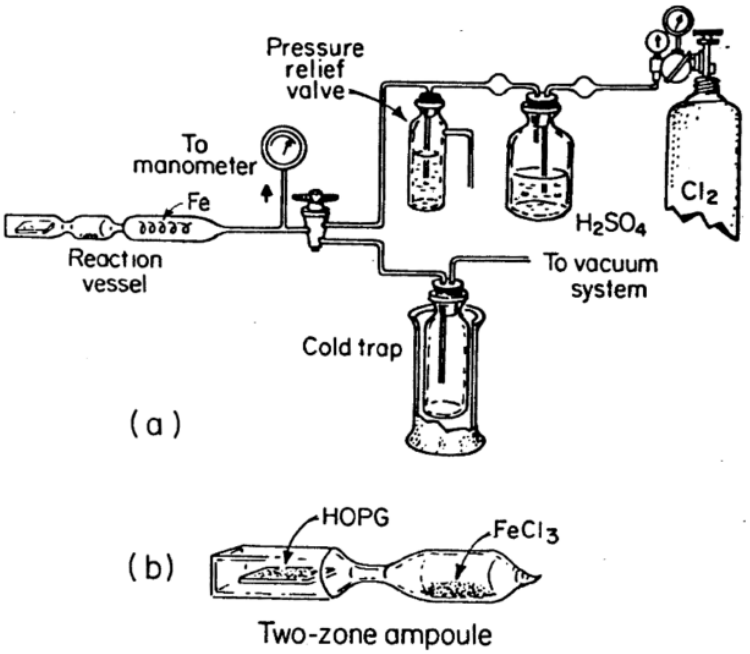

Figure 3.1: Synthesis system for a $FeCl_3$-GIC showing (a) the set-up required to prepare $FeCl_3$ in situ using a Fe wire in the ampoule and (b) the ampoule (usually glass) containing the intercalate and graphite, which are both heated to slightly different temperatures and the intercalate vapour diffuses between the graphene layers[48].

3.2 Characterisation of GICs

3.2.1 Weight Uptake

The quickest way to determine if intercalation is successful and to estimate the staging is by measuring the graphite sample after intercalation and comparing to its weight beforehand. The GICs have chemical formula of the form $C_X MCl_m$, where X can be estimated for a particular stage by taking the ratio of the in plane area of the unit cell of the MCl_m intercalate layer to that of the graphene area. Table 3.1 gives the values of X for intercalates used as well as the expected weight uptake when adding the MCl_m molecules to produce stage-1 and stage-2 GICs. These values assume intercalate coverage between the graphene layers (called the filling factor, f) is 100%. Previous weight uptake measurements have shown the actual filling factor to be f = 70-85%[49].

Weight uptake measurements provide an average filling factor and stage index for a sample and do not show if a sample consists of mixed stages. Weight uptake values of MCl_2-GICs fabricated and used in this study are given in table 4.1.

Intercalate	**Carbons per MCl_m**	**Mass of MCl_m (amu)**	**Stage-1 weight uptake (%)**	**Stage-2 weight uptake (%)**
$MnCl_2$	6.61	125.8	259	179
$FeCl_3$	6.11	162.4	321	211
$CoCl_2$	5.60	129.8	293	197
$NiCl_2$	5.65	129.6	291	196
$CuCl_2$	4.90	134.4	329	214

Table 3.1: The expected weight uptake is given for graphite intercalated to become a stage-1 or stage-2 GIC for various intercalates, assuming complete intercalate coverage between the graphene layers, $f = 100\%$. Number of carbon atoms per MCl_m were obtained from[49].

3.2.2 X-ray Diffraction

X-ray measurements are the de facto technique for characterising GICs, with the (00l) reflections yielding the c-axis repeat distance, and hence the GIC staging. Reflection X-ray measurements were attempted for the kish intercalated samples in this study but the Leybold teaching lab apparatus used was not suitable for our 1 mm thick samples, as they were too thin to reflect the required amount X-rays. As no thicker GICs were available, X-ray scattering in transmission mode was employed using Agilent-Technolgies Xcalibur molybdenum source X-ray system in the RHUL scattering group with the help of Dr Dan Porter.

A small crystallite ($1 \times 1 \times 0.035 \pm 0.005$ mm) from the GIC being studied was cut and mounted onto a 0.3 mm glass fibre using silicon gel. The small crystallite thickness was required in order for X-rays to pass through and diffract off the sample. Diffraction peaks were obtained for the whole Ewald sphere. Figure 3.2 shows a slice in the (hk0) direction for a stage-2 (estimated from weight uptake) $CoCl_2$-GIC. The distance of the peaks (converted from k-space to real-space) are matched to lattice spacings of the sample. The peaks are found to coincide with 100 and 110 for the in-plane $CoCl_2$ lattice and 100 for graphene (indexed in Fig. 3.2) confirming presence of intercalate in the sample. The carbon peaks are observed at six points giving the lattice to be symmetric

as the peak is rotated by $360°/6 = 60°$ as expected for the honeycomb lattice. The intercalate has twice as many points and has lattices oriented with the graphene layer and others that are 30° degrees out.

X-ray characterisation was not performed on all the samples since it had limited use and took a significant amount of time, the image in Fig.3.2 took about 12 hours to obtain. With regards to usefulness prior to exfoliation the technique only measured a small part of the sample that fell under the X-ray beam of 0.5 μm diameter and the piece that had been measured was not suitable for exfoliation, as it contained silicon gel that would contaminate the adhesive tape and probably add residue to the flakes exfoliated.

3.2.3 Raman Microprobe of the GIC surface

Some GICs fabricated were characterised by Raman spectroscopy, using the Raman microprobe that was used to study the exfoliated flakes. The set-up consists of a high resolution laser with a beam size of $\sim$ 500 nm diameter, which is the same order of magnitude as the wavelength of light it emits. Raman spectroscopy of GICs in the past (such as shown in Fig. 2.23) were performed with less focused lasers that probed a larger area[88]. Figure 3.3 shows the Raman spectrum obtained from the surface of a $FeCl_3$ sample estimated to be stage-1 from weight uptake measurements. The spectra was taken at two points on the surface to account for any inhomogeneity. Both spectra show the G peak at a position of $1623 \pm 1\,\mathrm{cm}^{-1}$, the same as previously reported for stage-1 $FeCl_3$[88].

A second $FeCl_3$ GIC sample with weight a uptake measurement of 219% suggesting it to be stage-1 with a filling factor of 50% or stage-2 with 100% filling factor was measured. Figure 3.4 shows the measured spectrum where the G peak region contains multiple peaks, indicating mixed staging for the section probed by the measurement (laser penetration depth is $\sim$150 layers[106]). Peaks are seen in the positions of G_0, G_1 and G_2. The region represented by the blue trace in the figure has a high intensity G_2 peak, indicating stage-1 is the largest proportion of the mixed stages and a weak G_0 peak suggesting very few undoped graphene layers. In contrast the region represented by the red trace has a significant G_0 peak indicating large portions of the area measured to contain the undoped graphene layers seen in stage-3 and above.

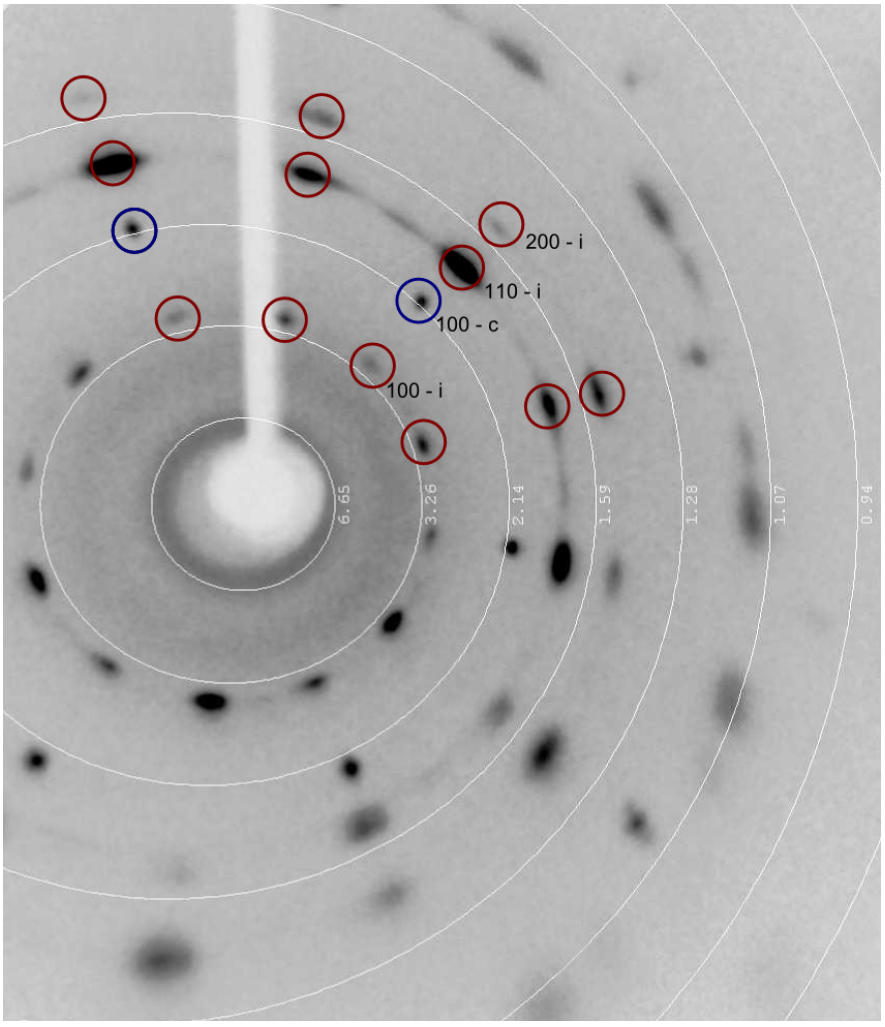

Figure 3.2: hk0 X-ray of a $CoCL_2$-GIC. Bragg peaks are indexed according to direction of reflection and if belonging to the carbon in plane lattice (c) or intercalate lattice (i). For easier identification a proportion of peaks are circled blue or red if due to the carbon or intercalate respectively. The equally spaced white contour lines give repeat distances in angstroms calculated by the software attached to the diffractometer. The carbon (100) peaks appear every 60° due the rotation symmetry of the honeycomb lattice. Additional peaks from the intercalate lattice are visible every 30° as the intercalate layers align at either 0° or 30° relative to the graphene layers.

Evidence of mixed staging in the second sample doesn't necessarily make it unsuitable for use for exfoliation as it can still produce intercalated few layer flakes. It is not desirable however as it may complicate characterisation of the flake if the staging of parent compound is uncertain. For this reason strongly mixed staged samples were avoided for the exfoliation process.

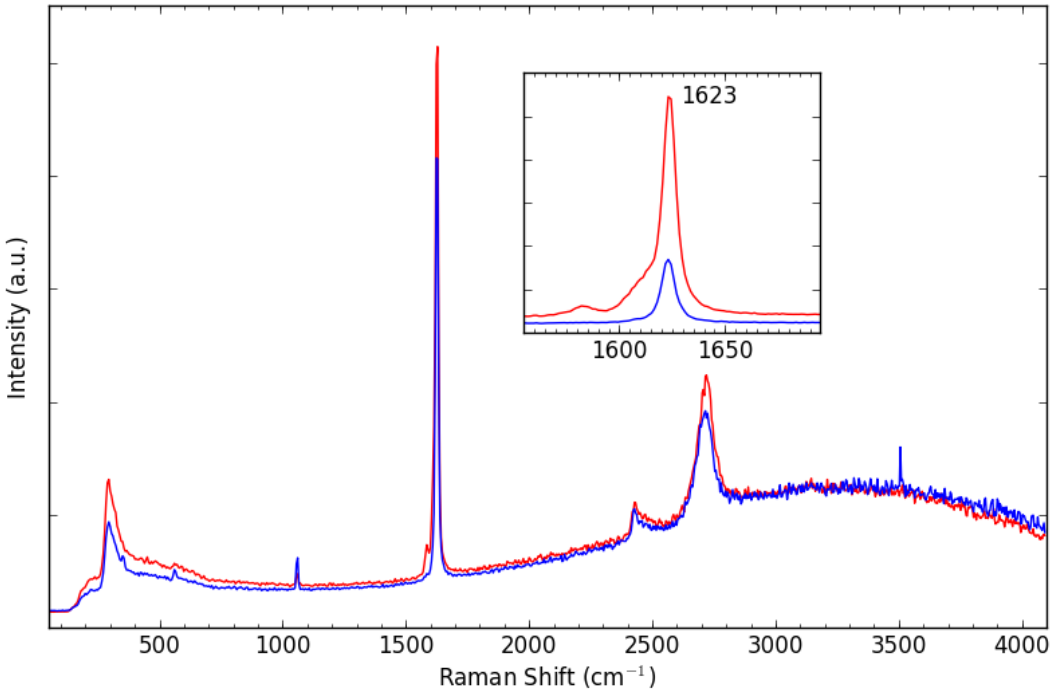

Figure 3.3: Raman spectra of a stage-1 $FeCl_3$ GIC measured at 488 nm with each trace (red and blue) taken 20 μm apart on the GIC surface. The background of the spectrum is not flat and shows luminescence from the intercalate layers. The inset shows position of G peak at 1623 cm^{-1}.

3.3 Exfoliation of GICs

3.3.1 Exfoliation Technique

Few-layer graphene intercalation compounds (FLGICs) with a varying number of intercalate layers were produced by mechanical exfoliation of bulk transition metal chloride GICs. Stage-1 or stage-2 GICs intercalated with $MnCl_2$, $CoCl_2$, $NiCl_2$, $CuCl_2$, or $FeCl_3$ were used as the starting material. The GICs were chosen primarily due to their weight

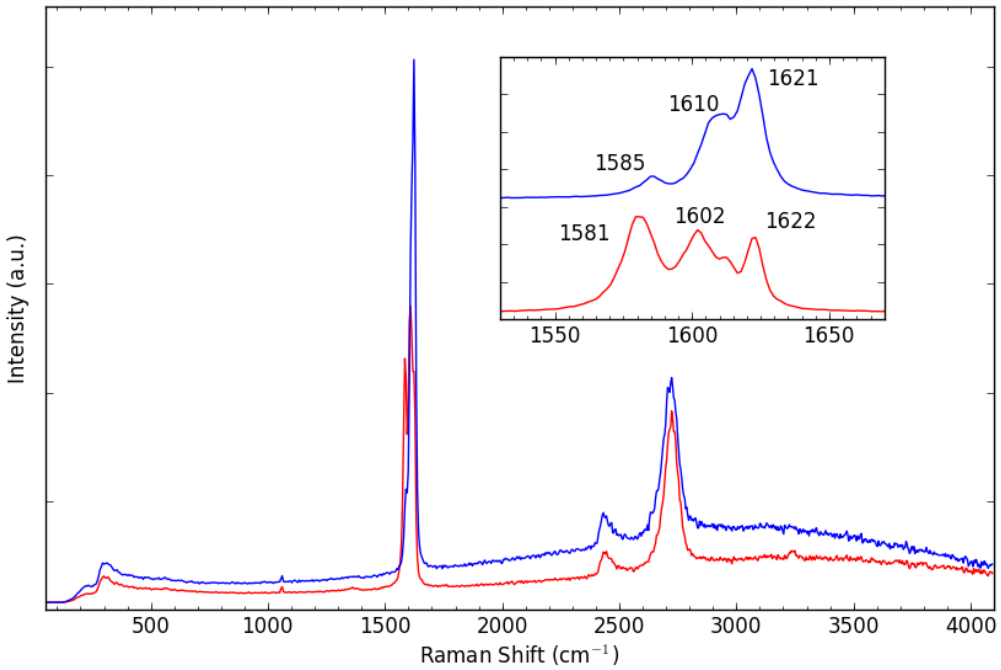

Figure 3.4: Raman spectra of a mixed stage $FeCl_3$ GIC measured at 488 nm. The GIC has a weight uptake of 219% indicating it to be stage-1 with 50% filling factor or stage-2 with 100% filling factor or a combination of both. Inset shows the G peak region consisting of three peaks of varying intensity. The presence of all three peaks (G_0, G_1 and G_2) indicate stage disorder for the area measured by the Raman probe (diameter ∼500 nm and penetration depth ∼ 50nm)

uptake since characterisation by Raman spectroscopy or X-Ray scattering only provide information on a small section of the sample and take extra time.

Figure 3.5: Optical image of a graphene flake exfoliated from Kish graphite with a measured contrast of 5% against the substrate background. The flake was confirmed to be monolayer graphene by Raman spectroscopy.

A chosen GIC was cleaved with a clean razor to expose a fresh surface for exfoliation. This was done to avoid exfoliating the outer part of the GIC that is most likely to be deintercalated due to exposure with the air. Nitto SWT 10+ adhesive tape[107] was then pressed against the GIC, using a rubber to apply localised moderate force and then peeled away. This results in exfoliating layers from the GIC. The adhesive tape was selected from a range of tapes tested and performed well due to strong adhesion while leaving little to no glue residue. Next the tape is repeatedly folded and peeled to spread the exfoliated GIC thinly across the length of tape, cut to approximately 25 cm. The tape is then pressed against the substrate and again a rubber used to apply pressure to help the flakes adhere to the substrate. Finally the tape is slowly peeled away leaving exfoliated GIC flakes on the substrate surface.

Creating a smooth surface on the substrate to which flakes are to be deposited was found to be a key requirement to produce single and few-layer flakes (<4 graphene layers). The substrate used was a 381 μm thick Si wafer with resistivity of 0.001-0.002 Ωcm, with a thermally grown 300 nm oxide layer on the surface. To prepare the wafer it was cut into manageable 1 cm^2 square chips, each of which were placed in acetone and left in a ultrasound sonicator for 10 minutes, transferred into distilled water and sonicated for a further 10 minutes, blow dried with nitrogen air gun, sonicated in

isopropanol for 10 minutes and then oxygen etched by a Oxford Instruments PlasmaLab for a final 10 minutes. The adhesive tape containing the exfoliated GIC is pressed down onto the wafer immediately after the plasma etch step, so to avoid any contamination on the surface that could hinder adhesion of flakes. The process is carried out in a clean room and exfoliated samples are stored in a dry desiccator.

Exfoliated flakes deposited onto the SiO_2 substrate were viewed under a optical microscope. To develop the fabrication method the mechanical exfoliation technique was first tested on natural graphite, HOPG and kish graphite before GICs. HOPG produced the smallest flakes ($\sim$1 μm across), while Kish and natural graphite produced flakes about an order of magnitude larger. Figures 3.5 and 3.6 show examples of flakes that were exfoliated from kish graphite, they are triangular in shape and show signs of folding or overlapping graphene layers where the contrast increases a step. Figure 3.7 shows flakes of similar thickness (about 2 graphene layers from optical contrast) exfoliated from GICs based on kish graphite. The typical shape of the flakes are less triangular and appear deformed by the intercalate layers, particularly at the edges. Although the flakes exfoliated from graphite and GICs do appear different visually this has not been used to identify intercalated flakes as the intercalate layer may have de-intercalated during the exfoliation process or cleaved at the carbon-intercalate interface, leaving the intercalate layer behind but still affecting shape of the graphene layers deposited.

To increase the average flake size to above $\sim$ 10 μm, it was found better to push the adhesive tape covered in GIC fragments along the SiO_2 substrate rather than just pressing it down. Figure 3.8 shows flakes obtained by this method. Trails of flakes can be seen along the substrate where a GIC fragment was rubbed along against the surface. Larger flakes are obtained when exfoliating GICs in this way however exfoliating non-intercalated kish graphite by pushing it along the substrate produces far fewer flakes, perhaps as GICs shear more easily since the interlayer bonding is weakened at the intercalate-carbon interfaces.

Mechanical exfoliation of stage-1 compounds always causes cleavage at a carbon-intercalate interface, whereas stage-2 compounds can cleave at either a carbon-intercalate or a carbon-carbon interface. Therefore exfoliation of stage-2 compounds is expected to produce more dilute intercalated graphene flakes, producing samples which have not been obtained by direct intercalation of few-layer graphene.

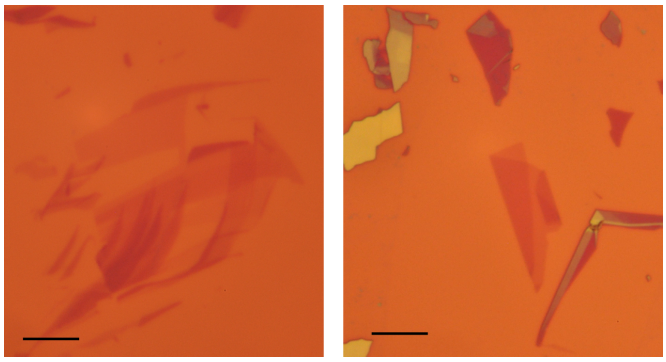

Figure 3.6: Optical images of kish exfoliated flakes which are triangular and exhibit overlapping regions and folding of the graphene layers. The scale bar is 10 μm.

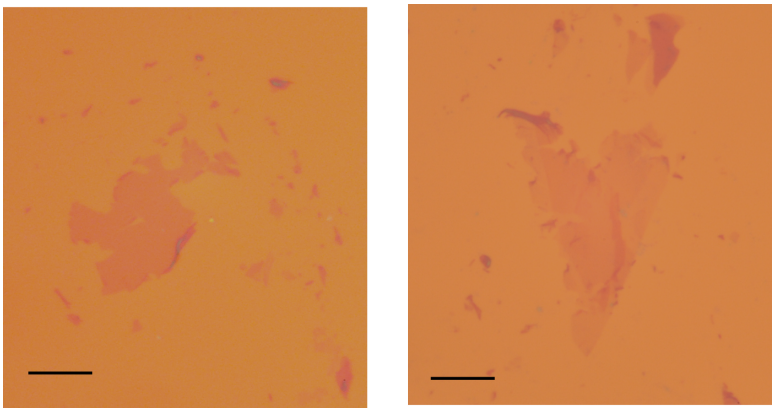

Figure 3.7: Optical images of FLGICs exfoliated from (left) a stage-2 $CoCl_2$-GIC and (right) a stage-1 $MnCl_2$-GIC, both based on kish. The structure appears deformed compared to flakes exfoliated from pristine kish graphite. The scale bar is 10 μm.

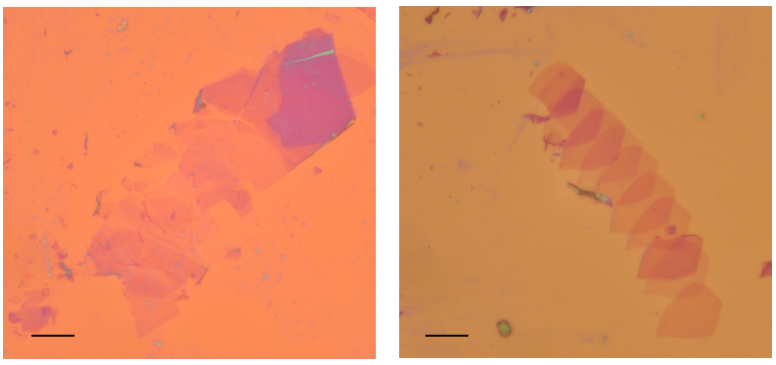

Figure 3.8: Optical images of trails of FLGICs produced by pushing a GIC fragment along the substrate. The scale bar is 10 μm.

3.3.2 Microdroplet Formation

Graphene and the silicon substrate are hydrophobic, water is repelled from the surface and tends to form droplets[108]. The transition metal chlorides investigated in this thesis are hygroscopic or deliquescent and absorb water from the atmosphere, indeed $CoCl_2$ (blue) crystals are even used as a detector of water as it changes colour when it hydrates, forming $CoCl_2.6H_2O$ (pink). Figure 3.9 shows microdroplets on samples of mechanically exfoliated GICs. In Fig. 3.9 (a) the microdroplets form a trail in the same direction that the GIC was rubbed across the wafer. It is believed that exposed intercalate layers on the adhesive tape absorbed water from the air and this was then spread onto the substrate along with the GIC crystallites. No microdroplets were ever found to form when exfoliating pure graphite and the microdroplets were found to be more likely to appear after exfoliating stage-1 than stage-2 GICs, presumably due to the higher number of expected intercalate layers.

Figure 3.9 (b) shows an optical image where droplets are mainly located on the flake and not on the substrate, suggesting that the flake contained an exposed intercalate layer that absorbed moisture from the atmosphere to form microdrolpets. Figure 3.9 (c) shows an optical image of the same flake after it was was rinsed in acetone for 5 minutes and dried with a nitrogen gas gun, resulting in the removal of the microdroplets. The microdroplets did not completely vanish from the thicker (darker in colour) region on the left hand side of the image, but became elongated and not washed away, believed to be as they are trapped underneath a top graphene layer.

To reduce droplet formation mechanical exfoliation was not performed on humid days where droplet formation was more likely, and samples that did show droplet formation were not used for further measurements.

3.4 Optical Contrast of Intercalated Flakes

3.4.1 Estimated Contrast Change due to the Intercalate Layers

Section 2.1.4.1 describes how the optical contrast of graphene on a silicon oxide layer of varying thickness was calculated. To perform similar calculations for FLGICs the method needs to be expanded to account for the extra interfaces where reflection and transmission of light can occur if each graphene and intercalate layer is modelled as a

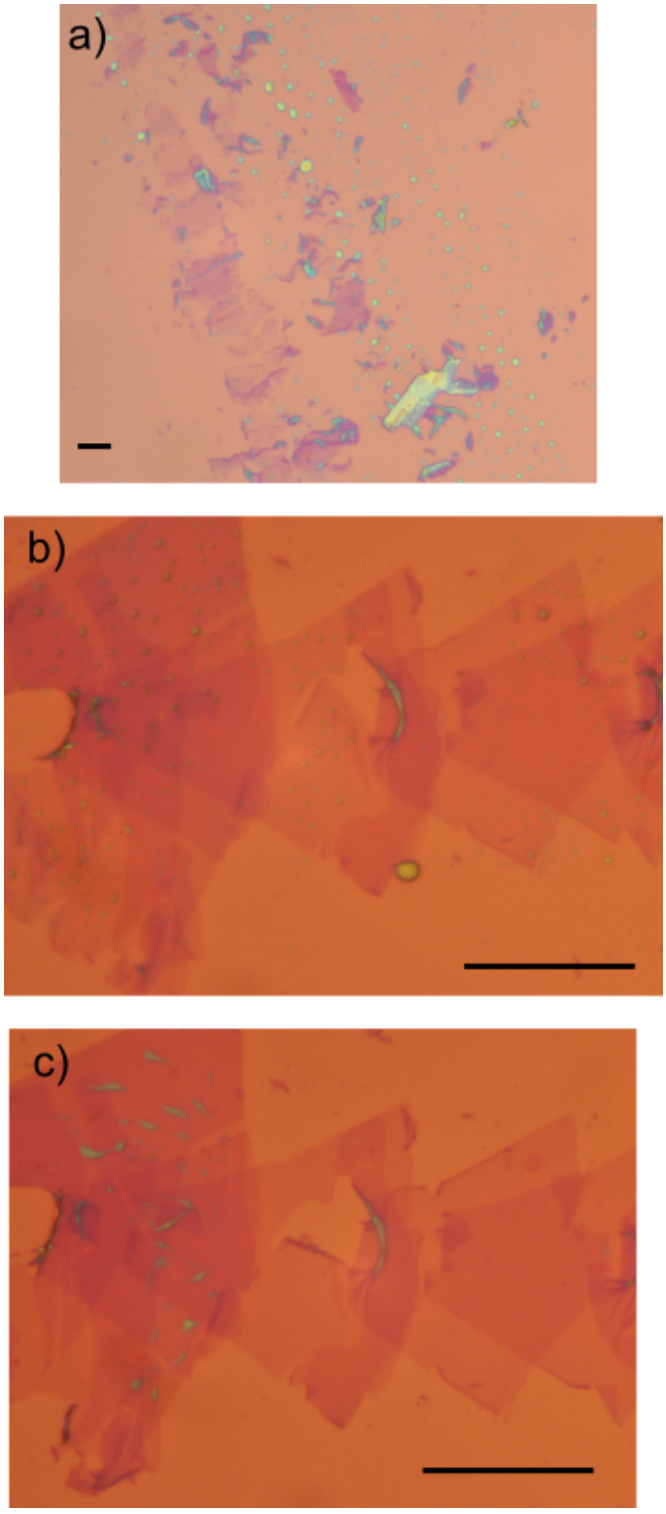

Figure 3.9: Optical images showing microdroplets produced when exfoliating GICs and depositing the flakes onto the Si/SiO_2 substrate, the scale bar is 20 μm in each image. (a) Droplets are visible on the substrate after exfoliating a stage-1 $FeCl_3$ GIC. (b) Droplets formed on a flake exfoliated from a stage-1 $MnCl_2$ GIC where (c) the droplets are seen to be mostly removed after rinsing in acetone. Droplets on the thicker region on the left became distorted indicating they are trapped by a graphene layer.

thin film. The reflectance of a monolayer graphene flake is modelled as a double layer thin film with three interfaces (Si/SiO_2/graphene/air)[39]. The thinnest FLGIC can be modelled as a 4-layer film with 5 interfaces (Si/SiO_2/graphene/intercalate/graphene/air) and the reflectance of such a film can be calculated using the recurrent matrix method for reflectance of multilayered films[109], which for light incident perpendicular to the plane is given by:

$$r = \frac{\Upsilon_0 m_{11} + \Upsilon_0 \Upsilon_s m_{12} - m_{21} - \Upsilon_s m_{22}}{\Upsilon_0 m_{11} + \Upsilon_0 \Upsilon_s m_{12} + m_{21} + \Upsilon_s m_{22}}, \tag{3.1}$$

with

$$\Upsilon_0 = \sqrt{\frac{\epsilon_0}{\mu_0}} n_0, \qquad \Upsilon_s = \sqrt{\frac{\epsilon_0}{\mu_0}} n_s,$$

where n_0 and n_s are the refractive indices of air and the Si substrate. ϵ_0 and μ_0 are the vacuum permittivity and vacuum permeability (electric and magnetic constants)and m_{ij} refers to elements of the characteristic matrix $\mathcal{M}$ constructed by multiplying matrices describing each layer in the order they appear:

$$\mathcal{M} = \mathcal{M}_I \mathcal{M}_{II} \mathcal{M}_{III} \cdots \mathcal{M}_p = \begin{bmatrix} m_{11} & m_{12} \\ m_{21} & m_{22} \end{bmatrix}, \tag{3.2}$$

where

$$\mathcal{M}_l = \begin{bmatrix} \cos\phi_l & (i \sin\phi_l)/\Upsilon_l \\ \Upsilon_l i \sin\phi_l & \cos\phi_l \end{bmatrix} \tag{3.3}$$

and

$$\phi_l = \frac{2\pi n_l d_l}{\lambda}, \qquad \Upsilon_l = \sqrt{\frac{\epsilon_0}{\mu_0}} n_l,$$

for a film with layers labelled $l = 1, 2, 3 \cdots p$, each with thickness d_l and refractive index n_l illuminated by light of wavelength λ. A value for reflectance R, a quantity that can be measured is obtained by multiplying r by its complex conjugate. The contrast is then calculated by comparing to the reflectance of the bare substrate, a film with single SiO_2 layer:

$$\text{Contrast} = \frac{R(\text{Substrate}) - R(\text{Flake})}{R(\text{Substrate})} \tag{3.4}$$

Values for the refractive index have to be obtained for each of the different layer types in the thin film. Data tables[40] were used to extrapolate values of refractive index at regular intervals in λ for the substrate. These are complex for silicon and contain the real part only for silicon dioxide. For the graphene layers the refractive

index of graphite $n_g = 2.6 - 1.3i$ was shown to fit well with experimental data[35] and is independent of λ. Data for the refractive index of the various intercalate compounds were harder to find. For the refractive index of the intercalate layer $1.9 - 0.7i$ was obtained from a study of optical properties of $CoCl_2$[110] that measured the dielectric function down to 4eV ($\lambda = 310$nm) and was used as a typical value of refractive index for all the metal chloride intercalates.

Figure 3.10 shows the calculated contrast for intercalated bilayer and trilayer flakes (intercalate between every graphene layer) compared to their non-intercalated pristine counterparts, both with a 300 nm SiO_2 layer. All traces in the plot were calculated using equation 3.1. It can be seen that the intercalate layer increases the contrast by around 8% and shifts the peak wavelength by ∼6 nm compared to a pristine sample with same number of graphene layers. The intercalated flakes therefore are visible on a Si substrate with 300 nm oxide layer, in the same way as pristine graphene flakes are. Considering how difficult it is to observe the contrast change of ∼10% due to single layer graphene (see Fig. 3.5) it is unlikely that the presence or absence of intercalate layers can be visually detected by observing the calculated difference in contrast of ∼8%.

3.4.2 Estimating the Number of Layers Experimentally

A digital camera attached to an optical microscope allowed the optical contrast of a flake to be measured from its digital image. Flakes that appeared to be only a few layers upon visual inspection were photographed using the camera. The contrast of the flake against the substrate background was estimated by analysing the digital image. Each pixel in the image contains RGB (Red-Green-Blue) values to give the colour of the pixel. The green value from an average of 10 pixels across the flake and green value from an average of 10 pixel from the nearby substrate were used as intensity values in equation 3.4 to obtain a measure of contrast. The green value was selected as this colour closest resembles the wavelength at which contrast is maximised. Figure 3.5 shows an image of a graphene flake that has a contrast of 5% when analysing the pixels in the image. This agrees with the calculation in Fig. 3.10 that shows monolayer graphene has contrast of between zero and 15% in the visible range. However the wide range means that the measurement of number of layers in a flake using this method can be determined to an accuracy of ±1 graphene layer.

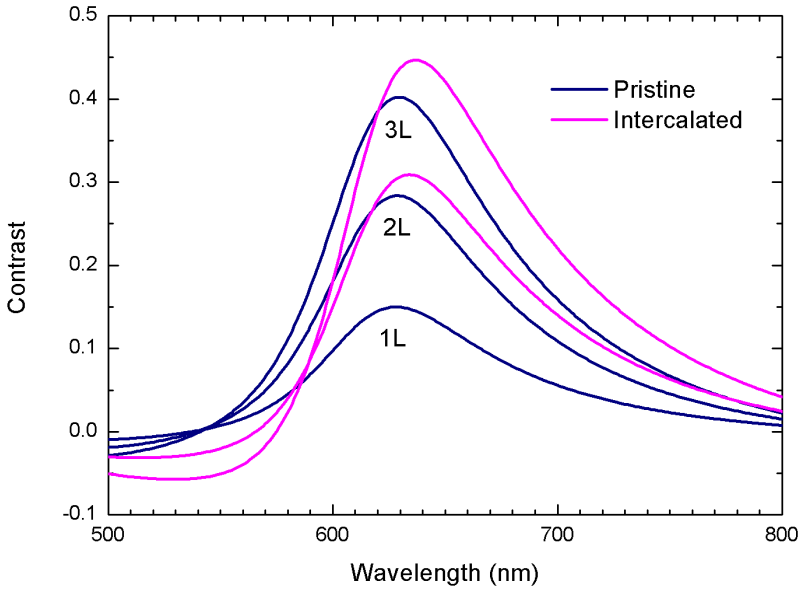

Figure 3.10: Calculated optical contrast of FLGICs and pristine non-intercalated flakes on a silicon substrate with 300 nm oxide layer. Dark blue lines for regular graphene and light blue for that of intercalated. Intercalated samples have similar contrast to non-intercalated samples with the same number of graphene layers, but with the peak in contrast ∼8% greater and positioned ∼6 nm higher in wavelength.

3.5 Fabrication of Devices

Gates and ohmic contacts need to be fabricated onto graphene flakes in order to measure their electrical properties. Gates are used to control the carrier concentration by applying a potential that depletes or attracts charge carriers to the gated region. A silicon substrate with an oxide layer allows for a back-gate to be used, as the oxide layer creates an insulating barrier between the silicon and the flake. A potential can be applied to the silicon, controlling the carrier concentration of graphene flakes. Figure 3.11 shows a schematic of the back gated device. Treating the back-gate and graphene flake as the plates of a parallel place capacitor:

$$C = \frac{\epsilon_r \epsilon_0 A}{d} = \frac{Q}{V_g} = \frac{nA}{V_g}, \tag{3.5}$$

the carrier density can then be controlled as:

$$n = \frac{\epsilon_r \epsilon_0 V_g}{d} \tag{3.6}$$

where n is charge density, C is the capacitance, ϵ_0 the permittivity of free space, ϵ_r and d are the relative permittivity and thickness of the insulating SiO_2 layer respectively. For a 300 nm oxide layer with $\epsilon_r = 3.9$ we obtain:

$$n = 7.19 \times 10^{10}\,[\mathrm{F\,C^{-1}\,cm^{-2}}] \times V_g\,[\mathrm{V}] \tag{3.7}$$

for n in units of cm^{-2}. There is an experimental limit on the gate voltage applied because the SiO_2 insulator will break down at high voltages and was kept below 25V for room temperature measurements and 100V for low temperature measurements.

For a typical semiconductor device photo lithography and e-beam lithography steps would be used to fabricate ohmic contacts in a hall bar arrangement. For FLGICs this was avoided, as lift-off involves agitation in solvents that could deintercalate the flakes. Instead, a dry fabrication technique was used, sacrificing the spatial resolution of e-beam lithography. Figure 3.12 outlines the steps of the procedure where a physical mask is used to deposit two contact pads onto an intercalated flake. A copper grid typically used for transmission electron microscopy (TEM) was used as the shadow mask, it is 0.8 mm thick with bars 10 μm wide placed every 73 μm. The grid is attached to the sample with a small amount of vacuum grease such that a bar partially

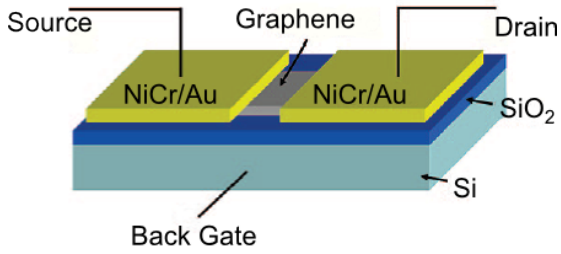

Figure 3.11: Illustration of a back gated graphene device. Graphene is deposited onto a silicon substrate with a 300 nm oxide layer. The oxide layer creates an insulating barrier allowing the silicon to be used as a back gate. Fabricated gold source-drain contacts are 50 nm thick with a 5 nm Ni/Cr sticking layer underneath. The distance between the contacts is 10 μm.

covers a flake, as shown in Fig. 3.12 (a). Using an Edwards 500 evaporator 5nm of NiCr is deposited onto the sample, followed by 50nm of gold (or silver to reduce costs). The thin NiCr layer is required as it adheres to the silicon substrate, a layer of gold by itself may not stick and could peel away. The evaporator operates by placing the sample at the top of a chamber with the chosen metal to be deposited in a crucible underneath. The chamber is evacuated to 10^{-5}Torr and the metal evaporated at a rate of 0.1 nm/s by applying a high voltage across the crucible heating the metal to melting point. After evaporation the grid is then removed to leave behind two metallic contact pads on the intercalated flake.

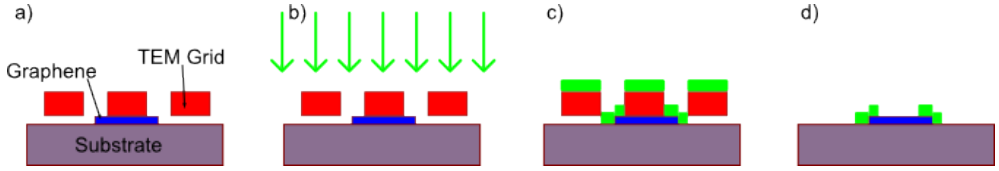

Figure 3.12: Illustration showing the steps in device fabrication. (a) A transmission electron microscopy (TEM) grid is place over a graphene flake on a SiO_2 substrate. (b) NiCr followed by Au are evaporated which then (c) deposit onto the grid, flake and substrate. (d) The grid is then removed to leave the deposited metal touching the two sides of the flake, making it suitable for a two terminal measurements.

During evaporation the two metal sources are placed on different heating elements in the chamber 6 cm apart and 30 cm from the sample. This requires the sample to be rotated 6° between the evaporation of NiCr and Au so that the shadow mask directly faces the metal to be evaporated. Failing to include the 6° rotation leads to unwanted shadow effects and a misalignment of the NiCr and Au layers. Figure 3.13 (b) shows

the resulting shadow if the 6° rotation step is not used in the fabrication process.

Figure 3.14 shows a fabricated device mounted onto a chip carrier bonded up and ready for measurement, the sample containing exfoliated flakes and deposited ohmic contacts is cut to <1 cm^2 and attached to the chip carrier using conducting silver glue. The conducting silver glue is in contact with the back of the wafer and hence can be used later to connect the back gate. A west-bond ultrasonic wedge bonder is used to connect 20 μm micron aluminium wire from the chip carrier to the ohmic contacts of the device. To avoid destruction of the graphene flakes (see Fig. 3.15) it was found that the bonder should be used without any heat applied (ultrasound pulse only).

Successfully fabricated and packaged samples were stored in conducting teflon containers to reduce possible sample damage due to static discharge. Figure 3.15 shows the image of a damaged flake that was taken before the precautionary procedures were adopted. After the first batch of devices were fabricated and measured another precautionary measure was taken. The samples were stored in a desiccator under vacuum when not being used in order to reduce exposure to the air which contains contaminants that can give unwanted doping of the samples. With this precaution the samples spent <45 minutes exposed to air during the exfoliation, attaching the TEM grid, removing the grid, mounting the sample to the chip carrier and bonding to the chip carrier (metal evaporation took place under vacuum).

3.6 Low Temperature Measurement Setup

In order to reduce the electrical noise and observe quantum effects in transport measurements, low temperatures must be used. Liquid ^{4}He boils at a temperature of 4.2 K and samples can be cooled to this temperature simply by dipping them into the inert liquid. A custom made 1 m long 'dipping' probe with a Charntek sample holder was used that allows samples in 20-way ceramic packages seen in Fig.3.14, to be inserted at one end and connected to measurement terminals via twisted pairs at the other end. The probe can be slowly lowered into a dewar of liquid ^{4}He, cooling the attached sample.

An Oxford Instruments Kelvinox dilution refrigerator was used that can cool to 30 mK and has a superconducting magnet that is capable of producing fields up to 14 T. Samples are mounted onto an insert that is loaded into the top of the fridge

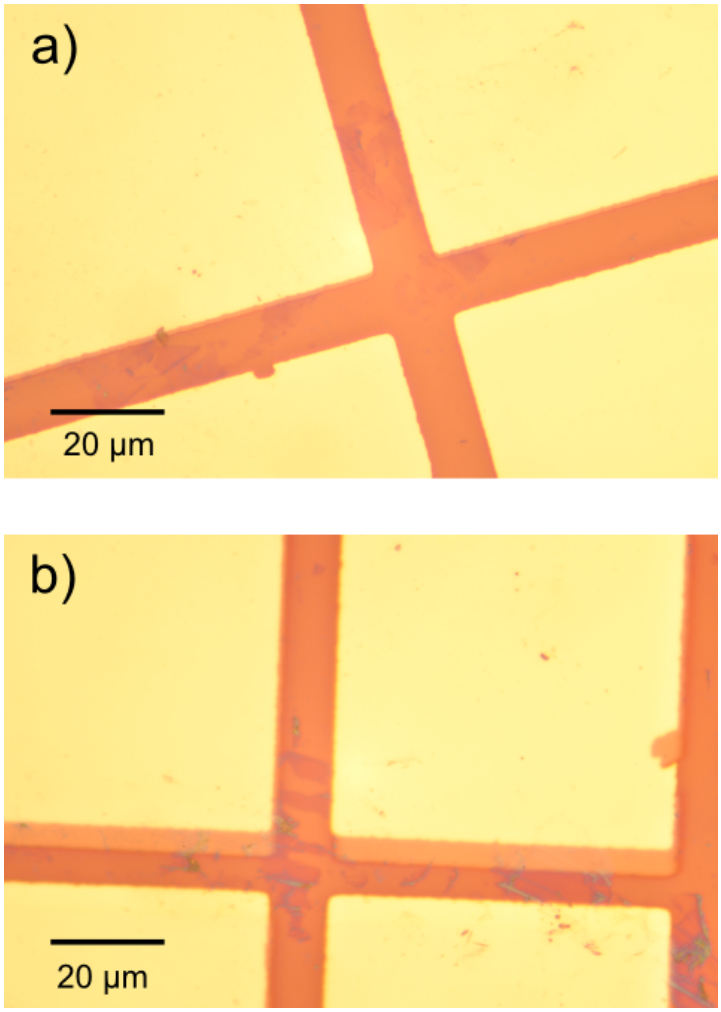

Figure 3.13: Optical image of fabricated devices showing metal pads in contact with the exfoliated flakes, fabricated by evaporating NiCr/Au around a TEM grid which is used as a shadow mask. (a) Successful deposition of metal around exfoliated flakes. (b) Deposition of metal where undesired shadow can be seen due to rotation of the sample and mask with respect to evaporation source.

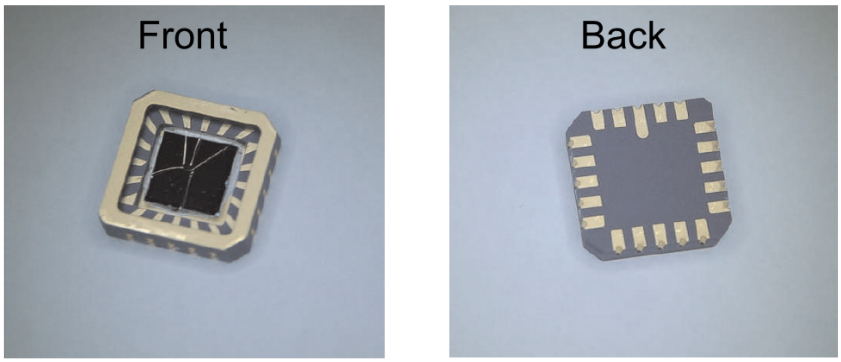

Figure 3.14: Image showing the Si wafer (300 nm oxide layer) cut and attached to a 20-way ceramic chip carrier. Ohmic contacts of the device bonded to one of the 20 gold contacts on the chip carrier using 20 μm Al wire allow measurement using the 'dipping' probe.

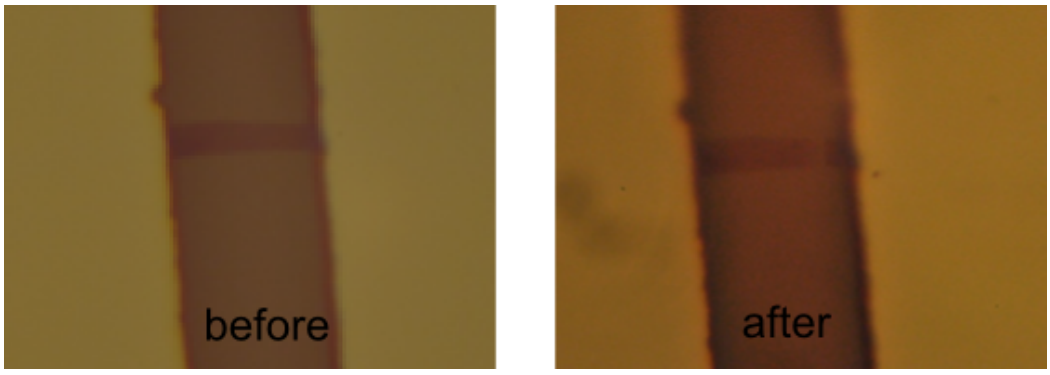

Figure 3.15: Optical image of a flake showing a tear that formed due to excessive heating when bonding.

and passes through the various cooling stages, with the coldest being located at the bottom where the samples are located. The first stage of the fridge is a helium bath used to reach 4.2 K and contains the superconducting magnet, the bath is thermally isolated from the environment by an outer vacuum can to slow evaporation; the helium bath requires refills of ^{4}He every few days. The cooling stage below 4.2 K are the 1 K pot, the still (0.3 K) and the mixing chamber and are all located in a inner vacuum can, thermally isolated from the helium bath . Temperatures of 1.4 K are reached at the 1 K pot by pumping on a few cm^3 of liquid ^{4}He, lowering its boiling point and temperatures of 0.3 K reached at the still by pumping on ^{3}He. The mixing chamber is the key component of a dilution refrigerator and contains a mixture of ^{3}He and ^{4}He. Figure 3.16 shows the phase diagram for a ^{3}He–^{4}He mixture where it can be seen below a critical temperature the mixture enters a two-phase region which consists of a ^{3}He rich phase floating on top of a heavier ^{4}He rich phase. There is a latent heat associated with evaporation of ^{3}He across this boundary, providing the cooling power of the mixing chamber.

Figure 3.17 shows the set-up used for two terminal measurements. An oscillator produces an AC voltage of 1 V with frequency of 17.3 Hz which is sent to a voltage divider and reference channel of the Perkin-Elmer lock-in amplifier. The reference channel provides the frequency of the signal to be measured on the lock-in and the voltage divider reduces the voltage to 10 μV to be applied to the sample. Typical sample resistances are 100 Ω to 10 kΩ, giving the current induced to flow through the sample by the applied voltage as 1 - 100 nA. The resulting signal from the sample is passed through a blocking capacitor to remove any DC component that may be produced by the lock-in amplifier and a pre-amplifier to increase the signal to be measured. The voltage V_g applied to the sample back-gate was using via a Kiethley 2400 voltage source with a protective 1 MΩ resistor in series. When not measuring, the leads connected to the sample are grounded as a precautionary measure.

3.6.1 Current Annealing

The quality of graphene samples can be improved by thermally heating the samples in a clean atmosphere (a process called annealing). This removes any contamination from the surface that could cause unwanted electron scattering or charge transfer, such as due to adsorbed H_2O. Annealing is unlikely to remove any contamination that is

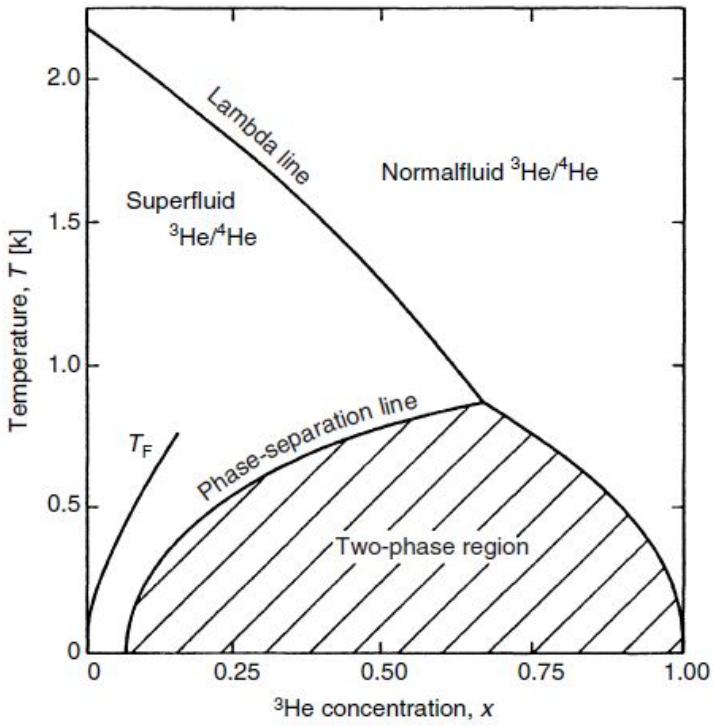

Figure 3.16: Phase diagram of liquid ^{3}He–^{4}He mixture at saturated vapour pressure[111], showing the phase separation line below which the mixture separates into a ^{4}He-rich and a ^{3}He-rich phase.

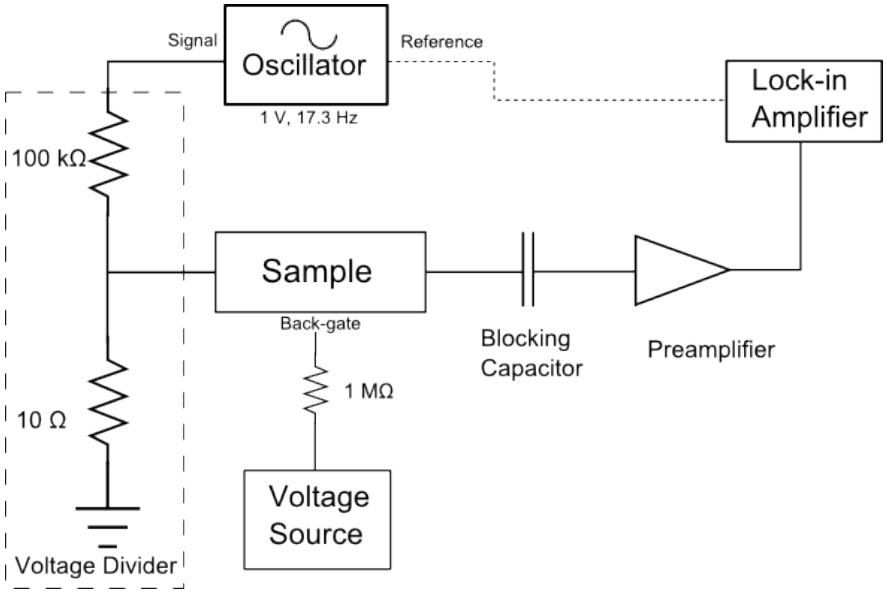

Figure 3.17: Two-terminal measurement circuit showing an AC signal applied to the sample and measured using a lock in amplifier. The voltage divider reduces the voltage applied between the source-drain contacts of the sample, the blocking capacitor removes any unwanted DC component of the signal and the preamplifier boosts the signal going to the lock-in.

trapped between the flake and the substrate, increasing the importance of using a clean substrate during fabrication.

Annealing is usually performed at several hundred degrees Celsius in a vacuum or inert gas[112, 113], however contamination can be reintroduced by exposure to the air when the sample is subsequently mounted for measurement. Current annealing[114, 115] allows the removal of contamination while the sample is inside the helium dewar or cryostat for measurement. Several volts are applied between the source-drain contacts, inducing very high current densities (10^8 A/cm^2), Joule-heating the flake. It is estimated that temperatures of ∼600 °C can be reached using this method[114].

We carried out the process in a controlled manner with voltage being slowly increased from 0 V to 2 V at 50 V/hour and held there for 10 seconds to observe any change in current. If the current stays steady the voltage is increased by 0.05 V and the current again observed. Once the current is observed to start drifting the voltage is not increased any further and is held constant until the measured current stabilises, indicating all contaminants have been removed.

Incrementing the voltage in this manner is important as applying too high a bias can

cause the carbon atoms to sublimate, usually creating a crack that propogates down the middle of the flake, between the two contacts[116]. Reported maximum current densities reached before flake breakdown are of the order 10^8 A/cm^2 per graphene layer and so care is taken not to approach this limit. Other effects of sublimation due to excessive Joule-heating are removal of graphene layers in multilayered flakes[117] and overlapping graphene flakes fusing to form single layered graphene[115]. Both would cause irreversible changes to intercalated flakes.

Chapter 4

Raman spectroscopy of FLGICs

Raman spectroscopy was carried out at Manchester University with the assistance of Axel Eckmann in the Casiraghi group using a Witec Alpha 300R spectrometer equipped with a 514 nm and 488 nm laser. Table 4.1 lists the GICs that were exfoliated to produce the few-layer graphene intercalation compounds (FLGICs), and the samples were labelled as [batch number]-[intercalate compound]-[substrate and flake identifier]. No ohmic contacts were fabricated onto the FLGICs studied in this chapter.

4.1 Raman Spectra of $CoCl_2$, $NiCl_2$, $CuCl_2$ and $MnCl_2$ FLGICs

The main purpose of measuring the Raman spectra of the exfoliated flakes is to analyse the G peak, and hence identify intercalate layers by their characteristic p-type doping of graphene. Measured G peak positions are compared to those listed in Table 2.2 to reveal if the graphene layers are flanked by intercalte on both sides (G_2), flanked on one side only (G_1) or are adjacent to no intercalate layers (G_0). Other features of the Raman spectrum such as the D and 2D peak will be presented in order to gain additional information.

The average G peak position for FLGICs exfoliated from stage-1 GICs was 1613 cm^{-1} (σ=7 cm^{-1}) and 1599 cm^{-1} (σ=8 cm^{-1}) for those exfoliated from stage-2 GICs. The greater shift measured for FLGICs exfoliated from stage-1 compounds reveals them to have higher levels of doping and is presumably due to the extra amount of intercalate layers in stage-1 GICs that carry over into the FLGICs when exfoliated.

Intercalate	Stage Index	Weight Uptake (%)
Batch 1		
$CoCl_2$	3	-
$CoCl_2$	4	-
Batch 2		
$CoCl_2$	1	227
$CoCl_2$	2	180
$CuCl_2$	1	327
$NiCl_2$	2	180
Batch 3		
$CoCl_2$	2	200
$NiCl_2$	2	191
Batch 4		
$CoCl_2$	1	316
$FeCl_3$	2	172
Batch 5		
$MoCl_5$	2	204
$MnCl_2$	1	266
$CuCl_2$	1	327
Batch 6		
$FeCl_3$	1	219
$FeCl_3$	1	294

Table 4.1: A list of the GICs exfoliated to produce samples for Raman spectroscopy measurement. The stage indices are identified from the weight uptake during intercalation.

Figure 4.1 shows the different possible stacking arrangement of layers in FLGICs, labelled in this thesis as intercalated bilayer (i2L), trilayer graphene with one intercalate layer (i3L) and trilayer graphene with two intercalate layers (ii3L). The ii3L structure can only be produced by exfoliating stage-1 GICs whereas the i2L and i3L configurations can be fabricated by exfoliating stage-1 or stage-2 compounds.

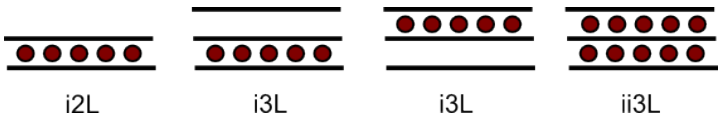

Figure 4.1: The possible stacking arrangements of layers in FLGICs produced by the exfoliation of GICs, lines represent graphene layers and solid circles the intercalate layers. An intercalate layer can only occupy one position in a 2L flake, labelled as i2L. A 3L flake may contain a single intercalate layer in either gallery (i3L) or contain intercalate in both galleries (ii3L).

Figure 4.2 presents a representative selection of Raman spectra for different FLGICs. The upshift of the G peak position from that of pristine graphene is a strong indicator of intercalation[74], and is observed for samples exfoliated from $CoCl_2$, $NiCl_2$, $CuCl_2$, $MnCl_2$ and $FeCl_3$ GICs (Raman spectra of $FeCl_3$-FLGICs are shown in section 4.2). No $MoCl_5$ FLGICs were successfully fabricated since no G peak upshift was seen in the Raman spectra of flakes exfoliated from $MoCl_5$ GICs. The failure to fabricate $MoCl_5$ FLGICs is believed to be due to the fact that the starting GIC was based on HOPG which is composed of small ~ 1 μm graphene crystallites, whereas all other GICs were based on kish graphite which contains larger crystallites.

The spectra shown in Fig. 4.2 all exhibit an upshifted G peak around 1613 cm^{-1} (G_1) and traces (iv)-(vi) show a doublet structure as previously observed in the spectra of bulk GICs[88]. The vertical structure of FLGICs (i2L, i3L or ii3L) labelled in Fig.4.2, were determined through a combination of optical contrast and identifying the G_0, G_1 and G_2 components in the G-band of the Raman spectra.

A range of peak intensities is seen for the 2D region of the Raman spectra shown in Fig.4.2, with no peak visible for traces (iii) and (iv) (which also have the highest measured G peak upshift and hence doping), revealing the Fermi energy has approached the limit $E_F > (E_L - \hbar\omega_{2D})/2$ due to Pauli blocking, described in section 2.3.2.2. For the excitation energy used $E_L = 1.96$ eV, the Fermi level has shifted a minimum of 0.82 eV from the charge neutrality point due to doping when no 2D peak is observed in the Raman spectrum, giving a lower bound to the carrier concentration $n = 4.9\times10^{13}$ cm^{-2}.

No disorder-induced D peak is observed around 1350 cm^{-1} for the samples measured, indicating the graphene layers to be free of defects and retain their in-plane structure[63, 67] after intercalation and exfoliation.

4.1.1 Raman Spectra of FLGICs with i2L Structure

Figure 4.1 shows the i2L structure of a FLGIC where two graphene layers are separated by a single intercalate layer. FLGICs with the i2L structure are identified by having a suitable optical contrast and a single G peak in the Raman spectra upshifted to $\sim$1613 cm^{-1} (G_1), since the graphene layers experience the same charge transfer as a stage-2 GIC that has a single G_1 peak in its spectra. For the $MnCl_2$, $CuCl_2$ and $CoCl_2$ samples shown in figure 4.2 the G peak positions are 1617 cm^{-1}, 1610 cm^{-1} and 1615 cm^{-1}, with optical contrasts 14%, 12% and 10% respectively. A total of 17 i2L samples were fabricated (10 $MnCl_2$, 5 $CuCl_2$ and 2 $CoCl_2$) and the G peak position was measured to be between 1608 cm^{-1} and 1618 cm^{-1} with an average of 1615 cm^{-1}. The variation in G peak position does not appear to correlate with the intercalate compound used in the FLGIC. Comparing the average G peak position to that from Raman studies of back gated graphene[76], the carrier concentration in i2L samples is estimated to be $n = 4.1 \times 10^{13}$ cm^{-2}.

No i2L samples were found to be fabricated when exfoliating stage-2 GICs, it may be that GICs prefer to cleave at the carbon-intercalate interface and not the carbon-carbon interface. There is no evidence that the intercalated bilayers have any exterior intercalate on the surface or trapped beneath the flake, since it is expected the G peak position would be upshifted further towards G_2, because of greater charge transfer from the extra intercalate.

4.1.2 Raman Spectra of FLGICs with ii3L Structure

In the ii3L configuration the inner graphene layer is doped by intercalate layers on both sides and will experience high levels of doping, comparable to a stage-1 GICs where the G peak position from the Raman spectra is $\sim$1626 cm^{-1} (G_2). The two outer layers in the ii3L configuration are flanked by intercalate on one side and are expected to produce a G_1 peak in the Raman spectra. FLGICs with the ii3L structure are identified by optical contrast and that exhibiting a doublet G_1/G_2 peak with a

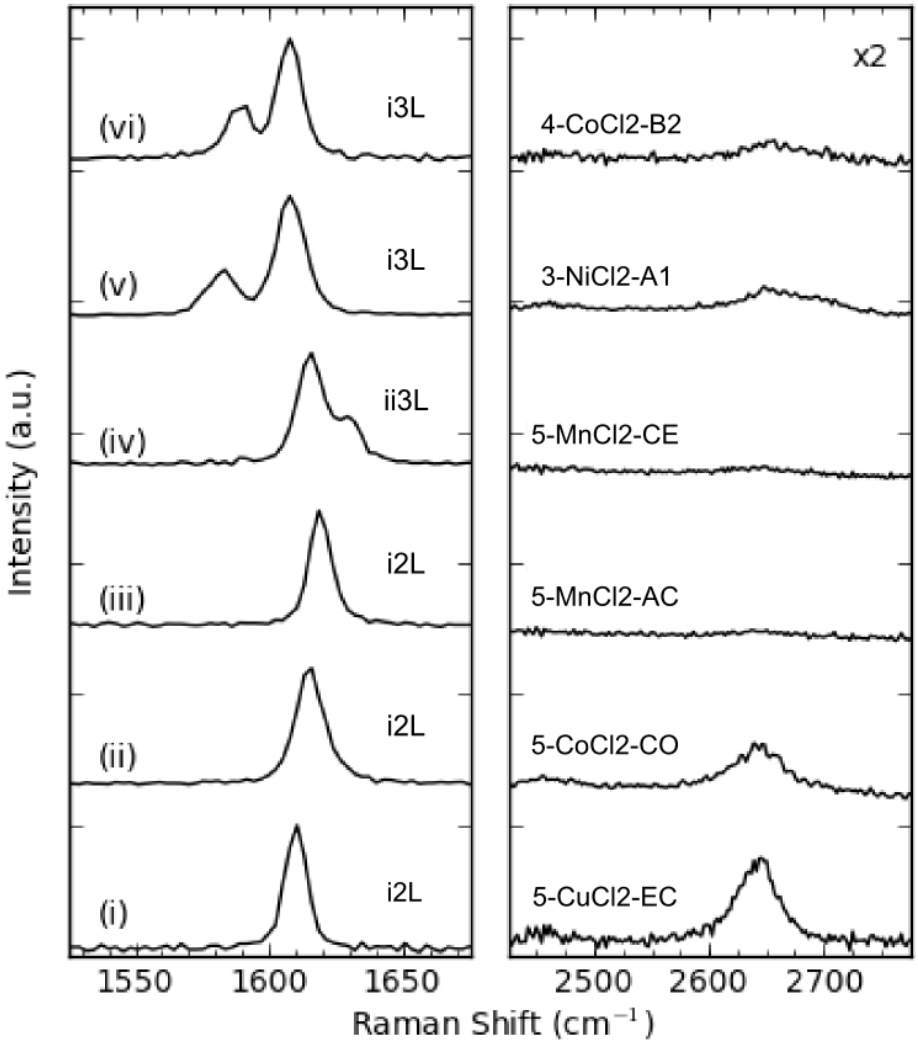

Figure 4.2: Raman studies with laser energy $E_L = 1.96$ eV (wavelength $\lambda = 633$ nm) of different MCl_2-intercalated bilayers (i2L) and trilayers (i3L and ii3L). Left panel: In the spectra of the three different i2L samples (traces (i)-(iii)) there is a single upshifted G peak. In contrast the spectrum of the ii3L flake (trace (iv)) shows additional structure at 1630 cm^{-1} (G_2), a peak that originates from the central graphene layer which is doped by two surrounding intercalate layers. The i3L samples, traces (v) and (vi), show an additional G_0 peak that comes from a graphene layer that has no adjacent MCl_2 layers. Right panel: The intensity ($\times 2$) of the 2D peaks are small relative to the G peaks. In the i2L samples (traces (i)-(iii)) the intensity of the 2D peak decreases as the G_1 peak is upshifted. The 2D peak is suppressed by Pauli blocking when $E_F > (E_L - \hbar\omega_{2D})/2$, a limit which is approached in trace (iii) and (iv). No D peak is seen around 1350 cm^{-1} (not shown) indicating the samples to be free from defects.

intensity ratio of 2:1 in the Raman spectrum, with the ratio being the number of outer graphene layers compared to inner graphene layers.

Four ii3L samples were fabricated (2 $MnCl_2$, 1$CuCl_2$ and 1 $CoCl_2$) by exfoliating stage-1 GICs. The low number of samples fabricated is an indicator that flakes often lose their intercalate layers during exfoliation, since fabricating a ii3L sample requires that no deintercalation takes place. The maximum G_2 peak position measured was 1629 cm^{-1} for sample 5-Mn-CE shown in Fig. 4.2, which gives an estimated carrier concentration for the inner graphene layer of $n = 8.3 \times 10^{13}$ cm^{-2} when comparing with Raman studies of back gated graphene[76].

4.1.3 Raman Spectra of FLGICs with i3L Structure

Exfoliated flakes with the i3L structure were identified by selecting flakes with 3L optical contrast and having a doublet in the G band of the Raman spectra at the positions of G_0 and G_1. The G_0 peak appears due to one of the graphene layers that has no adjacent intercalate layer, that can be either at the bottom or top of the stack. The G_0 peak is expected to be half as intense as G_1 since there are two doped graphene layers and one undoped graphene layer in the i3L arrangement shown in Fig.4.1. Flakes with this structure were most commonly obtained by exfoliating stage-2 GICs but are also obtained by exfoliating stage-1 GICs, where one of the intercalate layers has presumably de-intercalated.

Traces (v) and (vi) in Fig. 4.2 shows Raman spectra from FGLICs with the i3L structure. The average position of the lower wavenumber G_0 peak measured across the 16 i3L samples fabricated was 1587 cm^{-1}, an upshift of ~ 4 cm^{-1} to that of pristine graphene, indicating the graphene layer not flanked by an intercalate layer receives some charge transfer. The average G_0 and G_1 positions across the 6 i3L flakes found in batch 2 are 1587.7 cm^{-1} (σ=2.4 cm^{-1}) and 1606.2 cm^{-1} (σ=3.2 cm^{-1}) respectively. The average G_1 peak position is 7.6 cm^{-1} lower in i3L than ii3L flakes, indicating lower levels of doping. The measured position of the G_1 peak varies between 1600 cm^{-1} and 1611 cm^{-1} with an average of 1606 cm^{-1}, which gives an estimated carrier density of $n = 3.4 \times 10^{13}$ cm^{-2}, revealing the graphene layers adjacent to the intercalate layer in i3L the samples are less doped than the graphene layers in the i2L samples.

4.2 Raman Spectra of $FeCl_3$ FLGICs

FLGICs intercalated with $FeCl_3$ were fabricated by exfoliating stage-1 $FeCl_3$-GICs. Figure 4.3 shows the Raman spectrum of sample 6-$FeCl_3$-BB, taken at different parts of a flake identified to have the i3L and ii3L structure from the G peak doublet. The figure also shows spectra from a non intercalated flake located on the same sample for comparison. The Raman spectra of $FeCl_3$ FLGICs is seen to differ from that of the dichloride compounds in that an extra peak is observed at ~ 295 cm^{-1}, the intensity is seen to be more intense in the FLGIC with ii3L structure than that of i3L structure. The peak is identified as the Raman active A_{1g} mode of pure $FeCl_3$[118]. Five other Raman active modes exist in pristine $FeCl_3$[118] but are too weak or have too low a wavenumber to be detected. The $FeCl_3$ mode can be used as an additional indicator of an intercalate layer in exfoliated flakes.

The spectra in Fig. 4.3 were measured at 488 nm, a higher excitation energy than the measurements shown in Fig. 4.2. The higher excitation energy results in more intense 2D peaks as Pauli blocking does not occur (see section 2.3.2.2). The shape of the 2D peaks in Fig. 4.3 match that of those measured from monolayer graphene (see Fig. 2.20), being Lorentzian in shape and not that of multi-layered graphene flakes, where the change in electronic band structure modifies the 2D peak lineshape. The observed Lorentzian lineshape indicates the graphene layers to be decoupled in the FLGICs , due to the intercalate layers increasing their separation from 3.5 Åto 9.37 Å. Interestingly, the 2D peak lineshape seen in Fig. 4.3 is Lorentzian in shape for the FLGIC with i3L structure, that by definition contains a non-intercalated bilayer, and for the non-intercalated flake. This suggests the graphene layers are decoupled in all flakes exfoliated from stage-1 GICs. It is likely that all the graphene layers are decoupled in the starting GIC and during exfoliation deintercalation occurs, producing the non-intercalated and i3L flakes, yet the graphene layers remain decoupled electronically when the intercalate layers separating them have gone.

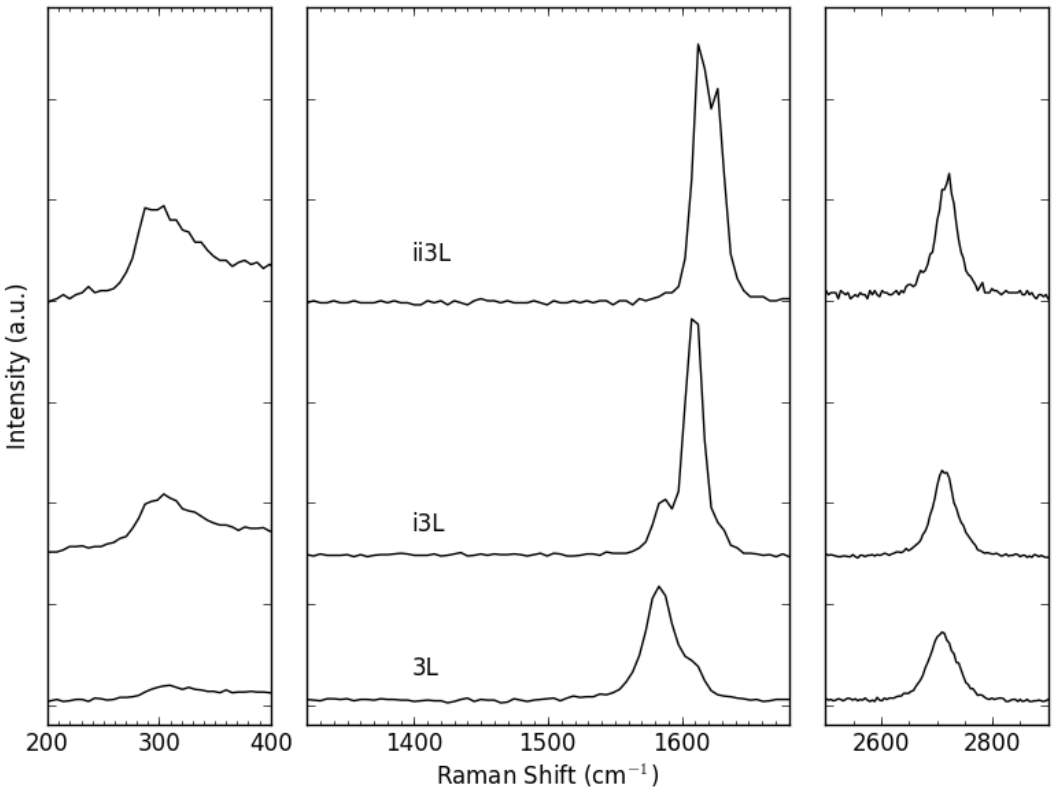

Figure 4.3: Raman spectrum of three different regions of sample 6-$FeCl_3$-BB measured at 488 nm, showing (Left) the low wavenumber $FeCl_3$ modes, (Centre) the region of D and G band and (Right) the Lorentzian 2D peaks indicating the graphene layers are decoupled, even in the non-intercalated 3L region. The ii3L, i3L and 3L designations are obtained through a combination of optical contrast measurements and analysing the G-band of the spectrum. The 3L G peak has a edge at the G_1 position indicating some residual intercalate/doping remains. All traces show no D peak at ∼1350 cm^{-}1 indicating no defects. The peak around 295 cm^{-}1 is attributed to a Raman active mode in the intercalate layer, the intensity of the peak increases with increasing number of intercalate layers and is unique to the $FeCl_3$ samples.

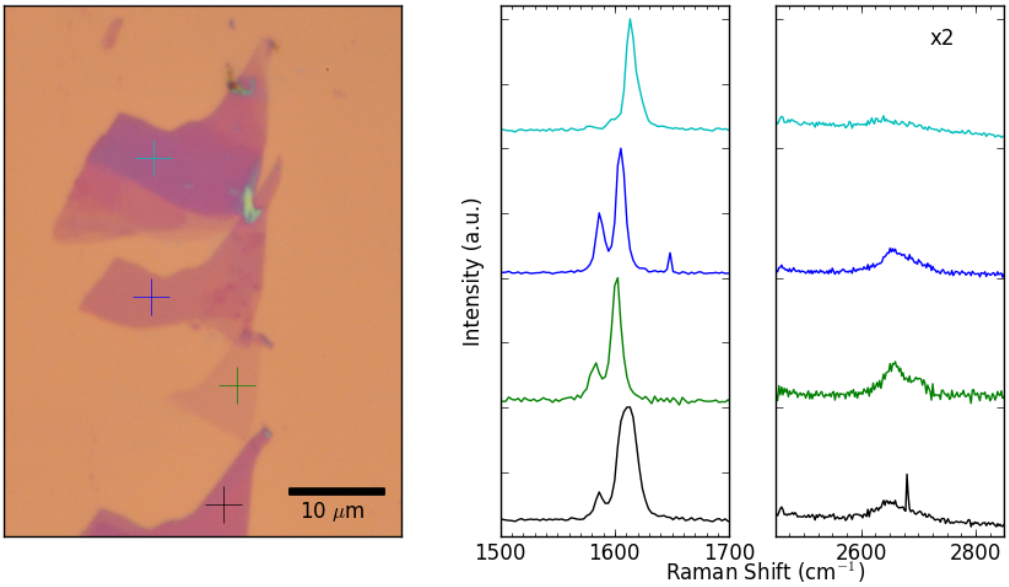

Figure 4.4: Raman spectrum of sample 3-$NiCl_2$-B21 measured at 633 nm showing FLGICS containing 4+ graphene layers. The coloured crosses in the optical image on the left indicate the position that the spectrum was taken, with the colour of the traces shown on the right matching that of the corresponding cross. The spectra have been normalised to show the same G peak intensity and the intensity of the 2D region has been increased by 2 to make the peaks visible. The flake at the top of the image with the strongest contrast, putting it a 5 ± 1 graphene layers, has a Raman spectrum that resembles the bulk stage-2 GIC it was exfoliated from. The remaining flakes in the image that have a fainter optical contrast exhibit a doublet G peak in their Raman spectrum, with the G_0 component around 1585 cm^{-1} indicating them to contain graphene layers not flanked by any intercalate layers.

4.3 Raman Spectra of FLGICs Containing 4+ Graphene Layers

For FLGICS containing ≥ 4 graphene layers the number of possible stacking arrangements of the layers increases, increasing the difficulty of identifying the structure using the G-band of the Raman spectrum and the possibility of obtaining an isolated magnetic monolayer is reduced. Raman measurements revealed FLGICs with 4+ graphene layers generally always contained intercalate layers, whereas thinner FLGICs often contained no intercalate layers, exhibiting a single G_0 peak in their Raman spectrum. Deintercalation is therefore found to be more likely for thinner FLGICs and presumably occurs every time a carbon-intercalate interface is cleaved exposing the intercalate layer to air.

In stage-1 and stage-2 GIC all the graphene layers exhibit the same level of charge transfer except for the surface layer which may experience a different level of charge transfer as the repeating stage structure is terminated. The surface layer is insignificant in GICs and does not contribute to the Raman spectrum, for FLGICs the case is different, the intensity of photons from Raman scattering in the surface layer is comparable to that of the other layers. When considering increasingly thicker FLGICs there should be a point where the Raman spectrum becomes indistinguishable from that of bulk GICs, as the ratio of inner graphene layers to surface layers increases.

Figure 4.4 shows Raman spectra of FLGICs exfoliated from a stage-2 GIC. The thickest FLGIC seen in the figure contains 5 ± 1 graphene layers from its optical contrast and has a single G_1 peak in its Raman spectrum, the same as that for a bulk stage-2 GIC, indicating the FLGIC has reached the bulk limit. The other thinner flakes shown in Fig. 4.4, that have fainter contrast (the flake indicated by the green cross is 2 ± 1 graphene layers from optical contrast measurement), have an additional G_0 peak in their Raman spectrum, explained by an undoped graphene layer at the surface such as is the case for the i3L structure shown in Fig. 4.1.

4.4 Raman Maps

Measurements of Raman spectrum at several points across flakes have revealed the spectra to be non-uniform across the FLGICs. Changes in G peak position and 2D

peak intensity have been observed, arising due to variation in the electronic and structural properties across each FLGIC. To visualise the variations in the spectra, images have been created that map the Raman features spatially across a flake. The Raman spectrum has been taken every 0.25 μm (with laser spot size $\sim$ 0.5 μm) for samples 3-$CoCl_2$-B3, 5-$CuCl_2$-EC, 5-$MnCl_2$-CD and 6-$FeCl_3$-BB. Using the Witec software, Raman maps were created that map peak position, intensity or FWHM on a colour scale, in effect creating a false image of the flake. The G and 2D peaks were used to create the maps since they are the characteristic peaks in the Raman spectrum of graphene based samples.

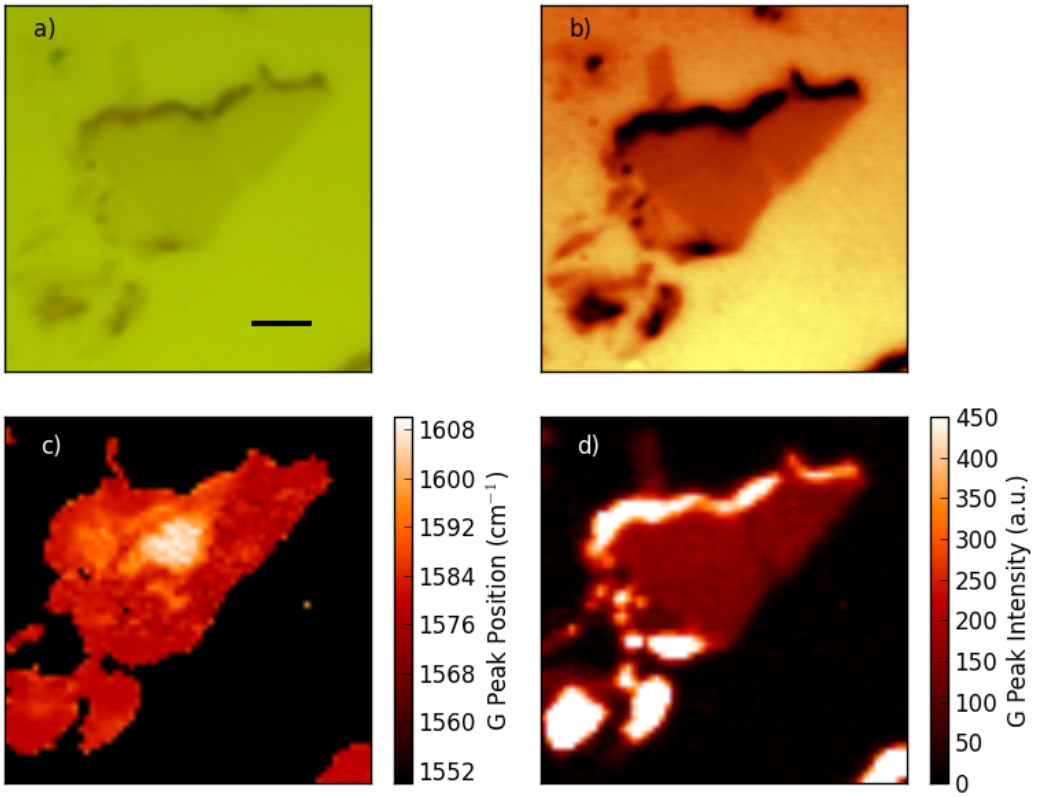

Figure 4.5: Sample 5-$CuCl_2$-EC imaged by a) optical microscope under green light, b) the same image edited to enhance the contrast, c) Raman map of G peak position and d) Raman map of G peak intensity. The scale bar in a) is 2 μm. The Raman map of G peak position shows the centre of the flake to have a region with an upshifted G peak, and hence an intercalate layer. The flake contains two graphene layers as measured by optical contrast and the top of the flake appears to have crumpled, presumably due to agitation from mechanical exfoliation. The G peak intensity is constant across the bilayer part of the flake and is more intense where the graphene layers have crumpled.

Since the G peak measured in FLGICs is often a doublet with two peak components at positions x_1 and x_2 in wavenumber and with peak intensities I_1 and I_2, the center of mass definition is used to obtain a single value of G peak position x_{avg} for the maps and is given by:

$$x_{\text{avg}} = \frac{I_1 x_1 + I_2 x_2}{I_1 + I_2}. \tag{4.1}$$

The position, intensity and FWHM of 2D peaks are obtained for Raman maps by fitting a Lorentzian curve to the Raman spectrum in the 2D region.

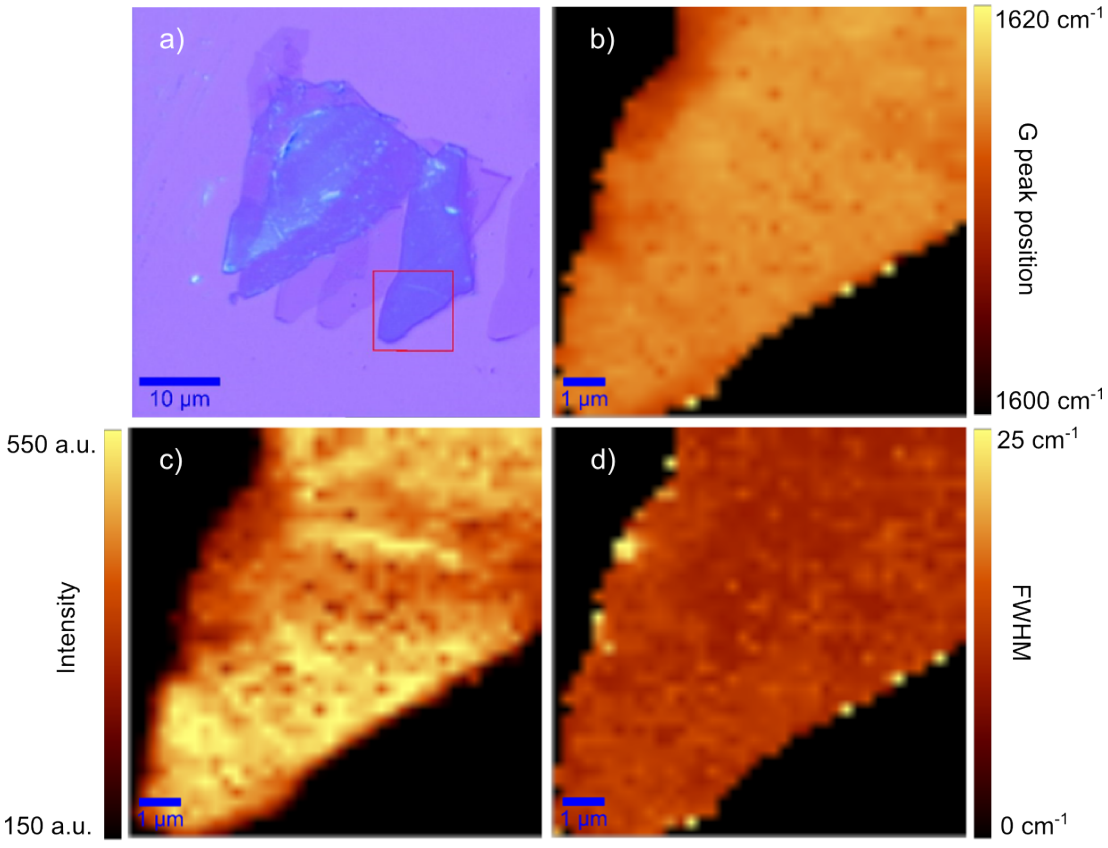

Figure 4.6: Optical image in a) shows area used for Raman maps of G peak position b), intensity c) and FWHM d) of sample 3-$CoCl_2$-B3. The strong optical contrast of the flake flake reveals it to contain tens of graphene layers. The G peak is upshifted to G_1 as expected for a stage-2 compound. The G peak shows no variation indicating the intercalate layers not to form domains in such thick flakes.

4.4.1 Intercalated Domains

The most striking feature of Raman maps of FLGIC samples is that the G peak upshift, used to indicate doping and hence an intercalate layer, is not uniform across the flake. Figures 4.5, 4.8 and 4.10 show Raman maps of G peak position, revealing areas of G peak upshift several microns across, attributed to the formation of intercalated domains up to several microns across. Figure 4.6 shows a Raman map of an intercalated flake exfoliated from a stage-2 GIC that contains tens of graphene layers, enough layers to be approximated as a bulk GIC. The map shows the G peak at the G_1 position, as expected for a stage-2 GIC, not to vary across the flake, such that the intercalate layers do not form domains in this sample, unlike what was expected by the Daumas-Hérold domain model[57]. It may be Daumas-Hérold domains exist at a length scale below Raman spectroscopy mapping resolution. The domains seen in the FLGIC samples are most likely created due to deintercalation during exfoliation, a hypothesis supported by the evidence that the graphene layers are decoupled everywhere in FLGICs, even in non-intercalated regions because of deintercalation, as discussed above.

Figures 4.7 and 4.9 show Raman maps of the D peak intensity, where the absence of the D peak is used as an indicator of graphene samples being free from defects. It can be seen that the domain interfaces, of intercalated to non-intercalated regions, surprisingly show no D peak, even though the graphene layer presumably has to deform at the boundary when intercalate increase the layer separation. The maps do reveal the D peak to be present at the edges of the flakes, as expected for a graphene edge[63].

4.4.2 Other Observations from Raman Maps

Figures 4.7 and 4.9 show Raman maps of the 2D peak taken at 633 nm revealing additional information about the FLGICs in samples 5-$CuCl_2$-EC and 5-$MnCl_2$-CD. The 2D peak has been shown to have a Lorentzian lineshape throughout the FLGICs (see Fig.4.3) but the Raman maps reveal the 2D peak to be less intense and narrower in the intercalated domains. The intercalate layer absorbs a portion of photons and reduces the probability of a 2D Raman scattering event being detected, decreasing the area under the corresponding 2D peak. The position of the 2D peak is seen to remain unchanged from the intercalated domains to the adjacent non-intercalated bilayer in Figs. 4.7 and 4.9. Raman maps of the 2D peak intensity, FWHM and position in Figs.

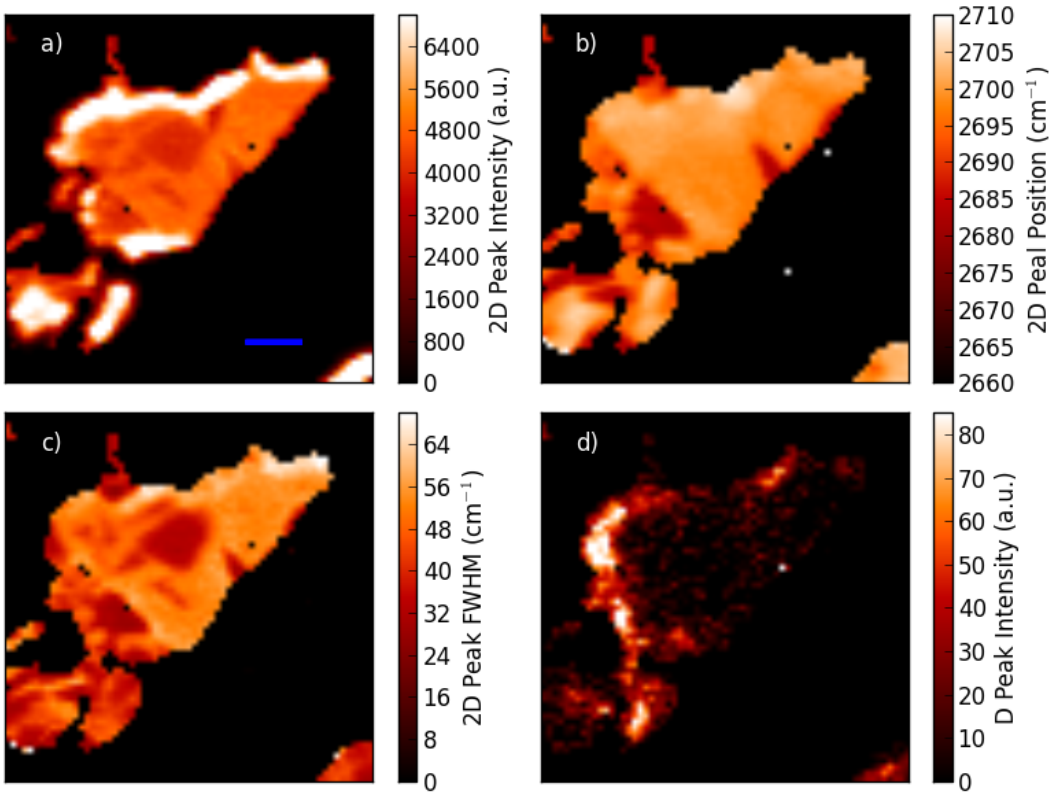

Figure 4.7: Raman maps of a) 2D peak intensity, b) 2D peak position, c) 2D peak FWHM and d) D peak intensity of sample 5-$CuCl_2$-EC. Scale bar in a) is 2 μm. The map of 2D peak position reveals two regions that are seen to be monolayer from optical contrast. The maps of 2D peak intensity and FWHM reveal the monolayer regions as well as intercalated regions seen in Raman maps of G peak position. The Raman map of the D peak intensity reveals the FLGIC to be free from defects, except at the edges as expected.

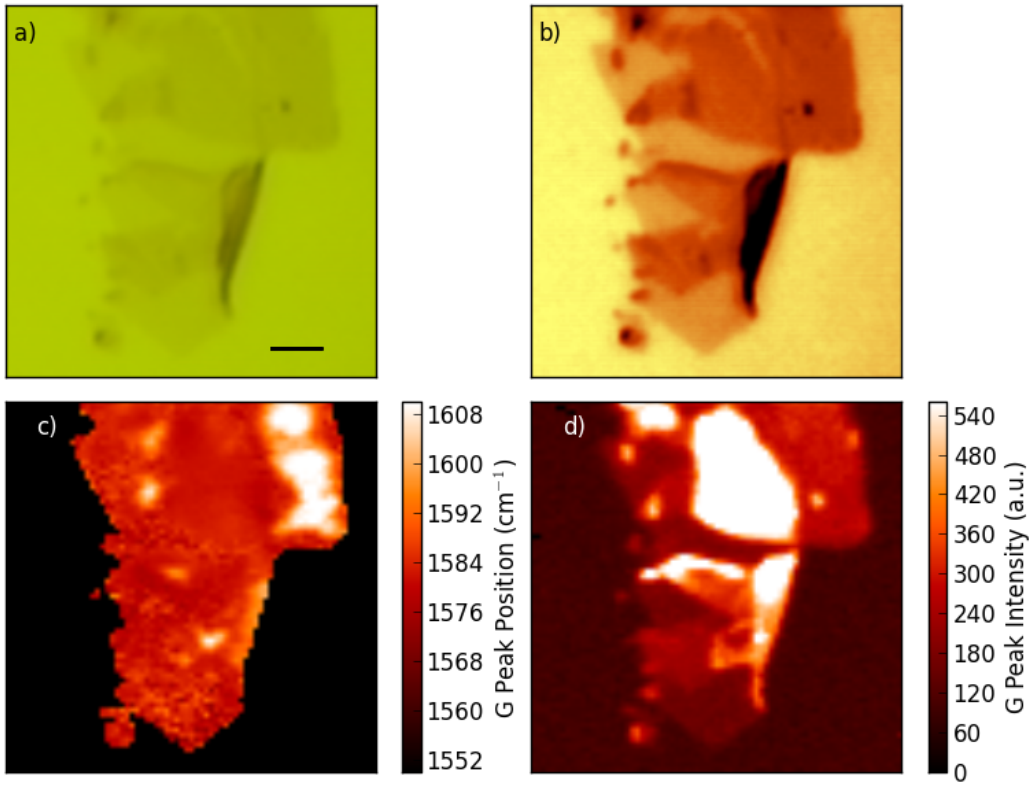

Figure 4.8: Sample 5-$MnCl_2$-CD imaged by a) optical microscope under green light, b) the same image edited to enhance the contrast, c) Raman map of G peak position and d) Raman map of G peak intensity. The scale bar in a) is 2 μm. Regions of monolayer and bilayer graphene are identified from the optical images. Intercalated domains can be seen in the map of G peak position, with the largest domain towards the top-right of the image. The Raman maps of G peak intensity reveals one of the bilayer regions to have a higher G peak intensity, indicating the two graphene layers to have become misoriented. A higher contrast region can be seen at the bottom-right of the optical image where the graphene layers appear to have folded over many times, presumably due to agitation from mechanical exfoliation.

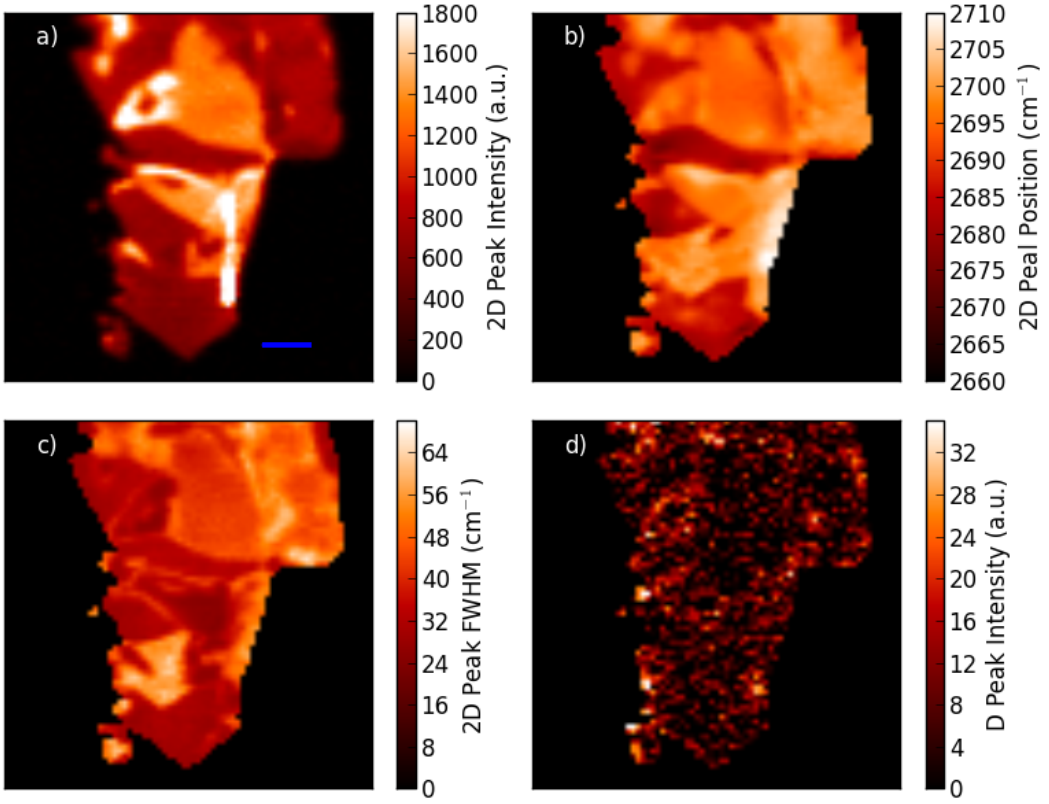

Figure 4.9: Raman maps of a) 2D peak intensity, b) 2D peak position, c) 2D peak FWHM and d) D peak intensity of sample 5-$MnCl_2$-CD. Scale bar in a) is 2 μm. The Raman map of 2D peak position shows a contrast between the monolayer and bilayer regions of the flake. Features corresponding to the intercalated domains and change in monolayer to bilayer regions can be seen in the maps of 2D peak intensity and FWHM. The graphene layers in the bilayer parts of the flake have rotated and become misoriented resulting in changes to the 2D peak intensity, FWHM and position.

4.7 and 4.9 each illustrate the location of monolayer regions as previously identified from optical contrast images. The 2D peak of monolayer graphene can therefore be distinguished from that of stacked but decoupled graphene layers in FLGICs.

The Raman maps of sample 5-$MnCl_2$-CD show evidence of the non-intercalated bilayer regions to have twisted graphene layers, exhibiting the characteristic Raman spectrum for misoriented graphene[81] (see Fig. 2.22). The Raman map of G peak intensity in Fig. 4.8 shows a bilayer region that has a significantly more intense G peak, indicating one of the graphene layers to be rotated by $\sim 10°$. The Raman map of 2D peak intensity in Fig. 4.9 shows a different non-intercalated bilayer region that has an intense 2D peak compared to the rest of the flake and is identified as having a graphene layer rotated by $\sim 25°$. These graphene layers have presumably been twisted when pushing the GIC across the substrate or during the violent exfoliation process. The bilayer region layer rotation of $\sim 25°$ is seen to contain an intercalated domain (i2L) and interestingly the intercalate layer does not show any evidence of being affected by the rotation of the host graphene layers. The $MnCl_2$ intercalate is incommensurate with the graphite lattice[49] and explains why the intercalate layer can remain when the graphene layers have been rotated.

Figure 4.10 (a) shows a Raman map of G peak position of sample 6-$FeCl_3$-BB and Fig. 4.10 (c) shows a map of the low wavenumber $FeCl_3$ mode intensity for the same sample. The maps demonstrate how both the G peak position and $FeCl_3$ mode of the Raman spectrum can be used to determine the presence of intercalate layers in $FeCl_3$ FLGICs. Areas of the FLGIC with ii3L and i3L structure can be identified from the Raman maps shown in Fig. 4.10 and agree with the the individual spectrum from each region as shown in Fig. 4.3.

4.5 Stability of FLGICs

Figures 4.10 and 4.11 show Raman maps of G peak position for samples 6-$FeCl_3$-BB and 5-$MnCl_2$-CD that were taken several times over a period of up to 8 months, and are used to study how the intercalated domains change over time. The samples were stored in a desiccator between measurements to avoid exposure to moisture in the air.

Sample 6-$FeCl_3$-BB shown in Fig. 4.10 was mapped straight after exfoliation (<90 mins) and then again ~ 24 hours later. Changes in the G peak reveals that deinterca-

lation has occurred between the two measurements because the intercalated domains appear smaller in the measurement taken on day 2. Sample 5-$MnCl_2$ shown in in Fig. 4.11 was mapped several days after exfoliation and then 8 months later, the intercalated domains are seen not to have deintercalated over this time, with the largest domain remaining the same size. The results from this section suggest $FeCl_3$ FLGICs to be less stable than those intercalated with $MnCl_2$, however the first Raman map of sample 6-$FeCl_3$-BB was taken immediately after fabrication while the first map of sample 5-$MnCl_2$-CD was taken a few days after fabrication. It may be that deintercalation occurs over the first few hours after exfoliation and the intercalated domains in FLGICs become stable for many months.

4.6 Measurements at Different Excitation Energies

Raman measurements in this chapter have been performed with light of wavelength 488 nm and 633 nm due to a change in experimental set-up over the course of study. The effect of changing the laser is examined by presenting Raman measurements of the same sample measured by both lasers. Figure 4.12 shows the Raman spectrum at the same point of sample 5-$MnCl_2$-CD measured at 488 nm (2.54 eV) and 633 nm (1.96 eV). The G peak is seen to remain largely unchanged when measured at different excitation energies, whereas the 2D peak appears at $\sim$ 2643 cm^{-1} for the 633 nm measurement and at $\sim$2719 cm^{-1} for the 488 nm measurement, and with significantly different intensities. The 2D peak position is dispersive with excitation energy[63] (see section 2.3.2), explaining the observed difference in the position of the 2D peak.

For doped graphene samples the 2D peak can be suppressed when Pauli blocking (see section 2.3.2) occurs such that the 2D peak process cannot take place at the given excitation energy, however this is not the case for the 644 nm measurement in Fig. 4.12 as a faint 2D peak can be observed. The lower intensity of the 2D peak of the can be explained using equation 2.19, which describes how the intensity of the 2D peak compared the G peak varies with electron scattering rates in doped samples, and that electron scattering rates depend on electron energy[77] ϵ which is given by the excitation energy E_L used to excite the electron-hole pair $\epsilon = E_L/2$.

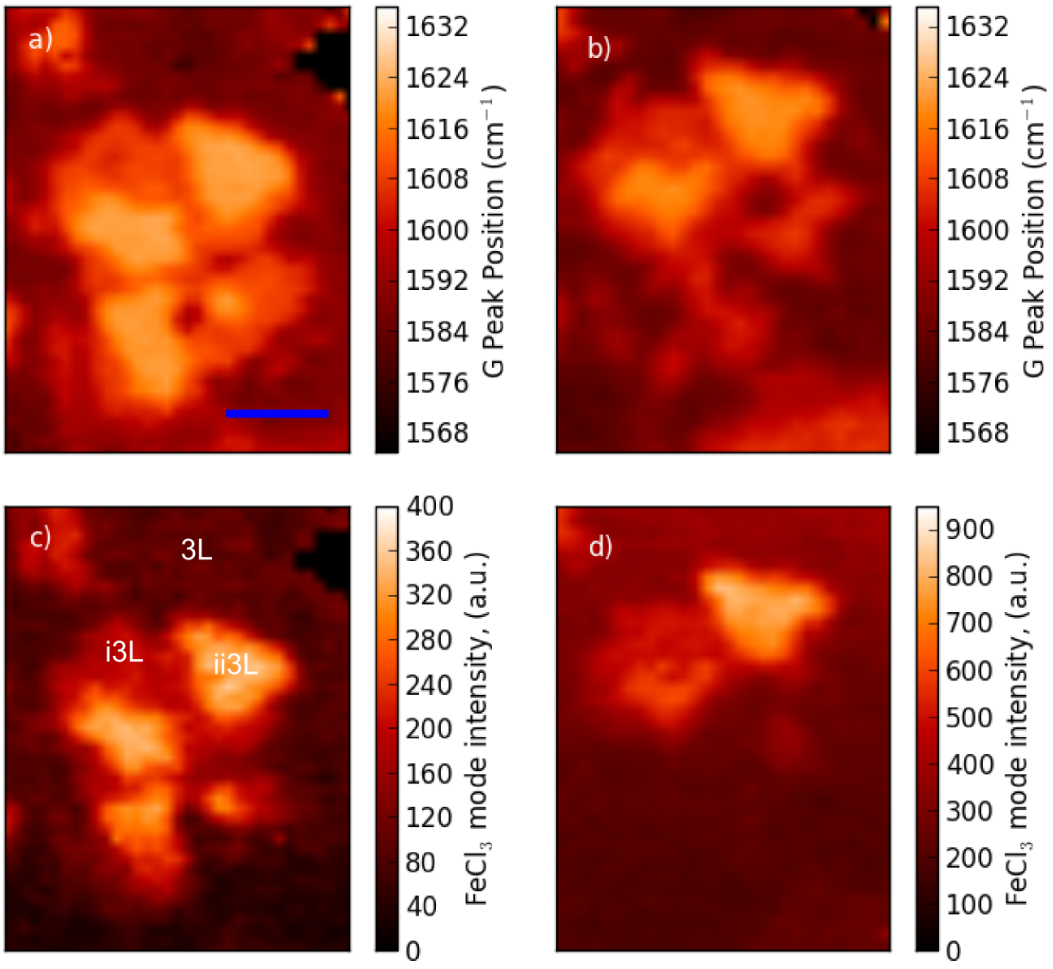

Figure 4.10: a) Raman map of G peak position measured on the day of exfoliation and b) the same flake measured the following day for sample 6-$FeCl_3$-BB. Raman maps of the low wavenumber $FeCl_3$ mode intensity are taken of the same sample c) on the day of exfoliation and d) the next day. The scale bar is 2 μm and the labels ii3L, i3L and 3L indicate the structure of the given region (spectra from each region are shown in Fig. 4.3). Maps of the $FeCl_3$ modes identify the same intercalated domain structure as seen in maps of G peak position. The flake appears to have deintercalated, losing some of the intercalated domains towards bottom right of image from day 1 to day 2.

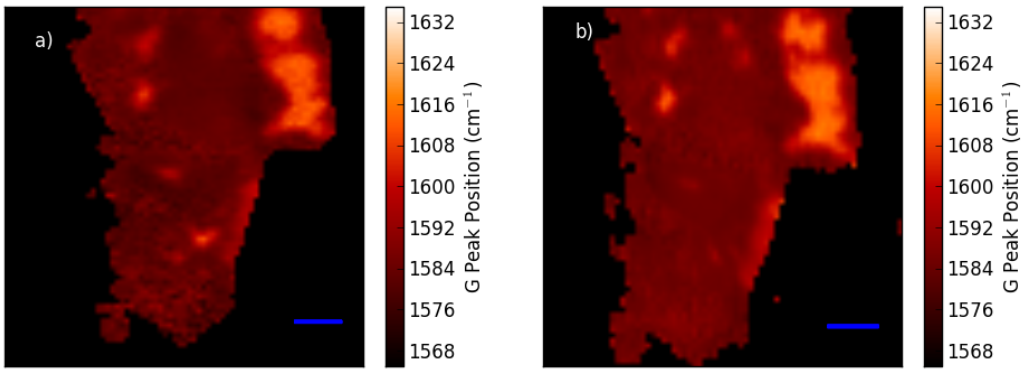

Figure 4.11: Raman maps of G peak position for sample 5-$MnCl_2$-CD. The Raman map in b) was taken 8 months after that of a), demonstrating the FLGIC to be stable as the large intercalated domain has not deintercalated during the 8 months.

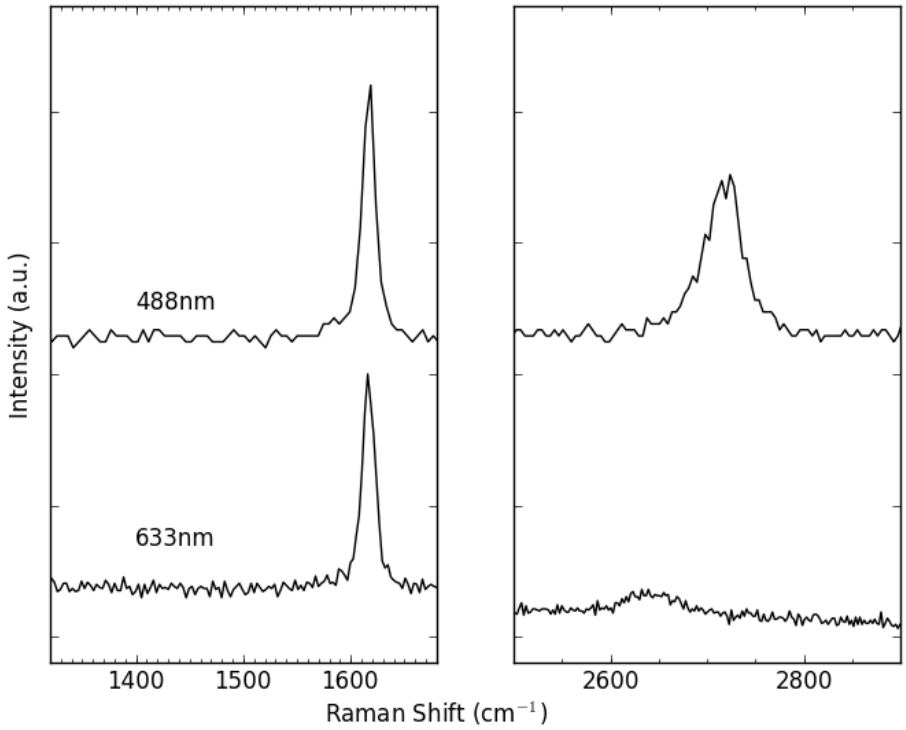

Figure 4.12: Raman spectrum of the intercalated domain in sample 5-$MnCl_2$-CD measured at 488 nm and 633 nm. The 2D peak position and intensity are seen to increase with increasing excitation energy while the G peak remains constant.

Chapter 5

Intercalated Domains Studied by Scanning Probe Microscopies

In this chapter EFM results are presented for samples 5-$MnCl_2$-CD and 5-$CuCl_2$-EC which have been measured previously by Raman spectroscopy (Figs.4.8 and 4.5) and contain intercalated domains. Measurements were performed on a Bruker Icon AFM at the National Physical Laboratory (NPL) with the assistance of Vishal Panchal. KPFM results are presented for sample 5-$MnCl_2$-CD, measured using an Asylum Research Cypher AFM at the Asylum Research Lab in collaboration with their engineer Mick Phillips. The corresponding AFM images are presented and discussed first.

5.1 AFM Images

Figures 5.1 and 5.2 show flake topographies measured during the first-pass AFM measurement that are required for subsequent EFM measurement. The difference in quality between the two AFM images is due to surface contaminants, perhaps from the adhesive tape, however both samples were fabricated using the same method. Flake topography is difficult to observe using AFM, see Fig.5.2, because of contamination. Removing the contamination from the samples by rinsing in solvents was not carried out, as this is thought to deintercalate the flakes.

Figure 5.1 shows the AFM measurement of sample 5-$MnCl_2$-CD with several areas labelled `1 - 7`. Labels `1` and `2` show regions with a height increase relative to the surrounding area and correspond to regions identified as intercalated domains from

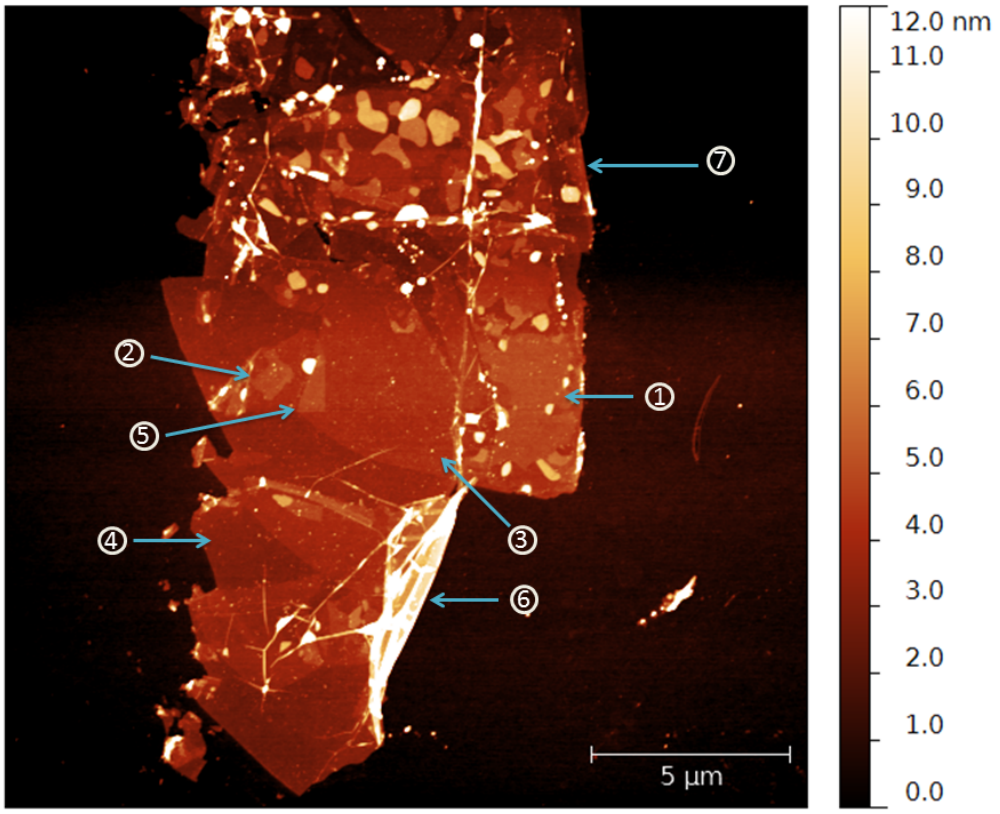

Figure 5.1: AFM height image of sample 5-$MnCl_2$-CD, previosuly measured by Raman spectroscopy in Fig.4.8. Regions of different thickness can be seen and are labelled as follows: 1 and 2 indicate regions that correspond to intercalated domains as measured previously by Raman spectroscopy. 3 and 4 are areas of the flake previously identified as bilayer and monolayer respectively through studies of Raman maps and optical contrast, the height step between these regions varies and is < 1 nm. The height step of the substrate to the flake at location 4 is ~ 4 nm, either in disagreement with the designation as a monolayer or indicating substantial residue trapped beneath the flake. 5 indicates a region where two bilayer regions intersect. 6 indicates where the flake has folded over/rolled up during fabrication. 7 indicates the location on the flake where oval/bulbous shaped features are observed which have height measurements of 2-7 nm above the surrounding area.

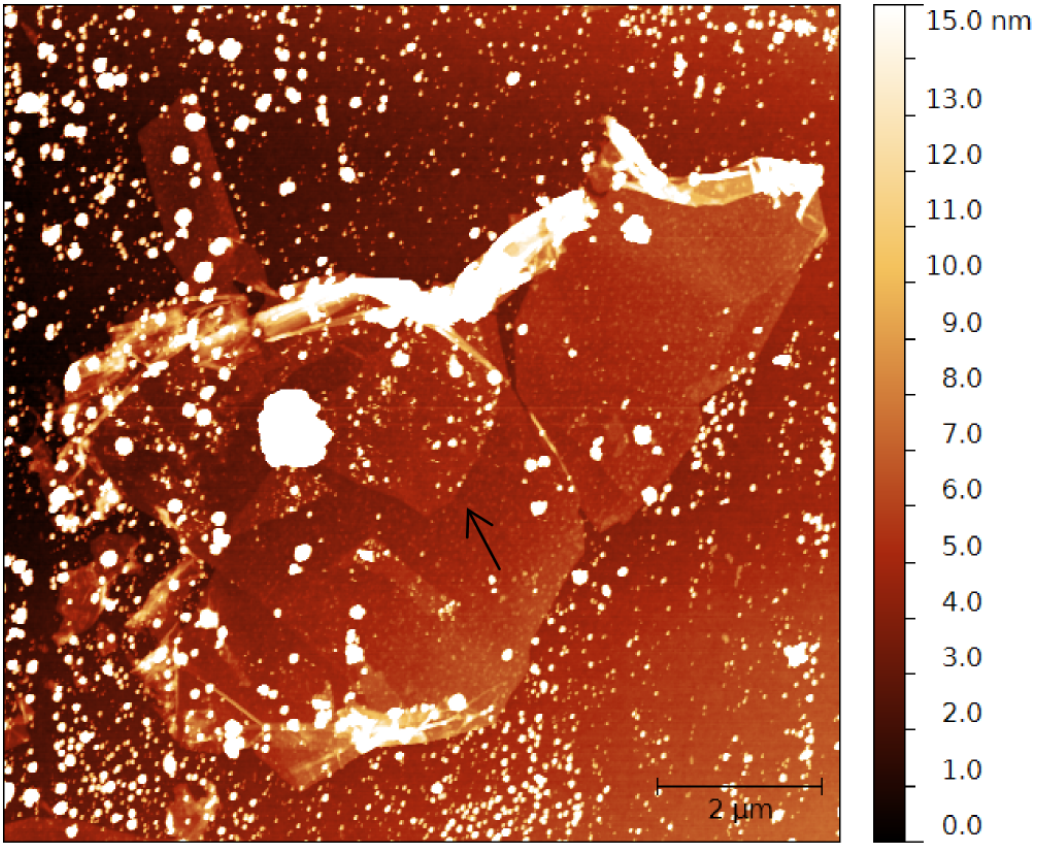

Figure 5.2: AFM height image of sample 5-$CuCl_2$-EC. Significant surface contamination is distorting the image. A intercalated domain indicated by the arrow (also seen in Raman Maps in Fig.4.5) can be observed due to the increased height.

Raman maps of G peak position (see Fig.4.8). The corners and some edges of the domain indicated by label 1 contain regions of greater height increase, perhaps due to intercalate taking on water and deintercalating. Figure 5.3 shows an average of 5 height profiles across the rectangular domain indicated by label 2, showing that the height increase due to the intercalate layer, is 0.7 nm, close to the expected 0.61 nm ($d_s = 0.95$ nm for $MnCl_2$). The height increase across the intercalated domains reveal that the host graphene layers are not suspended between domains, but maintain the regular 0.34 nm graphene layer separation away from the intercalated domains.

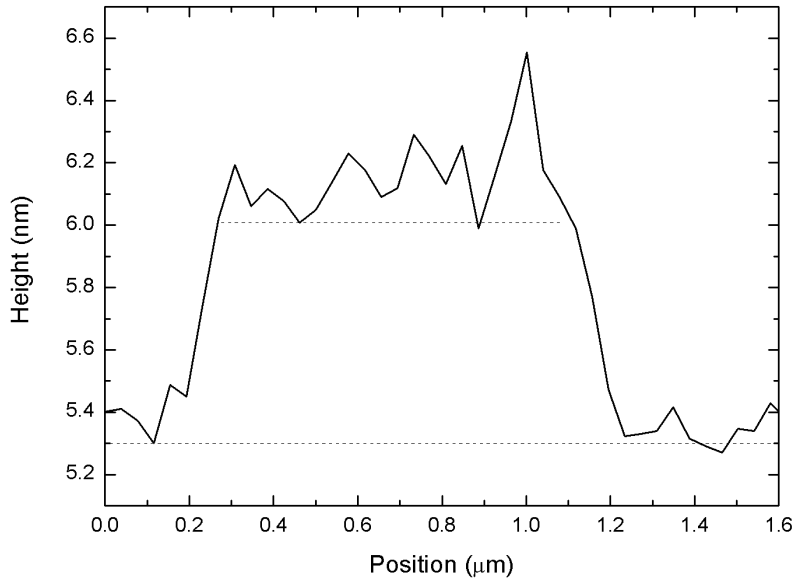

Figure 5.3: AFM profile of an intercalated domain of sample 5-$MnCl_2$-CD, showing the heights from 5 scans averaged across the domain labelled as 2 in Fig.5.1. The distance between the two dashed lines is ∼0.7 nm.

The regions labelled 3 and 4 in Fig.5.1 are bilayer and monolayer graphene, identified through a combination of optical contrast and Raman spectroscopy. A height step of of 0.5 nm between the two regions is obtained from an average of 25 profiles across the monolayer-bilayer boundary and is larger than the expected value of 0.34 nm. Further height measurements between the substrate and the monolayer parts of the flake give a height step of ∼2 nm, indicating a thickness of $5-6$ graphene layers where only one is expected, twice as large as the values from studies where a 'dead layer'[8] was

cited as increasing the thickness. It is possible that the thickness is increased by extra contamination as a result of the solvent free fabrication process or intercalate becoming exposed during exfoliation and absorbing extra water that is then trapped between the flake and the substrate.

5.2 EFM Images

Figures 5.4 and 5.5 show EFM phase images where the tip has retraced the topography from AFM measurement at a constant height of 20 nm above the flake surface and with an applied bias (V_{tip}) of -1.5 V between the tip and silicon back gate. The images reveal intercalated domains and changes in graphene layer number more clearly than their corresponding AFM images, and the surface contamination of the $CuCl_2$-intercalated sample is not as detrimental on the EFM images.

Figure 5.6 (a) shows EFM profiles obtained from an average of 5 scans across sample 5-$MnCl_2$-CD along the red dashed line in the figure, with $V_{\text{tip}} = \pm 1.5$ V. Steps in phase can be seen at boundaries of intercalated domains or changes in the number of graphene layers. Flipping the polarity of the tip potential reverses the observed contrast of the flake, indicating that the change in phase observed is due to a change in surface potential and not capacitance (see equation 2.20). In contrast the phase measured over the bare substrate does not change when flipping the tip polarity, so capacitive effects between the tip and Si substrate due to the insulating layer of air (20 nm) and SiO_2 layer (300 nm) dominate in determining the phase.

Figure 5.7 shows a histogram of the values of phase from the EFM image of sample 5-$MnCl_2$-CD, peaks are observed corresponding to the substrate, intercalated domains as well as a distribution for the different number of graphene layers. The dashed line in Fig.5.4 encloses a region of phase values $\Phi = 8.6°$ that is unique to the rest of the flake, and is surrounded by a region of phase values $\Phi = 9.7°$, the same as that of intercalated domains, as confirmed by Raman spectroscopy. One could interpret that this region is an intercalated domain having an extra graphene layer on top, i.e, the intercalate layer has two graphene layers between it and the EFM probe located where $\Phi = 8.6°$ and one graphene layer between it and the probe located where $\Phi = 8.6°$. EFM could therefore be used to distinguish between the two configurations in i3L stacked flakes (CICC or CCIC), whereas analysis of the Raman spectra cannot.

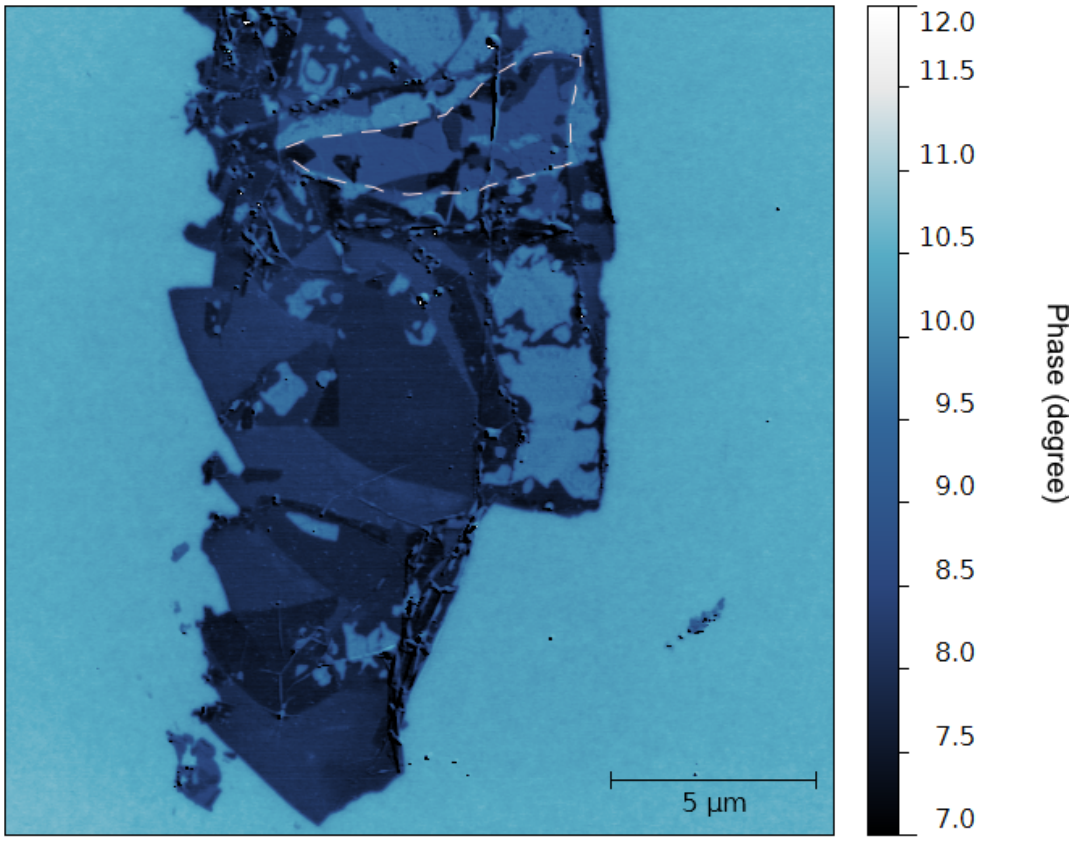

Figure 5.4: EFM phase image of sample 5-$MnCl_2$-CD taken with $V_{tip} = -1.5$ V and the tip at a constant height of 20 nm. Regions of the flake containing a different number of graphene layers (as identified in the AFM scan shown in Fig. 5.1) are clearly visible along with the intercalated domains. The phase shift of the intercalated domains with respect to the substrate is $\sim 1°$ and varying around $\sim 2.5°$ for the rest of the flake. The white dashed line encloses a region of phase unique to the rest of the image, probably due to an intercalate layer with two graphene layers above it. The oval/bulbous shaped features visible in the AFM image are not observed in the EFM image.

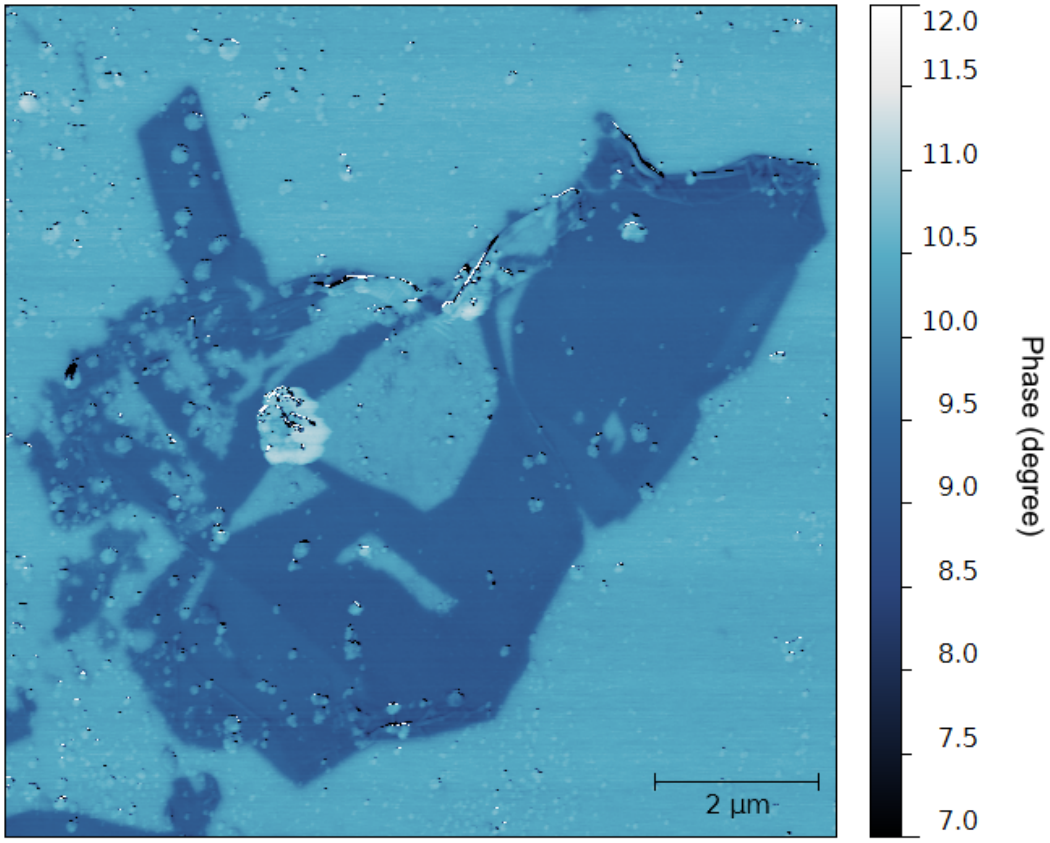

Figure 5.5: EFM Phase Image of sample 5-$CuCl_2$-EC taken with $V_{tip} = -1.5$ V and the tip at a constant height of 20 nm. Intercalated domains are more visible than compared to the corresponding AFM image. Regions of different number of graphene layers can also be observed that were barely visible in the corresponding AFM image.

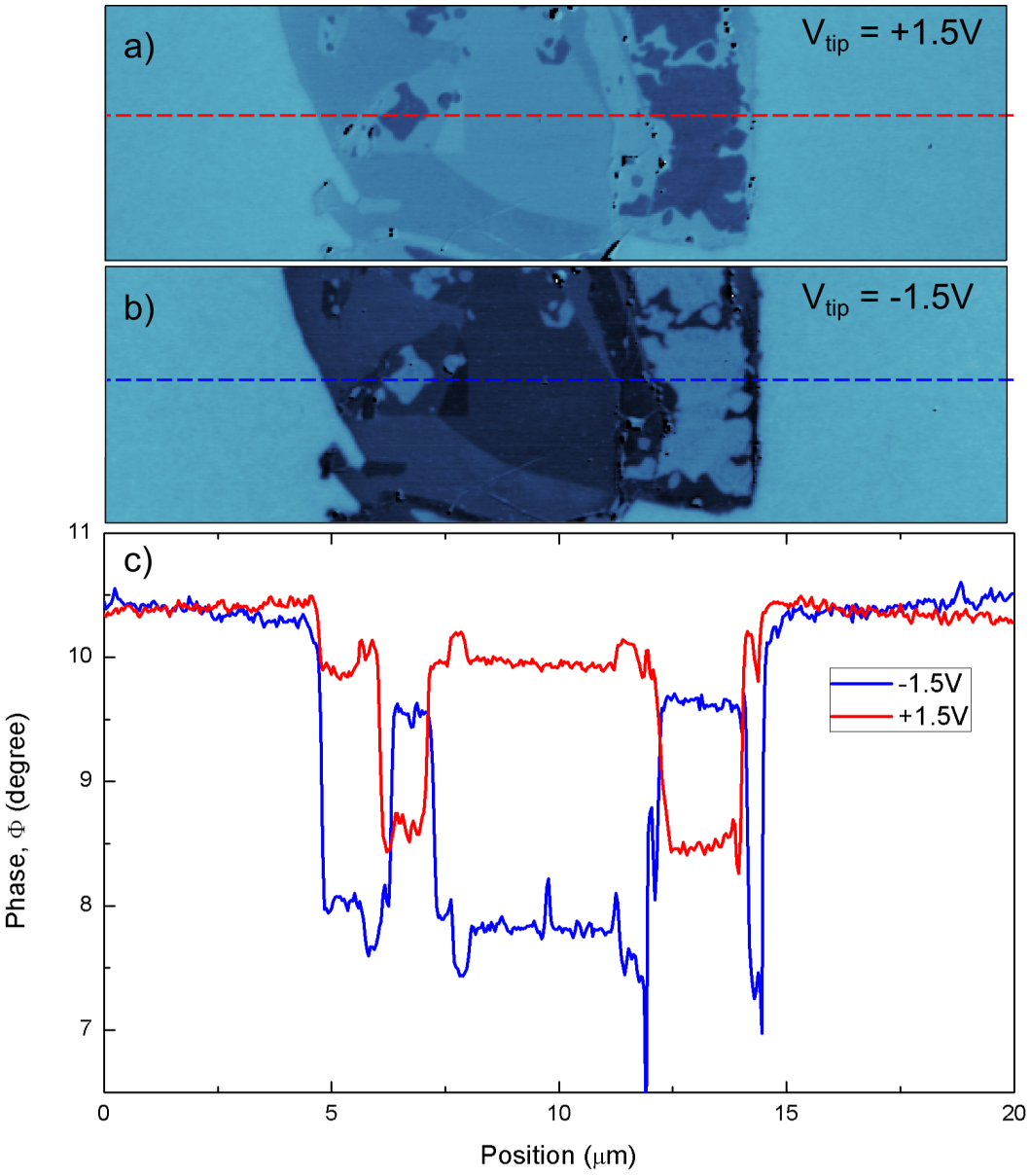

Figure 5.6: EFM profiles of sample 5-$MnCl_2$-CD with different values of V_{tip}. (a) The corresponding EFM image with $V_{\text{tip}} = +1.5$ V and (b) $V_{\text{tip}} = -1.5$ V from which the (c) profile along the dashed lines were taken. The tip height was 20 nm above the sample surface for both scans. The phase measured across the flake reverses when changing the tip polarity but does not over the substrate.

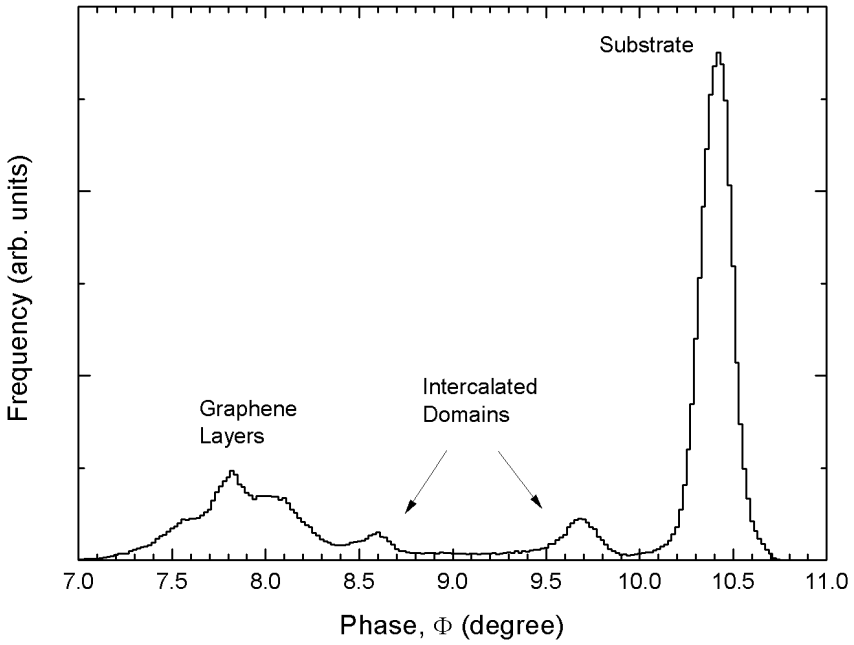

Figure 5.7: Histogram of EFM phase for sample 5-$MnCl_2$-CD imaged in Fig. 5.4. The substrate (10.4°), intercalated domains (9.7° and 8.6°) and the graphene layers (7.6° − 8.2°) are labelled according to the identifications in the EFM image

Comparing the AFM and EFM images of the $MnCl_2$-intercalated sample in Figs.5.1 and 5.4, most features are visible in both, with the exception of the oval/bulbous features seen at position 7 in the AFM image. The material causing oval/bulbous features therefore does not effect the electrostatic force being applied to the EFM tip, however they are positioned primarily in positions identified as intercalated domains.

5.3 Quantitative EFM Measurements

The surface potential at points across the $MnCl_2$-intercalated flake was measured by varying V_{tip} and finding the apex of the parabola as described in section 2.5. Figure 5.8 shows the result of measurements over points 2, 3 and 4 labelled in Fig.5.1 which correspond to an intercalated domain, monolayer and bilayer graphene and the substrate. An average from five V_{tip} sweeps was used from each region and a parabola fit to the data to obtain the surface potentials of -0.18 V for the intercalated domain, 0.22 V for the monolayer, 0.34 V for the bilayer and 0.21 V for the substrate.

Doping of graphene is expected to be p-type for both the $MnCl_2$ intercalate layer[48] and the SiO_2 substrate[8]. The change in sign of the graphene surface potential at the intercalated and non-intercalated regions is then not due to a shift from p-type to n-type doping but suggests the potential of the whole flake is offset and is floating, since only the Si back gate was grounded, not the flake itself.

The bilayer region has a measured surface potential greater than that of the monolayer region in agreement with the Thomas-Fermi theory[95], where the potential increases for thicker flakes. The intercalated domain has a measured surface potential that is less than that of the non-intercalated monolayer region, and since both regions have the same electric field screening due to one graphene layer above the charges (in the SiO_2 substrate or intercalate layer), the charge density in the intercalate layer must be greater than that in the SiO_2 layer, following the result of the Thomas-Fermi theory (see Fig.2.27).

Varying V_{tip} over the bare substrate produces a parabola of a different shape to that of over the flake, indicating it to have a different capacitance, since the quality factor and spring constant of the cantilever were kept the same.

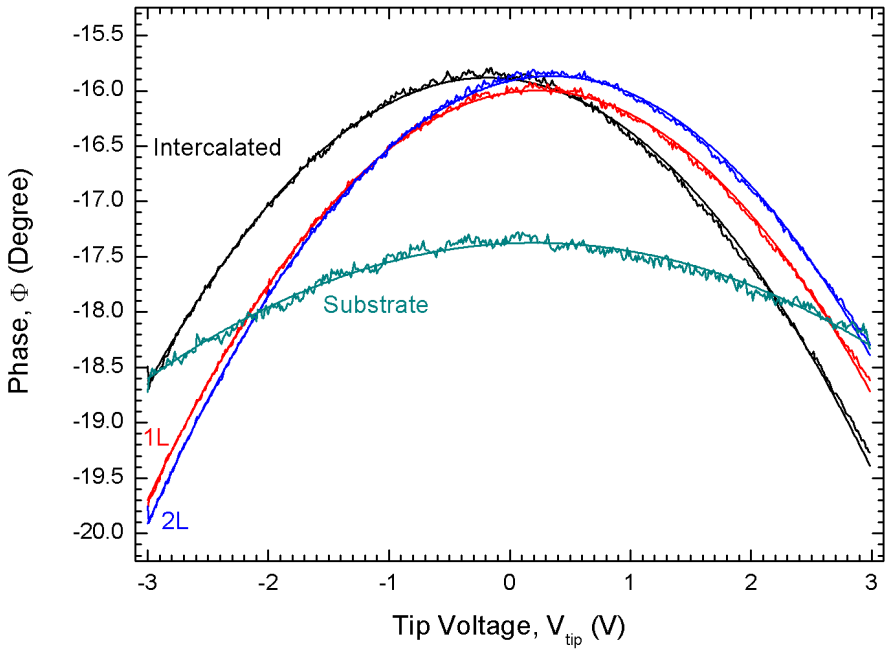

Figure 5.8: V_{tip} is varied in EFM Mode at various positions over sample 5-$MnCl_2$-CD to measure surface potential. Each trace in the plot represents an average of 5 measurement at a constant position 15 nm above a given region; intercalated bilayer domain (black), monolayer graphene (red), bilayer graphene (blue) and the Si/SiO_2 substrate (grey) as indicated in Fig.5.1. Parabolic curves have been fitted to the data to find the point where $V_{\text{tip}} = V_{\text{surface}}$ at the apex as described by equation 2.20. Values obtained for V_{surface} are -0.18 V for the intercalated domain, 0.22 V for monolayer graphene region, 0.41 V for the bilayer region and 0.21 V for the substrate.

5.4 KPFM Images

Figure 5.9 shows the KPFM image of sample 5-$MnCl_2$-CD, focusing on the intercalated domain. The image contains horizontal distortions as rapidly varying topography caused the tip to come into contact with the surface, contaminating the tip for a period of time.

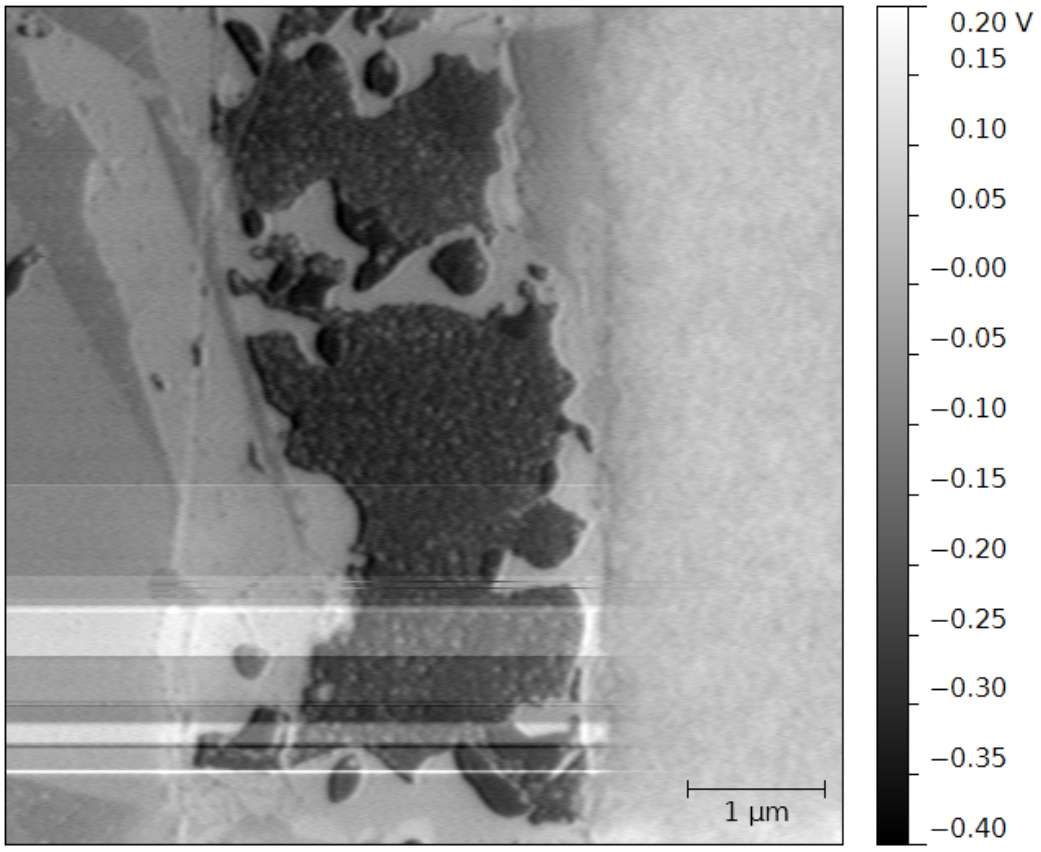

Figure 5.9: KPFM image of sample 5-$MnCl_2$-CD showing the same structures observed previously. The scars in the image are due to the tip picking up charged material from the surface and dropping it a several traces later. The intercalated domain has a negative surface potential which becomes more negative at some of the edges.

The intercalated domain structure seen in EFM images can be seen in KPFM, as well as variation in potential at some of the edges and corners of the domain, coinciding with height steps seen in the AFM image of Fig.5.1. It is possible this is a result of partial deintercalation at the edges and the anhydrous $MnCl_2$ adopts the dihydrate or

tetrahydrate form, incorporating H_2O molecules into its structure.

Figure 5.10 shows a histogram of the KPFM image with the distorted regions excluded from the histogram calculation. Peaks of distinct surface potential can be seen and can be identified as intercalated regions, non-intercalated regions and the substrate. The values of surface potential obtained from KPFM are not the same as those from quantitative EFM measurement but the relative position of the values are. The difference in surface potential measured between EFM and KPFM for the intercalated domain is $\sim$1 V and varies between 3 V and 5 V for the non-intercalated regions depending on number of graphene layers. The surface potential across the whole flake is negative in the KPFM measurement. The KPFM voltage was applied between the tip and the Silicon layer (back gate) and not the flake directly, therefore it is possible it will float up to a different potential and the measured values of surface potential may be offset causing a difference between EFM and KPFM measurements.

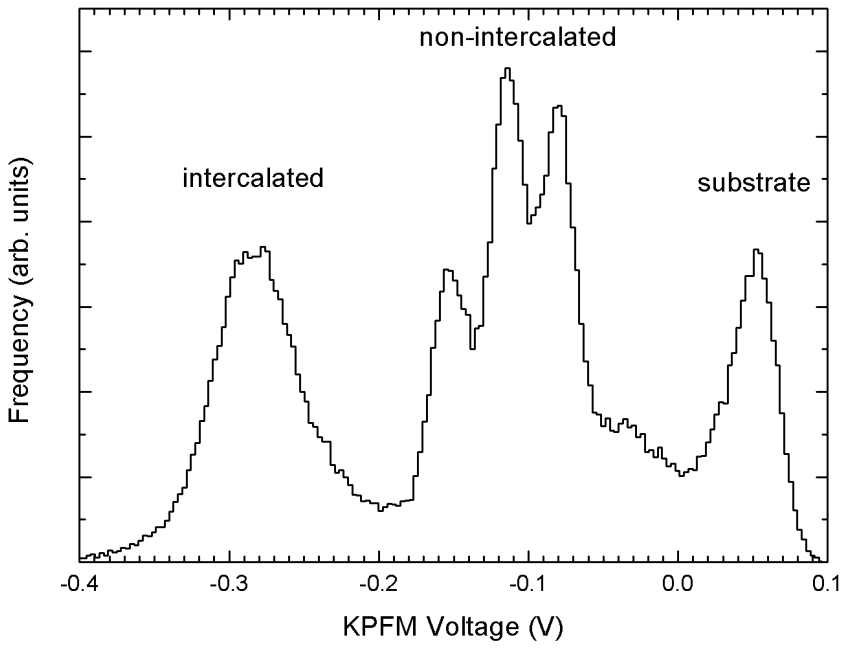

Figure 5.10: Histogram of KPFM voltages for sample 5-$MnCl_2$-CD imaged in Fig.5.9. The KPFM voltage used for the histogram are taken from the non-scarred areas of the image only and peaks corresponding to regions in the image have been labelled. Three peaks are observed across the non-intercalated regions and can be attributed to monolayer, bilayer and trilayer graphene. The peak at 0.28 V, corresponding to the surface potential of the intercalated domain, differs from the value (-0.18 V) obtained by EFM measurement in Fig.5.8.

Chapter 6

Electronic Transport in FLGICs

FLGICs were fabricated into devices consisting of source and drain contacts and a back gate as illustrated in Fig. 3.11. Table 6.1 lists the samples fabricated into devices and lists the measured resistance and position of the Dirac point. Samples that were found to be unusable after fabrication are omitted from the table. Measurements are performed at 4.2 K in ^{4}He, or 30 mK in a dilution refrigerator where a magnetic field was used.

6.1 Sweeping the Back Gate

The devices fabricated allow for twoterminal resistance measurements of the FLGICs, where a voltage can be applied to the back gate, modifying the carrier concentration in the graphene layers (given by equation 3.6). The voltage applied to the back gate is varied and a peak in resistance is observed, indicating the Fermi level in the graphene layers has returned to the charge neutrality point (Dirac point). For 9 of the 25 samples measured, no variation in resistance was observed when sweeping the back gate, indicating a faulty back gate.

6.1.1 FLGIC Samples

Figure 6.1 shows typical measurements from 3 FLGIC devices, no peak in resistance is observed in the region the gate could safely be swept without breakdown of the SiO_2 insulating layer. No differences are observed in the measurements relating to differences in the intercalate compound used in the FLGIC. The resistance of the FLGICs increases

Sample Number	Material Exfoliated	Measured Two Terminal Resistance	Dirac Point	Comments
01	Stage-1 $CoCl_2$ GIC	18 kΩ	30 V	
02	Stage-1 $CoCl_2$ GIC	4000 Ω	>100 V	
04	Stage-1 $CoCl_2$ GIC	350 Ω	>100 V	
05	Stage-1 $CoCl_2$ GIC	3100 Ω	-	
07	Stage-1 $MnCl_2$ GIC	1100 Ω	>100 V	
08	Stage-1 $CoCl_2$ GIC	600 Ω	20 V	
09	Kish Graphite	30 kΩ	-	
10	Kish Graphite	200 Ω	-	
11	Kish Graphite	1400 Ω	0 V	
12	Kish Graphite	300 Ω	-	
14	Kish Graphite	25 kΩ	0 V	
15	Kish Graphite	200 Ω	-	
17	Stage-1 $CoCl_2$ GIC	250 Ω	>100 V	
18	Stage-1 $CoCl_2$ GIC	3200 Ω	0 V	
20	Stage-2 $NiCl_2$ GIC	75 Ω	>100 V	
21	Stage-2 $NiCl_2$ GIC	80 Ω	>100 V	
23	Stage-2 $NiCl_2$ GIC	400 Ω / 6300 Ω	>100 V / 0 V	Sample changed after annealing
25	Stage-2 $NiCl_2$ GIC	1400 Ω	0 V	Cleaned in Isopropanol
26a	Stage-1 $MnCl_2$ GIC	280 Ω	>100 V	
26b	Stage-1 $MnCl_2$ GIC	150 Ω	20 V	
27	Stage-1 $MnCl_2$ GIC	900 Ω	>100 V	
28	Stage-1 $MnCl_2$ GIC	160 Ω	-	
30a	Stage-1 $MnCl_2$ GIC	2600 Ω	-	
30b	Stage-1 $MnCl_2$ GIC	300 Ω	-	SdH oscillations observed
30c	Stage-1 $MnCl_2$ GIC	300 Ω	-	
30d	Stage-1 $MnCl_2$ GIC	13 kΩ	-	
32a	Stage-1 $MnCl_2$ GIC	2400 Ω	-	SdH oscillations observed
32b	Stage-1 $MnCl_2$ GIC	500 Ω	-	
32c	Stage-1 $MnCl_2$ GIC	1700 Ω	-	
32d	Stage-1 $MnCl_2$ GIC	300 Ω	-	

Table 6.1: List of samples showing the material exfoliated, the measured resistance and position of the Dirac point. Samples that were unusable after fabrication are not shown. No Dirac point is given if the back gate on the device could not be swept. A Dirac point given as > 100 V indicates the charge neutrality point was beyond the maximum voltage that could be applied to the back gate without breakdown of the SiO_2 insulating layer.

as the applied gate voltage becomes more positive, and the Dirac point must lay beyond 100 V. Using equation 3.5 it is calculated (using $n = 4 \times 10^{13}$ cm^{-2} estimated from Raman measurement of i2L FLGICs) that a gate voltage of 560 V is required to shift the Fermi level to the charge neutrality point and observe a peak in resistivity.

The measurement of sample-02 in Fig. 6.1 (a) shows that the resistance is approaching a maximum value, likely to be seen when V_g is around 150 - 300 V. It is reasonable for the peak to occur at less than the expected V$_g$ = 560 V since Raman measurements have shown the flakes to contain both intercalated and non-intercalated domains which would reduce the overall carrier density.

Table 6.1 shows that the Dirac point was not out of experimental range for all FLGICs measured. Sample-01 exhibited a peak in resistance at $V_g \approx 30$ V and sample-08 and sample-26b exhibited a peak in resistance at $V_g \approx 30$ V, indicating the samples to have lower levels of doping than the other FLGICs measured, most likely due to deintercalation during mechanical exfoliation. The measured resistance of sample-25 revealed the Dirac point to be at $V_g \approx 0$ V, explained by the device being left in IPA overnight to remove vacuum grease that was accidentally spread over the flake when attaching the shadow mask during fabrication. It appears the intercalate layers were removed from the FLGIC along with the vacuum grease and highlights the importance of the solvent free fabrication process.

The resistance of the flakes varies across the samples measured. Figure 6.1 shows that the sample resistance is lower for FLGICs which contain a higher estimated (from optical contrast) number of graphene layers, as each additional graphene layer provides and extra channel for conduction.

6.1.2 Pristine Graphene Samples

Pristine few-layer graphene samples (exfoliated from Kish graphite) were measured to confirm that the doping seen in the FLGIC samples is due to the presence of intercalate layers and not contamination from other sources that the sample may have been exposed to during the fabrication process. Figure 6.2 shows the typical result from a kish exfoliated flake containing an estimated (from optical contrast) 2 graphene layers. The Dirac point is seen at 0 V indicating that the Fermi level is at the charge neutrality point. The inset of Fig. 6.2 shows the Dirac point to be at 0 V before current annealing took place (used to clean the samples), indicating no contamination was introduced

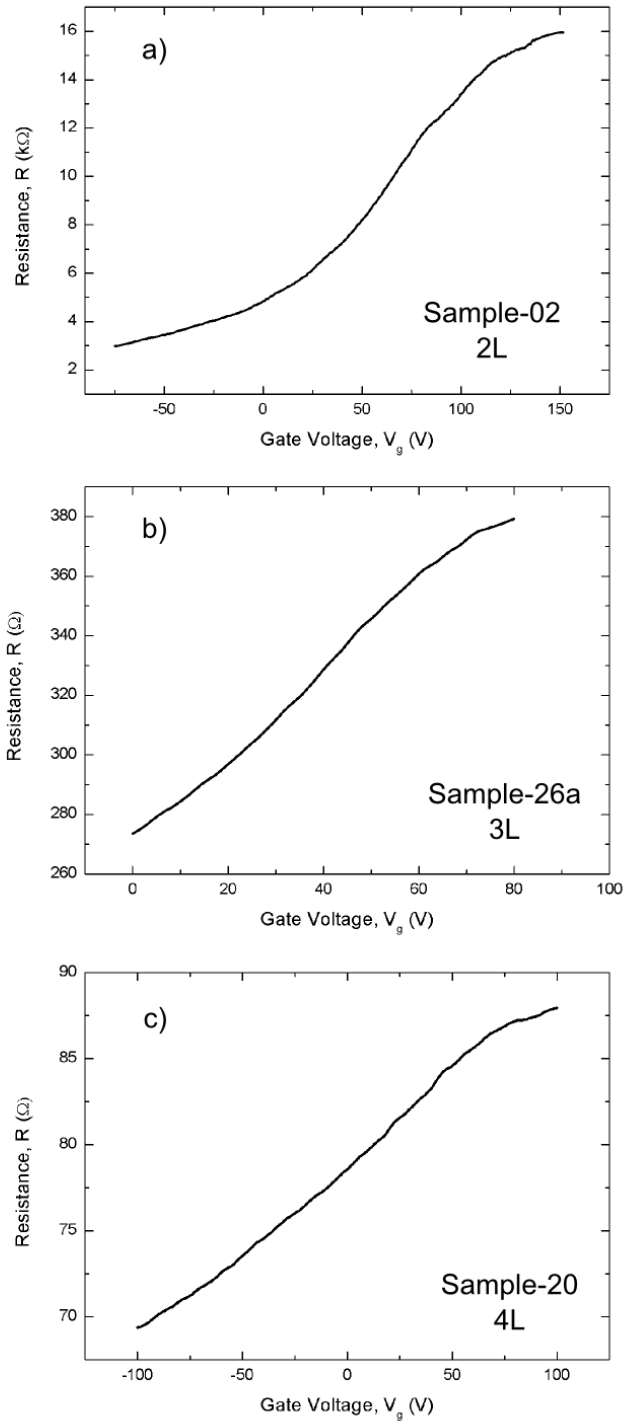

Figure 6.1: Resistance measured across FLGICs with the back gate voltage being varied, the samples used and the corresponding number of graphene layers from optical contrast are given. The data has been averaged over several sweeps to remove the noise. Resistance increases as the gate voltage becomes more positive, no peak in resistance is seen for the range measured. The different resistances measured across the samples can be attributed to different number of graphene layers in each.

during fabrication, and that the the dry fabrication method was successful in reducing contamination that has been seen when using e-beam lithography techniques due to resist residue[119] that can introduce unwanted doping.

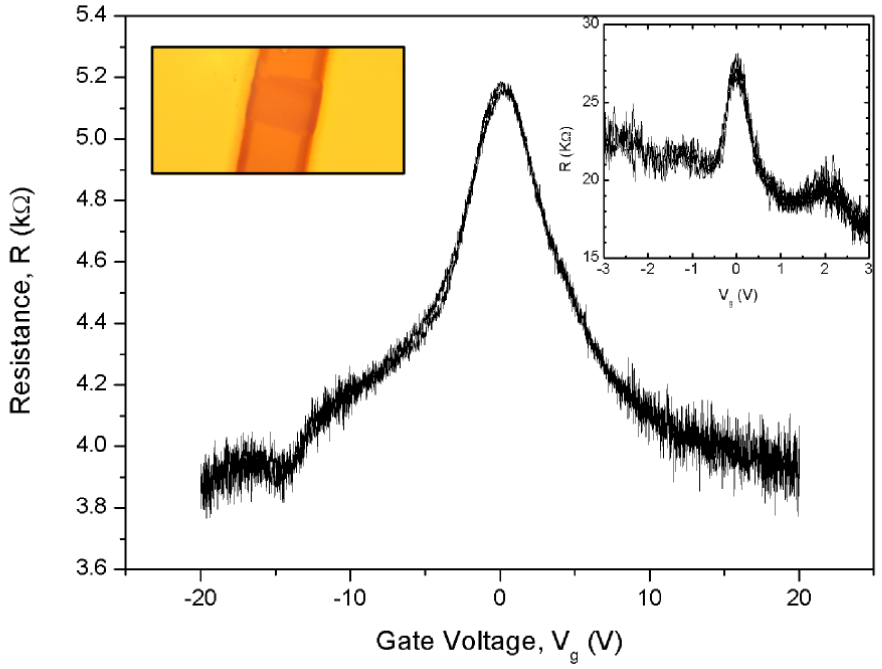

Figure 6.2: Resistance measured across a non-intercalated 2L flake (sample-14) with the back gate voltage being varied at $T = 4.2\,\mathrm{K}$. Left insert: Optical image of the device where the distance between the gold contacts is 10 μm. Right insert: Measurement before current annealing. A peak in resistance is seen around 0 V indicating the sample to be un-doped. Measurement before current annealing shows the Dirac peak to be at 0 V, indicating that any contamination from fabrication does not introduce any significant levels doping.

The intercalated flakes have lower measured resistances than those of the kish exfoliated samples, where measured resistances were >1 kΩ. Here the intercalate layer improves the conduction of the graphene layers through hole doping. Figure 6.2 shows that the peak in resistance around 0V of sample-14 widened and became more symmetric after current annealing, and that the the total resistance of the device decreased (measurement set up was kept the same). It may be that annealing removed contamination that increased the resistance through electron scattering but did not significantly dope the sample or that the changes observed are due to improvement in the ohmic

contacts from annealing.

6.2 Measurements in a Perpendicular Magnetic Field

Figure 6.3 shows the resistance of samples that were measured in a magnetic field up to 12T inside a dilution refrigerator at 30 mK. Eight samples were mounted onto the fridge (samples 30a-d and 32a-d), of which only three (samples 30a, 30b and 32a) were working after mounting. Damage to the samples may have occurred during soldering of wires from the probe to the sample, heating the FLGICs. Due to time constraints no other solution could be developed, such as that used on the ^{4}He dipping probe.

For the measurement of FLGICs shown in Fig. 6.3 the resistance is lower than that measured for non-intercalated flakes containing the same number of graphene layers (samples 9-15), indicating that the flakes do contain intercalate layers. In general the measured resistance of the samples increases when a perpendicular magnetic field is applied, in agreement with other studies[90, 91] of $FeCl_3$ FLGICs. The noise makes it difficult to identify Shubnikov de Haas (SdH) oscillations in the measured resistance.

Figure 6.4 shows the same data from Fig. 6.3 but with the noise reduced by averaging over adjacent data points and the inverse magnetic field is plotted to make peaks in SdH oscillations equidistant. SdH oscillations at two frequencies are indicated in Fig. 6.4, one high frequency oscillation due to graphene layers doped by intercalate and one low frequency due to undoped graphene layers, that are present in FLGICs with i3L structure. The fast SdH oscillations identified for sample-30b are 0.012 (1/T) apart, using equation 2.13 this gives a carrier density of $n = 8 \times 10^{12}$ cm^{-2}. The average distance between the high frequency oscillations of sample-32a is 0.005 (1/T) corresponding to a carrier density of $n = 1.9 \times 10^{13}$ cm^{-2} and is near the carrier density of $n = 4 \times 10^{13}$ cm^{-2} obtained from Raman spectroscopy of a FLGIC with i2L structure. The low frequency oscillation of sample-32a corresponds to lower carrier density of $n = 1 \times 10^{11}$ cm^{-2}.

6.3 Current Annealing of FLGICs

An interesting change was observed in the measurements of sample-23 after current annealing. Figure 6.5 (a) shows the measured resistance as a function of gate voltage

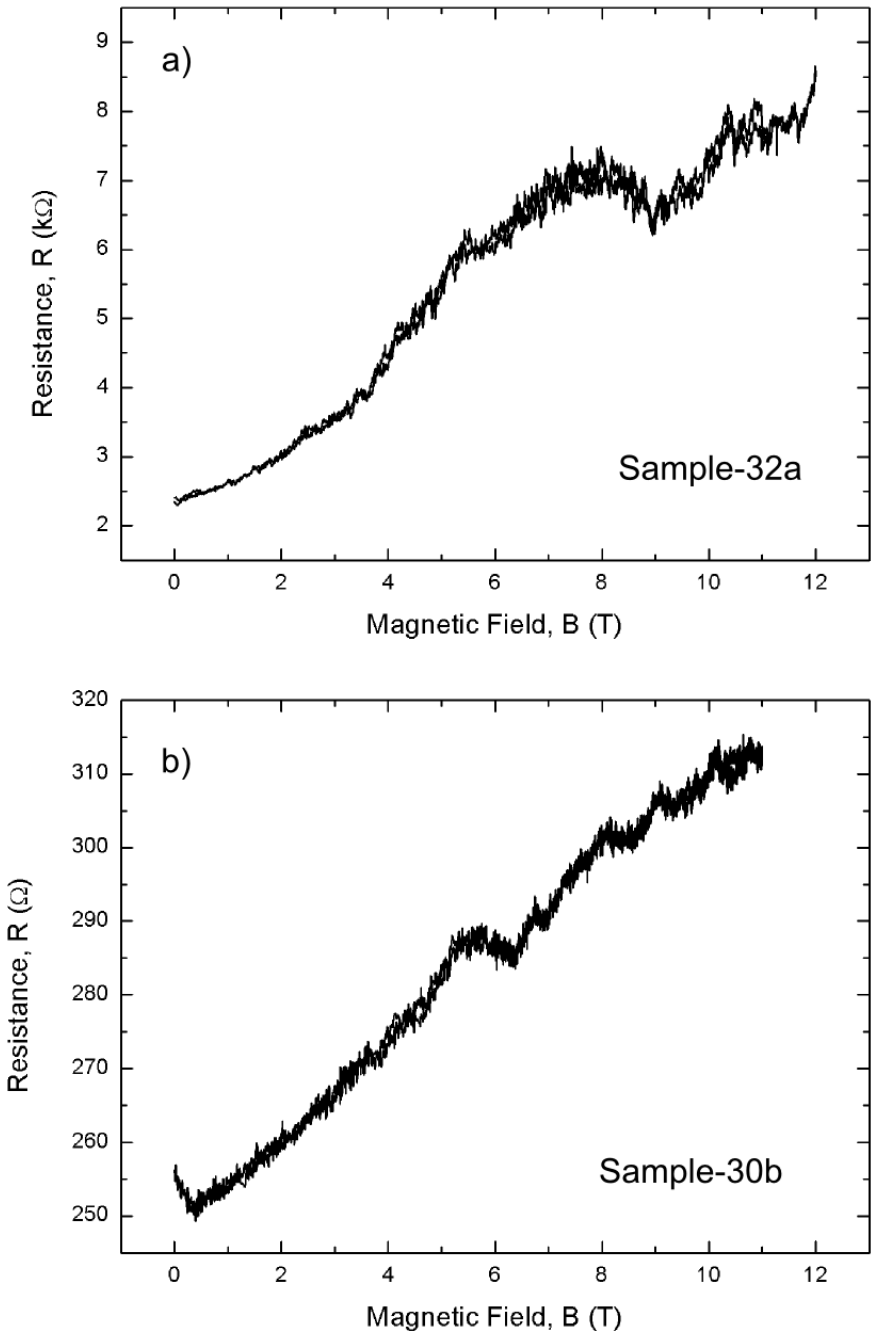

Figure 6.3: Measurements of FLGICs in a magnetic field at 30 mK. Sample-32a contains 2 graphene layers and sample-30b 4 graphene layers (estimated from optical contrast).

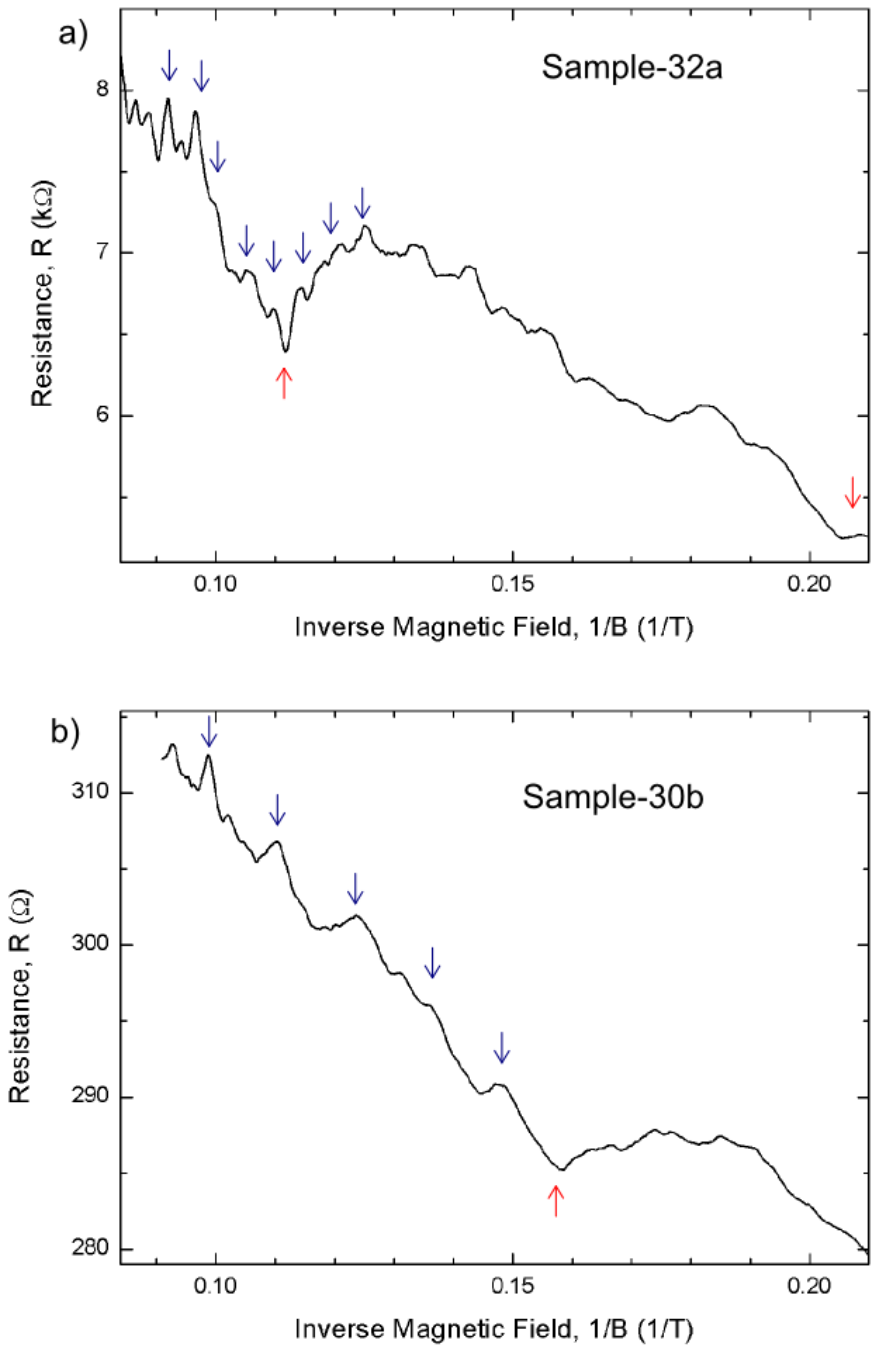

Figure 6.4: Resistance of FLGICs plotted against inverse magnetic field to make SdH oscillations appear equidistant, $T = 30\,\mathrm{mK}$ The data has been smoothed which makes oscillations with two distinct frequencies visible. Blue arrows indicate peaks of the high frequency oscillations and red arrows for peaks the low frequency oscillations. Oscillations are more pronounced at high magnetic fields.

before current annealing and Fig. 6.5 (b) measurement afterwards. Before annealing the measured resistance exhibits the typical behaviour for a FLGIC with no Dirac point observed in the range that V_g was swept, then after annealing the Dirac point was observed at 0 V and the resistance of the sample has increased, exhibiting features typical for a non-intercalated sample and indicates that sample-23 deintercalated during annealing.

Figure 6.6 shows a section of the source-drain current during annealing. When the voltage is held at 2.5 V the current decreases steadily for $\sim$ 3 minutes, indicating that doping contaminants are slowly desorbed from the graphene surface, shifting the Dirac point towards 0 V increasing the resistance at $V_g = 0$ V. When the bias was increased to 2.6V (ramped in two 0.05 V steps), around the 19 minute mark the current fluctuates for 30 seconds and then sharply drops to 0.55 mA from 4.70 mA, indicating that de-intercalation took place and that the process occurred almost instantaneously. The resistance of the sample increases after annealing, so it is probable that the outer graphene layer was removed through sublimation, hence reducing the number of graphene layers and leaving an unstable intercalate layer exposed.

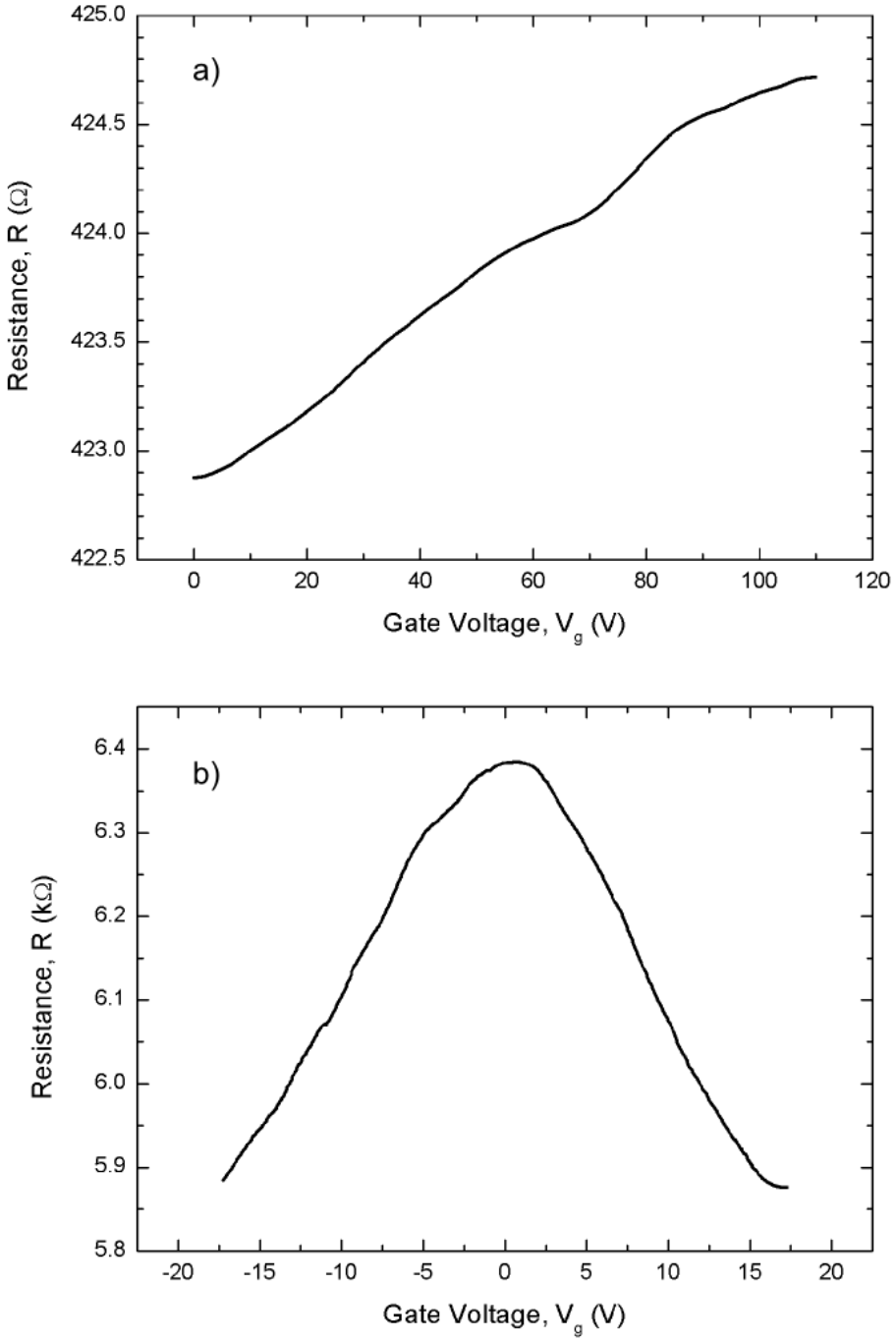

Figure 6.5: Sample-23 measured (a) before current annealing and (b) after current annealing at $T = 4.2\,\mathrm{K}$. The dirac point can be seen at 0 V after annealing indicating the sample to have deintercalated between measurements.

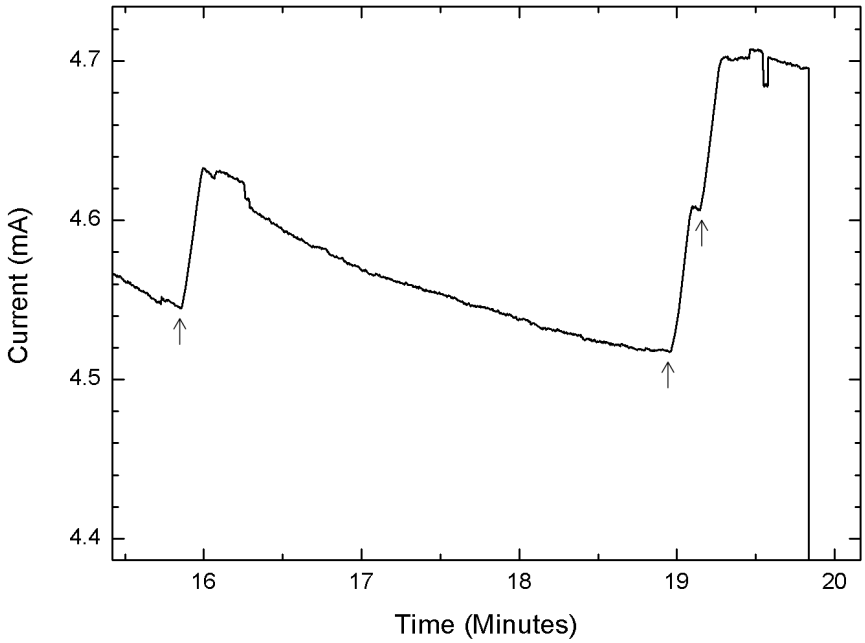

Figure 6.6: Measured current during annealing of FLGIC Sample-23 at $T = 4.2\,\mathrm{K}$. The arrows indicate the times when the source-drain voltage was incrementally increased and then held constant for a few minutes annealing the sample with the high current induced. At ∼16 minutes the voltage was increased from 2.45 V to 2.5 V. The voltage was increased again to 2.6 V three minutes later whereby the current of the sample sharply dropped to 0.55 mA.

Chapter 7

Conclusions and Future Work

This thesis has demonstrated the feasibility of fabricating new few-layer graphene intercalation compounds (FLGICs), by the exfoliation of stage-1 and stage-2 GICs, for a range of intercalation compounds ($CoCl_2$, $MnCl_2$, $CuCl_2$, $NiCl_2$ and $FeCl_3$). FLGICs containing a single intercalate layer have been identified by Raman spectroscopy which can form the basis of studies into model 2D magnets. The graphene layers in FLGICs are shown to be highly p-doped by the intercalate layers while the visibility is largely unchanged by them, this makes FLGICs a better candidate than graphene to replace indium tin oxide as the transparent conductor of choice in future commercial electronic devices.

Measurements of the Raman G peak position of FLGICs are used to estimate the carrier concentration as $n_{\mathrm{i2L}} = 4.1 \times 10^{13}$ cm^{-2} for the graphene layers in a intercalated bilayer (i2L) flanked by intercalate on one side and $n_{\mathrm{ii3L}} = 8.3 \times 10^{13}$ cm^{-2} for the inner graphene layer in fully intercalated trilayer (ii3L) that is flanked by intercalate on both sides. Transport measurements of FLGICs reveal the carrier concentration in the graphene layers to be up to $n = 1.9 \times 10^{13}$ cm^{-2} from the SdH oscillations.

FLGICs fabricated by mechanical exfoliation have been shown to contain intercalated domains several microns across from maps of Raman G peak position and AFM/EFM/SKPM images. Figure 7.1 shows the FLGIC from sample 5-Mn-CD imaged optically, by a Raman map of G peak position, by AFM and EFM, where it can be seen that EFM is the superior technique for imaging the domain structure. EFM and KPFM have been used to measure the surface potential of intercalated domains and the non-intercalated regions of exfoliated flakes. In the future more accurate val-

ues of surface potential could be obtained if the flake being measured was connected to ground via an ohmic contact, instead of the back gate as was the situation in this thesis.

Raman spectroscopy was the superior technique for identifying the stacking arrangement of graphene and intercalate layers by the analysis of the G_0, G_1 and G_2 components of the G-band of the Raman spectra. Raman measurements of the 2D peak lineshape reveal the graphene layers to be decoupled in the intercalated domains and the non-intercalated regions, suggesting the flakes measured were intercalated uniformly, decoupling the graphene layers everywhere. The intercalated domains would then be formed by partial deintercalation of the intercalate layers, most probably deintercalating when the FLGICs were fabricated by mechanical exfoliation.

The hygroscopic and deliquescent compounds used in this study were found to be air stable in FLGICs since they are enclosed by graphene layers. Raman maps of sample 5-$MnCl_2$-CD taken 8 months apart revealed intercalate domains to remain constant with no deintercalation taking place, despite being exposed to air during that time. Evidence of deintercalation was observed from the Raman maps of sample 6-$FeCl_3$-BB where changes to the domain size was seen over 24 hours. AFM and KPFM images of sample 5-$MnCl_2$-CD showed some edges of the intercalated domain to have a variation in the surface potential and bulbous shaped height steps, possibly due to intake of moisture from the air. Deintercalation of a FLGIC was shown to occur when applying a high current ($> 4.5\ mA$) during annealing and FLGICs were seen to be structurally damaged when heated during soldering and bonding.

7.1 Future Work

Fabricating FLGICs into Hall bar devices would allow for four-terminal measurements with reduced noise compared to two-terminal measurements, making SdH oscillations easier to identify. A shadow mask more complex than the TEM grid used could be implemented to achieve fabrication of Hall bar devices, however this comes with the difficulty of aligning the mask with the position of exfoliated FLGICs. Well developed e-beam lithography techniques can produce Hall bar devices of graphene flakes. To apply the techniques to FLGICs the stability of FLGICs exposed to the chemicals used during e-beam lithography would need to be investigated.

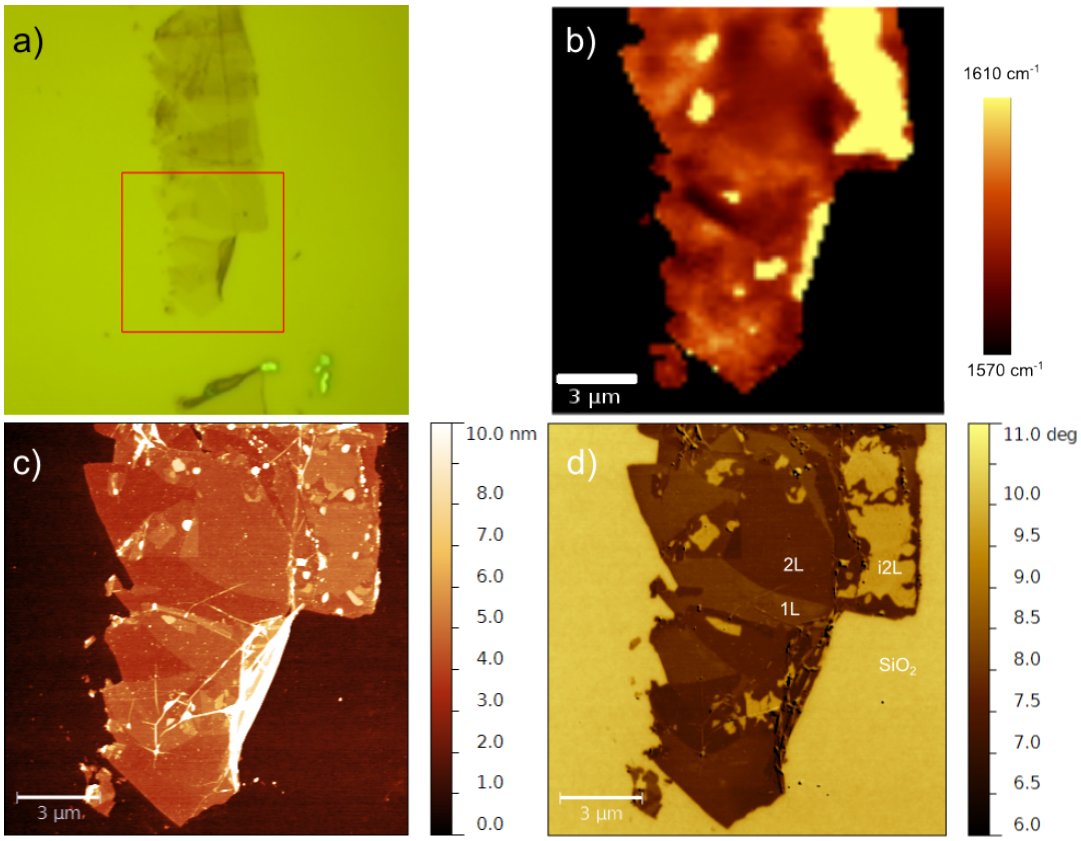

Figure 7.1: A comparison of techniques used to image sample 5-$MnCl_2$-CD. (a) Optical image under green light to enhance contrast, the square indicates area used for other images. (b) Raman map of G peak position, (c) AFM height Image and (d) EFM phase image. The intercalated domain (i2L) cannot be distinguished in the optical image and is most clearly visible with good resolution in the EFM measurement.

Deintercalation of FLGICs has been demonstrated to occur in this thesis through mechanical exfoliation, current annealing and exposure to moisture in the air. If FLGICs are to be used as transparent conductors in electronic devices the stability of FLGICs requires further study. Producing Raman maps of FLGICs at regular time intervals for each of the intercalation compounds would reveal the rate at which deintercalation in air occurs.

For FLGICs to replace indium tin oxide (ITO) as the leading transparent conductor, large scale fabrication methods are required. The most feasible method would be to directly intercalate large few-layer graphene sheets[120], where the optimal parameters for intercalation would have to be investigated. For use in flexible electronic devices the effect of the incommensurate intercalate layers on the flexibility of FLGICs needs to be investigated. The optical properties of FLGICs would need to be studied if they are to be used as transparent conductors. FLGICs could be transferred to transparent substrates such as glass to be used for optical transmission experiments. A recent study of $FeCl_3$ FLGICs[91] has measured a transmittance of 84%, which is comparable to commercially available ITO.

FLGICs containing a single intercalate layer have been identified in this thesis and provide an excellent opportunity to study low-dimensional magnetic phase transitions, where the graphene layers act as a benign mechanically strong host. The temperatures at which magnetic phase transitions occur can be studied by measuring the temperature dependence of the in-plane resistivity in FLGICs . Transport measurements of $CoCl_2$ GICs[7] show a peak in in-plane resistivity at temperatures of a magnetic phase transition ($\sim$ 10 K) and resistivity measurements of $FeCl_3$ FLGICs[90] show a peak at 15 K possibly due to a magnetic phase transition.

Direct measurements of the order parameter (magnetisation) will represent a challenge due to the size of the intercalated domains. One route would be to use a nano-superconucting quantum interference device[121] (nano-SQUID), however the planar sub-micron sized pick-up loops can only measure magnetic fields perpendicular to the substrate. To measure spins from a 2DXY magnet (such as Co^2+ ions in $CoCl_2$) out of plane pick-up loops are required, such pick-up loops have been demonstrated possible[122] to fabricate using focused-ion-beam-induced chemical vapor deposition and could potentially be fabricated adjacent to the FLGIC of interest.

References

[1] Akshay Kumar and Chongwu Zhou. **The race to replace tin-doped indium oxide: which material will win?** *ACS nano*, **4**:11, 2010. 1

[2] David S Hecht, Liangbing Hu, and Glen Irvin. **Emerging transparent electrodes based on thin films of carbon nanotubes, graphene, and metallic nanostructures.** *Advanced materials*, **23**:1482, 2011. 1

[3] Jung-Yong Lee, Stephen T Connor, Yi Cui, and Peter Peumans. **Solution-processed metal nanowire mesh transparent electrodes. 8**:689, 2008. 1

[4] C A F Vaz, J A C Bland, and G Lauhoff. **Magnetism in ultrathin film structures**. *Reports on Progress in Physics*, **71**:056501, 2008. 1, 2

[5] K. Fritsch, R. D'Ortenzio, and D. Venus. **Observation of mixed anisotropy in the critical susceptibility of an ultrathin magnetic film**. *Physical Review B*, **83**:075421, 2011. 2

[6] A. Liebig, P. T. Korelis, Martina Ahlberg, and B. Hjörvarsson. **Experimental realization of amorphous two-dimensional XY magnets**. *Physical Review B*, **84**:024430, 2011. 2

[7] G Dresselhaus, J. T Nicholls, and M. S. Dresselhaus. **Graphite Intercalation Compounds II**. *Springer Series in Material Science*, **18**:217–345, 1992. 2, 18, 19, 114

[8] K. S. Novoselov, AK Geim, SV Morozov, D. Jiang, Y. Zhang, SV Dubonos, IV Grigorieva, and AA Firsov. **Electric field effect in atomically thin carbon films**. *Science*, **306**:666, 2004. 3, 5, 7, 10, 39, 89, 95

[9] PR Wallace. **The band theory of graphite**. *Physical Review*, **71**:622, 1947. 3, 6

[10] N.D. Mermin. **Crystalline order in two dimensions**. *Physical Review*, **176**:250, 1968. 3

[11] LD Landau, EM Lifshitz, and L.E. Reichl. *Statistical Physics, Part 1*, **34**. Pergamon, Oxford, 1981. 3

[12] Mazdak Taghioskoui. **Trends in graphene research**. *Materials Today*, **12**:34, 2009. 3

[13] Nathan O Weiss, Hailong Zhou, Lei Liao, Yuan Liu, Shan Jiang, Yu Huang, and Xiangfeng Duan. **Graphene: an emerging electronic material.** *Advanced materials*, **24**:5782, 2012. 3

[14] AK Geim and K. S. Novoselov. **The rise of graphene**. *Nature materials*, **6**:183, 2007. 4

[15] Eduardo V. Castro, H. Ochoa, M. I. Katsnelson, R. V. Gorbachev, D. C. Elias, K. S. Novoselov, A. K. Geim, and F. Guinea. **Limits on Charge Carrier Mobility in Suspended Graphene due to Flexural Phonons**. *Physical Review Letters*, **105**:266601, 2010. 3

[16] L Britnell, R V Gorbachev, R Jalil, B D Belle, F Schedin, A Mishchenko, T Georgiou, M I Katsnelson, L Eaves, S V Morozov, N M R Peres, J Leist, A K Geim, K S Novoselov, and L A Ponomarenko. **Field-effect tunneling transistor based on vertical graphene heterostructures.** *Science*, **335**:947, 2012. 4

[17] S. Ghosh, I. Calizo, D. Teweldebrhan, E. P. Pokatilov, D. L. Nika, A. A. Balandin, W. Bao, F. Miao, and C. N. Lau. **Extremely high thermal conductivity of graphene: Prospects for thermal management applications in nanoelectronic circuits**. *Applied Physics Letters*, **92**:151911, 2008. 4

[18] Alexander A Balandin, Suchismita Ghosh, Wenzhong Bao, Irene Calizo, Desalegne Teweldebrhan, Feng Miao, and Chun Ning Lau. **Superior thermal conductivity of single-layer graphene.** *Nano letters*, **8**:902, 2008. 4

[19] Changgu Lee, Xiaoding Wei, Jeffrey W Kysar, and James Hone. **Measurement of the elastic properties and intrinsic strength of monolayer graphene.** *Science*, **321**:385–8, 2008. 4

[20] S. Das Sarma, Shaffique Adam, E. H. Hwang, and Enrico Rossi. **Electronic transport in two-dimensional graphene**. *Reviews of Modern Physics*, **83**:407, 2011. 4, 6

[21] KS Novoselov, a. H.. Castro Neto, N. M. R.. Peres, AK Geim, and F. Guinea. **The electronic properties of graphene**. *Reviews of Modern Physics*, **81**:109, 2009. 4, 5, 6, 7, 9, 10, 15

[22] K. S. Novoselov, AK Geim, SV Morozov, D. Jiang, M.I.K.I.V. Grigorieva, SV Dubonos, and AA Firsov. **Two-dimensional gas of massless Dirac fermions in graphene**. *Nature*, **438**:197, 2005. 4, 8

[23] Alexander S Mayorov, Roman V Gorbachev, Sergey V Morozov, Liam Britnell, Rashid Jalil, Leonid A Ponomarenko, Peter Blake, Kostya S Novoselov, Kenji Watanabe, Takashi Taniguchi, and A K Geim. **Micrometer-scale ballistic transport in encapsulated graphene at room temperature.** *Nano letters*, **11**:2396, 2011. 4

[24] Yuanbo Zhang, Yan-Wen Tan, Horst L Stormer, and Philip Kim. **Experimental observation of the quantum Hall effect and Berry's phase in graphene.** *Nature*, **438**:201, 2005. 5

[25] David L Miller, Kevin D Kubista, Gregory M Rutter, Ming Ruan, Walt A de Heer, Phillip N First, and Joseph A Stroscio. **Observing the quantization of zero mass carriers in graphene.** *Science*, **324**:924–7, 2009. 5

[26] Kirill I Bolotin, Fereshte Ghahari, Michael D Shulman, Horst L Stormer, and Philip Kim. **Observation of the fractional quantum Hall effect in graphene.** *Nature*, **462**:196, 2009. 5

[27] M. I. Katsnelson, K. S. Novoselov, and A. K. Geim. **Chiral tunnelling and the Klein paradox in graphene**. *Nature Physics*, **2**:620, 2006. 5

[28] Andrea F. Young and Philip Kim. **Quantum interference and Klein tunnelling in graphene heterojunctions**. *Nature Physics*, **5**:222, 2009. 5

[29] Charles Kittel. *Introduction to Solid State Physics*. Wiley, eighth edi edition, 2004. 6, 9

[30] Mark Wilson. **Electrons in Atomically Thin Carbon Sheets Behave Like Massless Particles**. *Physics Today*, **59**:21, 2006. 7

[31] Edward McCann and Vladimir I. Falko. **Landau-Level Degeneracy and Quantum Hall Effect in a Graphite Bilayer**. *Physical Review Letters*, **96**:086805, 2006. 7

[32] Eduardo Castro, K. Novoselov, S. Morozov, N. Peres, J. dos Santos, Johan Nilsson, F. Guinea, A. Geim, and A. Neto. **Biased Bilayer Graphene: Semiconductor with a Gap Tunable by the Electric Field Effect**. *Physical Review Letters*, **99**:216802, 2007. 7

[33] Yuanbo Zhang, Tsung-Ta Tang, Caglar Girit, Zhao Hao, Michael C Martin, Alex Zettl, Michael F Crommie, Y Ron Shen, and Feng Wang. **Direct observation of a widely tunable bandgap in bilayer graphene.** *Nature*, **459**:820, 2009. 8

[34] C Casiraghi, A Hartschuh, E Lidorikis, H Qian, H Harutyunyan, T Gokus, KS Novoselov, and AC Ferrari. **Rayleigh imaging of graphene and graphene layers**. *Nano Letters*, **7**:2711, 2007. 11, 12

[35] P. Blake, E. W. Hill, A. H. Castro Neto, K. S. Novoselov, D. Jiang, R. Yang, T.J. J. Booth, and A. K. Geim. **Making graphene visible**. *Applied Physics Letters*, **91**:063124, 2007. 11, 12, 55

[36] D. S. L. Abergel, a. Russell, and Vladimir I. Falko. **Visibility of graphene flakes on a dielectric substrate**. *Applied Physics Letters*, **91**:063125, 2007. 11, 12

[37] AK Geim. **Graphene: status and prospects.** *Science*, **324**:1530, 2009. 11

[38] Taeshik Yoon, Woo Cheol Shin, Taek Yong Kim, Jeong Hun Mun, Taek-Soo Kim, and Byung Jin Cho. **Direct measurement of adhesion energy of monolayer graphene as-grown on copper and its application to renewable transfer process.** *Nano letters*, **12**:1448, 2012. 11

[39] Hugo Anders. *Thin Films in Optics*. Focal, London, 1967. 12, 54

[40] E.D. Palik. *Handbook of optical constants of solids*. Academic, New York, 1991. 12, 54

[41] Guoquan Teo, Haomin Wang, Yihong Wu, Zaibing Guo, Jun Zhang, Zhenhua Ni, and Zexiang Shen. **Visibility study of graphene multilayer structures**. *Journal of Applied Physics*, **103**:124302, 2008. 12

[42] Xiaolin Li, Guangyu Zhang, Xuedong Bai, Xiaoming Sun, Xinran Wang, Enge Wang, and Hongjie Dai. **Highly conducting graphene sheets and Langmuir-Blodgett films.** *Nature nanotechnology*, **3**:538, 2008. 12

[43] Yenny Hernandez, Valeria Nicolosi, Mustafa Lotya, Fiona M Blighe, Zhenyu Sun, Sukanta De, McGoverni. T., Brendan Holland, Michele Byrne, Yurii K Gun'Ko, John J Boland, Peter Niraj, Georg Duesberg, Satheesh Krishnamurthy, Robbie Goodhue, John Hutchison, Vittorio Scardaci, Andrea C Ferrari, and Jonathan N Coleman. **High-yield production of graphene by liquid-phase exfoliation of graphite**. *Nature nanotechnology*, **3**:563, 2008. 13

[44] Goki Eda, Giovanni Fanchini, and Manish Chhowalla. **Large-area ultrathin films of reduced graphene oxide as a transparent and flexible electronic material.** *Nature nanotechnology*, **3**:270, 2008. 13

[45] Claire Berger, Zhimin Song, Tianbo Li, Xuebin Li, Asmerom Y. Ogbazghi, Rui Feng, Zhenting Dai, Alexei N. Marchenkov, Edward H. Conrad, Phillip N. First, and Walt A. de Heer. **Ultrathin Epitaxial Graphite: 2D Electron Gas Properties and a Route toward Graphene-based Nanoelectronics**. *The Journal of Physical Chemistry B*, **108**:19912, 2004. 13

[46] Alfonso Reina, Xiaoting Jia, John Ho, Daniel Nezich, Hyungbin Son, Vladimir Bulovic, Mildred S Dresselhaus, and Jing Kong. **Large area, few-layer graphene films on arbitrary substrates by chemical vapor deposition.** *Nano letters*, **9**:30, 2009. 13

[47] Sukang Bae, Hyeongkeun Kim, Youngbin Lee, Xiangfan Xu, Jae-Sung Park, Yi Zheng, Jayakumar Balakrishnan, Tian Lei, Hye Ri Kim, Young Il Song, Young-Jin Kim, Kwang S Kim, Barbaros Ozyilmaz, Jong-Hyun Ahn, Byung Hee Hong, and Sumio Iijima. **Roll-to-roll production of 30-inch graphene films for transparent electrodes.** *Nature nanotechnology*, **5**:574, 2010. 13

[48] M. S. Dresselhaus and G. Dresselhaus. **Intercalation compounds of graphite**. *Advances in Physics*, **51**:1, 2002. 14, 15, 17, 18, 32, 35, 42, 43, 95

[49] Toshiaki Enoki, M Endo, and Masatsugu Suzuki. *Graphite Intercalation Compounds and Applications*. OUP, 2003. 14, 15, 17, 19, 42, 43, 44, 82

[50] N. Hannay, T. Geballe, B. Matthias, K. Andres, P. Schmidt, and D. MacNair. **Superconductivity in Graphitic Compounds**. *Physical Review Letters*, **14**:225, 1965. 15

[51] C. Underhill, T. Krapchev, and M.S. Dresselhaus. **Synthesis and characterization of high stage alkali metal donor compounds**. *Synthetic Metals*, **2**:47–55, 1980. 15

[52] L. Pietronero, S. Strässler, H. Zeller, and M. Rice. **Charge Distribution in c Direction in Lamellar Graphite Acceptor Intercalation Compounds**. *Physical Review Letters*, **41**:763, 1978. 15, 41

[53] S. Safran and D. Hamann. **Electrostatic interactions and staging in graphite intercalation compounds**. *Physical Review B*, **22**:606–612, 1980. 15, 41

[54] G.K. Wertheim, P.M.Th.M. van Attekum, H.J. Guggenheim, and K.E. Clements. **Acceptor site in metal halide intercalated graphite**. *Solid State Communications*, **33**:809, 1980. 15

[55] G.K. Wertheim. **Island formation in metal halide intercalation compouds**. *Solid State Communications*, **38**:633, 1981. 15

[56] D. Wiesler, M. Suzuki, and H. Zabel. **Ordering in quasi-two-dimensional planar ferromagnets: A neutron scattering study of graphite intercalation compounds**. *Physical Review B*, **36**:7051, 1987. 15

[57] R. Nishitani, Y. Uno, and H. Suematsu. **Study of statics and dynamics of staging in K and Rb GICs by in situ X-ray observation**. *Synthetic Metals*, **7**:13, 1983. 16, 78

[58] JM Thomas, GR Millward, R.F. Schlögl, and H.P. Boehm. **Direct imaging of a graphite intercalate: Evidence of interpenetration of stages in graphite: Ferric chloride**. *Materials Research Bulletin*, **15**:671, 1980. 16

[59] G. Kirczenow. **Domain model of stage order and disorder in intercalation compounds**. *Physical Review B*, **31**:5376, 1985. 16

[60] M. Heerschap and P. Delavignette. **Electron-microscopy study of the ferric chloride/graphite compound**. *Carbon*, **5**:383, 1967. 17

[61] H Zabel and S.A. Solin. *Graphite intercalation compounds II*. Springer-Verlag, 1992. 17, 18

[62] Peter Larkin. *Infrared and Raman Spectroscopy*. Elsevier, 2011. 20

[63] Andrea C Ferrari, J.C. Meyer, V. Scardaci, C. Casiraghi, M. Lazzeri, F. Mauri, S. Piscanec, D. Jiang, K. S. Novoselov, S. Roth, and A. K. Geim. **Raman spectrum of graphene and graphene layers**. *Physical Review Letters*, **97**(18):187401, 2006. 20, 24, 26, 27, 29, 69, 78, 83

[64] John R Ferraro. *Introductory Raman Spectroscopy*. Elsevier, 2003. 21

[65] Andrea C Ferrari and Denis M Basko. **Raman spectroscopy as a versatile tool for studying the properties of graphene.** *Nature nanotechnology*, **8**:235, 2013. 21, 23, 25, 32

[66] Michele Lazzeri, Claudio Attaccalite, Ludger Wirtz, and Francesco Mauri. **Impact of the electron-electron correlation on phonon dispersion: Failure of LDA and GGA DFT functionals in graphene and graphite**. *Physical Review B*, **78**:081406, 2008. 21, 22

[67] L.M. Malard, M. A. Pimenta, G. Dresselhaus, and M.S. Dresselhaus. **Raman spectroscopy in graphene**. *Physics Reports*, **473**:51, 2009. 22, 25, 26, 27, 69

[68] Stephanie Reich and Christian Thomsen. **Raman spectroscopy of graphite.** *Philosophical transactions. Series A, Mathematical, physical, and engineering sciences*, **362**:2271, 2004. 23

[69] R Saito, M Hofmann, and G Dresselhaus. **Raman spectroscopy of graphene and carbon nanotubes**. *Advances in Physics*, page 413, 2011. 22

[70] R.P. Vidano, D.B. Fischbach, L.J. Willis, and T.M. Loehr. **Observation of Raman band shifting with excitation wavelength for carbons and graphites**. *Solid State Communications*, **39**:341, 1981. 25

[71] A Das, S Pisana, B Chakraborty, S Piscanec, S K Saha, U V Waghmare, K S Novoselov, H R Krishnamurthy, A K Geim, A C Ferrari, and A K Sood. **Monitoring dopants by Raman scattering in an electrochemically top-gated graphene transistor.** *Nature Nanotechnology*, **3**:210, 2008. 26, 28

[72] A. Das, B. Chakraborty, S. Piscanec, S. Pisana, A. Sood, and A. Ferrari. **Phonon renormalization in doped bilayer graphene**. *Physical Review B*, **79**:155417, 2009. 26

[73] L. Pietronero and S. Strässler. **Electron-phonon scattering and electrical conductivity of graphite intercalation compounds**. *Synthetic Metals*, **3**:213, 1981. 26

[74] Weijie Zhao, Ping Heng Tan, Jian Liu, and Andrea C Ferrari. **Intercalation of few-layer graphite flakes with $FeCl_3$: Raman determination of Fermi level, layer by layer decoupling, and stability.** *Journal of the American Chemical Society*, **133**:5941–6, 2011. 26, 33, 35, 68

[75] Michele Lazzeri and Francesco Mauri. **Nonadiabatic Kohn Anomaly in a Doped Graphene Monolayer**. *Physical Review Letters*, **97**:266407, 2006. 26

[76] Jun Yan, Yuanbo Zhang, Philip Kim, and Aron Pinczuk. **Electric Field Effect Tuning of Electron-Phonon Coupling in Graphene**. *Physical Review Letters*, **98**:166802, 2007. 26, 69, 71

[77] D. M. Basko, S. Piscanec, and A. C. Ferrari. **Electron-electron interactions and doping dependence of the two-phonon Raman intensity in graphene**. *Physical Review B*, **80**:165413, 2009. 27, 83

[78] Simone Pisana, Michele Lazzeri, Cinzia Casiraghi, Kostya S Novoselov, a K Geim, Andrea C Ferrari, and Francesco Mauri. **Breakdown of the adiabatic Born-Oppenheimer approximation in graphene.** *Nature materials*, **6**:198, 2007. 28

[79] L. M. Malard, J. Nilsson, D. C. Elias, J. C. Brant, F. Plentz, E. S. Alves, a. H. Castro Neto, and M. a. Pimenta. **Probing the electronic structure of bilayer graphene by Raman scattering**. *Physical Review B*, **76**:201401, 2007. 30

[80] Pierre Lespade, André Marchand, Michel Couzi, and Francis Cruege. **Caracterisation de materiaux carbones par microspectrometrie Raman**. *Carbon*, **22**:375, 1984. 31

[81] K. Kim, S. Coh, Liang Tan, W. Regan, J. Yuk, E. Chatterjee, M. Crommie, M. Cohen, S. Louie, and A. Zettl. **Raman Spectroscopy Study of Rotated Double-Layer Graphene: Misorientation-Angle Dependence of Electronic Structure**. *Physical Review Letters*, **108**:246103, 2012. 31, 82

[82] P H Tan, W P Han, W J Zhao, Z H Wu, K Chang, H Wang, Y F Wang, N Bonini, N Marzari, N Pugno, G Savini, A Lombardo, and A C Ferrari. **The shear mode of multilayer graphene.** *Nature materials*, **11**:294, 2012. 31

[83] Zhen Hua Ni, Ting Yu, Yun Hao Lu, Ying Ying Wang, Yuan Ping Feng, and Ze Xiang Shen. **Uniaxial strain on graphene: Raman spectroscopy study and band-gap opening.** *ACS nano*, **2**:2301, 2008. 32

[84] T. Mohiuddin, a. Lombardo, R. Nair, a. Bonetti, G. Savini, R. Jalil, N. Bonini, D. Basko, C. Galiotis, N. Marzari, K. Novoselov, a. Geim, and a. Ferrari. **Uniaxial strain in graphene by Raman spectroscopy: G peak splitting, Grüneisen parameters, and sample orientation**. *Physical Review B*, **79**:205433, 2009. 32

[85] Mingyuan Huang, Hugen Yan, Changyao Chen, Daohua Song, Tony F Heinz, and James Hone. **Phonon softening and crystallographic orientation of strained graphene studied by Raman spectroscopy.** *Proceedings of the National Academy of Sciences of the United States of America*, **106**:7304, 2009. 32

[86] V. Geringer, M. Liebmann, T. Echtermeyer, S. Runte, M. Schmidt, R. Rückamp, M. Lemme, and M. Morgenstern. **Intrinsic and extrinsic corrugation of monolayer graphene deposited on SiO2**. *Physical Review Letters*, **102**:076102, 2009. 32

[87] Elena Stolyarova, Kwang Taeg Rim, Sunmin Ryu, Janina Maultzsch, Philip Kim, Louis E Brus, Tony F Heinz, Mark S Hybertsen, and George W Flynn. **High-resolution scanning tunneling microscopy imaging of mesoscopic graphene sheets on an insulating surface.** *Proceedings of the National Academy of Sciences of the United States of America*, **104**:9209, 2007. 32

[88] C. Underhill, S.Y. Leung, G. Dresselhaus, and M.S. Dresselhaus. **Infrared and Raman spectroscopy of graphite-ferric chloride**. *Solid State Communications*, **29**:769, 1979. 32, 33, 34, 45, 68

[89] Da Zhan, Li Sun, Zhen Hua Ni, Lei Liu, Xiao Feng Fan, Yingying Wang, Ting Yu, Yeng Ming Lam, Wei Huang, and Ze Xiang Shen. **$FeCl_3$-Based Few-Layer Graphene Intercalation Compounds: Single Linear Dispersion Electronic Band Structure and Strong Charge Transfer Doping**. *Advanced Functional Materials*, **20**:3504, 2010. 33

[90] Namdong Kim, Kwang S Kim, Naeyoung Jung, Louis Brus, and Philip Kim. **Synthesis and electrical characterization of magnetic bilayer graphene intercalate.** *Nano Letters*, **11**:860, 2011. 33, 35, 37, 105, 114

[91] I. Khrapach, F. Withers, T. H. Bointon, D. K. Polyushkin, W. L. Barnes, S. Russo, and M.F. Craciun. **Novel Highly Conductive and Transparent Graphene-Based Conductors**. *Advanced Materials*, **24**:2844, 2012. 33, 35, 36, 37, 105, 114

[92] Y. Martin, C. C. Williams, and H. K. Wickramasinghe. **Atomic force microscopeforce mapping and profiling on a sub 100-A scale**. *Journal of Applied Physics*, **61**:4723, 1987. 37

[93] C H Lei, A Das, M Elliott, and J E Macdonald. **Quantitative electrostatic force microscopy-phase measurements**. *Nanotechnology*, **15**:627, 2004. 38

[94] Marc Bockrath, Nina Markovic, Adam Shepard, M. Tinkham, Leonid Gurevich, Leo P. Kouwenhoven, Mingshaw W. Wu, and L. L. Sohn. **Scanned Conductance Microscopy of Carbon Nanotubes and λ-DNA**. *Nano Letters*, **2**:187, 2002. 38

[95] Sujit S. Datta, Douglas R. Strachan, E. J. Mele, and A. T. Johnson. **Surface potentials and layer charge distributions in few-layer graphene films.** *Nano Letters*, **9**:7, 2009. 38, 39, 40, 41, 95

[96] Chun Hung Lui, Li Liu, Kin Fai Mak, George W Flynn, and Tony F Heinz. **Ultraflat graphene.** *Nature*, **462**:339, 2009. 38

[97] P Nemesincze, Z Osvath, K Kamaras, L Biro, and P Nemesincze. **Anomalies in thickness measurements of graphene and few layer graphite crystals by tapping mode atomic force microscopy**. *Carbon*, **46**:1435, 2008. 39

[98] T. Filleter, K. V. Emtsev, Th. Seyller, and R. Bennewitz. **Local work function measurements of epitaxial graphene**. *Applied Physics Letters*, **93**:133117, 2008. 39, 40

[99] Tim Burnett, Rositza Yakimova, and Olga Kazakova. **Mapping of local electrical properties in epitaxial graphene using electrostatic force microscopy.** *Nano Letters*, **11**:2324–, 2011. 39

[100] D. Ziegler, P. Gava, J. Güttinger, F. Molitor, L. Wirtz, M. Lazzeri, a. M. Saitta, a. Stemmer, F. Mauri, and C. Stampfer. **Variations in the work function of doped single- and few-layer graphene assessed by Kelvin probe force microscopy and density functional theory**. *Physical Review B*, **83**:235434, 2011. 39

[101] Young-Jun Yu, Yue Zhao, Sunmin Ryu, Louis E Brus, Kwang S Kim, and Philip Kim. **Tuning the graphene work function by electric field effect.** *Nano letters*, **9**:3430, 2009. 39

[102] N. J. Lee, J. W. Yoo, Y. J. Choi, C. J. Kang, D. Y. Jeon, D. C. Kim, S. Seo, and H. J. Chung. **The interlayer screening effect of graphene sheets investigated by Kelvin probe force microscopy**. *Applied Physics Letters*, **95**:222107, 2009. 39

[103] Andres Castellanos-Gomez, Roel H.M. Smit, Nicolás Agraït, and Gabino Rubio-Bollinger. **Spatially resolved electronic inhomogeneities of graphene due to subsurface charges**. *Carbon*, **50**:932, 2012. 39

[104] Yumeng Shi, Xiaochen Dong, Peng Chen, Junling Wang, and Lain-Jong Li. *Physical Review B*, page 115402. 39

[105] Yonghua Lu, M. Muñoz, C. Steplecaru, Cheng Hao, Ming Bai, N. Garcia, K. Schindler, and P. Esquinazi. **Electrostatic Force Microscopy on Oriented Graphite Surfaces: Coexistence of Insulating and Conducting Behaviors**. *Physical Review Letters*, **97**:076805, 2006. 41

[106] Zhenhua Ni, Yingying Wang, Ting Yu, and Zexiang Shen. **Raman spectroscopy and imaging of graphene**. *Nano Research*, **1**:273, 2010. 45

[107] Nitto Denko Corporation. **SWT 10+ adhesive tape**. 49

[108] Shiren Wang, Yue Zhang, Noureddine Abidi, and Luis Cabrales. **Wettability and surface free energy of graphene films.** *Langmuir : the ACS journal of surfaces and colloids*, **25**:11078–81, 2009. 52

[109] Eugene Hecht. *Optics*. Addison Wesley, 2002. 54

[110] I. Pollini, J. Thomas, and A. Lenselink. **Optical properties of layered transition-metal halides**. *Physical Review B*, **30**:2140, 1984. 55

[111] Frank Pobell. *Matter and Methods at Low Temperatures*. Springer, 1992. 63

[112] Elena Stolyarova, Kwang Taeg Rim, Sunmin Ryu, Janina Maultzsch, Philip Kim, Louis E Brus, Tony F Heinz, Mark S Hybertsen, and George W Flynn. **High-resolution scanning tunneling microscopy imaging of mesoscopic graphene sheets on an insulating surface.** *Proceedings of the National Academy of Sciences of the United States of America*, **104**:9209, 2007. 64

[113] Masa Ishigami, J H Chen, W G Cullen, M S Fuhrer, and E D Williams. **Atomic structure of graphene on SiO2.** *Nano letters*, **7**:1643, 2007. 64

[114] J. Moser, A. Barreiro, and A. Bachtold. **Current-induced cleaning of graphene**. *Applied Physics Letters*, **91**:163513, 2007. 64

[115] a Barreiro, F Börrnert, M H Rümmeli, B Büchner, and L M K Vandersypen. **Graphene at high bias: cracking, layer by layer sublimation, and fusing.** *Nano letters*, **12**:1873, 2012. 64, 65

[116] Jian Yu Huang, Feng Ding, Boris I Yakobson, Ping Lu, Liang Qi, and Ju Li. **In situ observation of graphene sublimation and multi-layer edge reconstructions.** *Proceedings of the National Academy of Sciences of the United States of America*, **106**:10103, 2009. 65

[117] Jian Yu Huang, Liang Qi, and Ju Li. **In situ imaging of layer-by-layer sublimation of suspended graphene**. *Nano Research*, **3**:43, 2010. 65

[118] N. Caswell and S.A. Solin. **Vibrational excitations of pure FeCl3 and graphite intercalated with ferric chloride**. *Solid State Communications*, **27**:961, 1978. 72

[119] N. Staley, H. Wang, C. Puls, J. Forster, T. N. Jackson, K. McCarthy, B. Clouser, and Y. Liu. **Lithography-free fabrication of graphene devices**. *Applied Physics Letters*, **90**:143518, 2007. 104

[120] Keun Soo Kim, Yue Zhao, Houk Jang, Sang Yoon Lee, Jong Min Kim, Kwang S Kim, Jong-Hyun Ahn, P. Kim, Jae-Young Choi, and Byung Hee Hong. **Large-scale pattern growth of graphene films for stretchable transparent electrodes.** *Nature*, **457**:706, 2009. 114

[121] L. Hao, C. Ass mann, J. C. Gallop, D. Cox, F. Ruede, O. Kazakova, P. Josephs-Franks, D. Drung, and Th. Schurig. **Detection of single magnetic nanobead with a nano-superconducting quantum interference device**. *Applied Physics Letters*, **98**:092504, 2011. 114

[122] E. J. Romans, E. J. Osley, L. Young, P. a. Warburton, and W. Li. **Three-dimensional nanoscale superconducting quantum interference device pickup loops**. *Applied Physics Letters*, **97**:222506, 2010. 114